THE SNO+ SUPERNOVA CALIBRATION SOURCE DEVELOPMENT AND TESTING

by

Caitlyn Darrach

A thesis submitted in partial fulfillment
of the requirements for the degree of
Master of Science in Physics

The Faculty of Graduate Studies

Laurentian University
Sudbury, Ontario, Canada

THESIS DEFENCE COMMITTEE/COMITÉ DE SOUTENANCE DE THÈSE
Laurentian Université/Université Laurentienne
Faculty of Graduate Studies/Faculté des études supérieures

Title of Thesis
Titre de la thèse THE SNO+ SUPERNOVA CALIBRATION SOURCE

Name of Candidate
Nom du candidat Darrach, Aimee Caitlyn

Degree
Diplôme Master of Science

Department/Program
Département/Programme Physics

Date of Defence
Date de la soutenance July 19, 2016

APPROVED/APPROUVÉ

Thesis Examiners/Examinateurs de thèse:

Dr. Clarence Virtue
(Supervisor/Directeur(trice) de thèse)

Dr. Christine Kraus
(Co-supervisor/Co-directeur(trice) de thèse)

Dr. Rizwan Haq
(Committee member/Membre du comité)

Dr. Victor Zacek
(External Examiner/Examinateur externe)

Approved for the Faculty of Graduate Studies
Approuvé pour la Faculté des études supérieures
Dr. Shelley Watson
Monsieur Shelley Watson
Acting Dean, Faculty of Graduate Studies
Doyenne intérimaire, Faculté des études supérieures

ACCESSIBILITY CLAUSE AND PERMISSION TO USE

Abstract

SNO+ is a kilotonne-scale, liquid scintillator-based neutrino detector housed in the underground facilities of SNOLAB at Creighton Mine, Sudbury. SNO+ is capable of detecting bursts of neutrinos released by nearby core-collapse supernovae among other physics goals. For such an event, stress testing is required to ensure that a burst of supernova neutrino events can be reliably read out and recorded by the electronics and data acquisition system to avoid data pileup and limit event separation. During a supernova, SNO+ needs to be able to record the burst, send a timely alert to the astronomical community, and quickly analyze and interpret the data.

The supernova calibration system (SNC+) for SNO+ simulates the light produced by interactions of neutrinos from a supernova within the liquid scintillator target using pulsed, visible light from a laser diode. The SNC+ is a data-driven pulser capable of producing high-powered, ns-scale pulses with repetition rates up to 12.5 MHz. Each photon pulse is expected to deposit energy of up to 70 MeV within the liquid scintillator of the SNO+ detector. The light from the SNC+ laser diode will be delivered isotropically within the SNO+ detector by fiber optics and a diffusing glass laserball. The SNC+ has undergone design, parts procurement, construction, assembly, and initial-stage testing for this thesis research.

Keywords: SNC+, SNO+, supernova, pulsed optical source, calibration, neutrino

Acknowledgments

I would like to express my gratitude to my co-supervisor Dr. Clarence Virtue for his time, expert guidance, and gracious support throughout the course of this work, and to my co-supervisor Dr. Christine Kraus for her flexibility, support, and continued guidance throughout my degree. I'd also like to acknowledge my internal advisory committee member Dr. Rizwan Haq for his time and valued input on my thesis and research, and my external advisor, Dr. Viktor Zacek.

Dr. Jean-Pierre Martin at the University of Montreal provided excellent SNC+ boards and FPGA programming along with ongoing advice. Mark Stringer was pivotal in adapting the TELLIE resources to the SNC+ analysis and providing input throughout. Dr. Chris Jillings and Dr. Valentina Lozza, thank you for your assistance during the XRF studies. Greg in the Laurentian Machine Shop, I've bothered you many, many times - thank you for your patience. To the SNOLAB "Mikes", Schwendener and Schumaker, thank you for your first year of seasoned guidance and support in the office. Thank you also to Dr. Erica Caden-Cronin and Dave Braid for your general helpfulness around the office and lab. A special thanks to Oleg C. for your patience in allowing me to use your scope for a month longer than anticipated.

Chris Jillings, Ian Lawson, Nigel Smith, Eric Vasquez, and professors Gennady Chitov and Rizwan Haq - thank you for your high-quality teaching and lessons.

Fellow SNO+ colleagues and local friends (Kate, Rob, Suzy, Annette, John, Sarah, Jack, Ed, Tony, Freija, Evelina, Chris J., Tim, Morgan, Teal, Sean, Eric, Matt S., Dr. Mottram, Laura, Ian, the list goes on...), you always made collaboration meetings and Sudbury Saturday Nights a fun occasion.

Nancy Brown, aka SNOLAB mom, thank you for your hugs, chats, and Beef 'n' Bird Porchetta invites. There's nothing like free bingo meat to make a graduate student's day. Thank you also

to Taylor Shantz for your couch and kindness. Tom and Eleanor, thanks for hosting amazing boardgames nights!

To my SNOLAB friends, particularly Janet Rumleskie and Steve Linden - thank you for an amazing Dungeons and Dragons campaign and being generally awesome. I would also like to thank fellow students and office mates Colin Bruulsema, Stephane Venne, and Ingrida Semenec for their friendship, boardgames nights and lively discussions typically coasting into absurdism.

To my two sisters, thanks for pretending to care about my research. You are inspiring, smart, well-rounded women whom I enjoy bragging about.

To my parents, Patricia and Wayne Darrach, and grandparents, Joan and Doug MacPhail, thank you for your generosity, encouragement, and love during, but not limited to, my graduate studies. I wouldn't have been here without you.

Contents

List of Figures

List of Tables

Chapter 1

Introduction

1.1 Introduction to Neutrinos

In October 2015, the Nobel Prize in Physics was awarded jointly to Takaaki Kajita and Arthur B. McDonald for their discovery that elementary particles called neutrinos oscillate between neutrino flavours and have mass. This is, remarkably, the fourth Nobel Prize associated with the experimental measurement of neutrinos. One might wonder why humans should care so much about these strange, incredibly small particles, which barely interact with ordinary matter.

Neutrinos are neutral, almost massless elementary particles which travel through space almost at the speed of light and weakly interact with matter. Trillions of neutrinos per square centimeter flow through the Earth every second. Some were created in the Big Bang, others are constantly being created in various processes in space and on Earth – from exploding supernovae, the deaths of massive stars, reactions in nuclear power plants to fusion in the Sun.

Because neutrinos interact only weakly, they can travel immense distances. They provide us with a window into places we would never otherwise be able to see, such as the inner core of a star undergoing supernova. In the Standard Model (SM) of particle physics which has correctly described every other observation that has been made in particle accelerators and other experiments in the past century, neutrinos were once thought to be massless. The discovery of a massive neutrino is the first evidence of physics beyond the Standard Model and indicates that there is new physics that remains to be discovered beyond it. The Standard Model has since been extended to include massive neutrinos.

1.2 Brief History of Neutrinos

Historically, the study of beta decay provided the first physical evidence of the neutrino. In 1911, physicist Lise Meitner, most famous for her discovery of nuclear fission, and chemist Otto Hahn performed an experiment demonstrating that the energies of electrons emitted by beta decay had a continuous rather than a discrete spectrum [1], confirming results by Charles Ellis and William Wooster [2]. This was in apparent contradiction with the law of conservation of energy, as it appeared that energy was lost in the beta decay process. Scientists at the time could not understand why there was a continuous energy spectrum. If the decay was to a two-body state, as physicists at the time believed, then the conservation of energy and momentum required a unique energy for the emitted electron - which was clearly not the case. The conservation laws were under question.

The neutrino was first postulated as a "desperate way out" in 1930 by Wolfgang Pauli. In a famous letter addressed to the "Radioactive Ladies and Gentlemen" for a convention in Tübingen [3], Pauli suggested that in addition to electrons and protons, atoms also contained an extremely light, neutral, spin-1/2 particle which he called the neutron. He suggested that this "neutron" was also emitted during β-decay and had simply not yet been observed.

By 1934 after implementing Pauli's proposal, Enrico Fermi had developed his Theory of Weak Interactions, describing beta decay, to include the neutrino which was presumed to be massless as well as chargeless. Fermi renamed Pauli's "neutron" to neutrino as a word play on *neutrone*, the Italian name of the neutron[1].

The neutrino was experimentally observed by Clyde L. Cowan and Frederick Reines in 1956 [4] nearly 26 after its prediction when nuclear reactors were available. They were awarded the Nobel Prize in Physics in 1995. Their experiment used a nuclear reactor, expected to produce neutrino fluxes on the order of 10^{12-13} neutrinos per second per cm^2, far higher than any attainable flux from other radioactive sources. The neutrinos would then weakly interact with protons in a tank of water containing cadmium chloride, a highly-effective neutron absorber. This reaction created neutrons and positrons via the inverse beta decay reaction:

$$\bar{\nu} + p \rightarrow n + e^{+} \tag{1.1}$$

[1] *Neutrone* in Italian means big and neutral, and neutrino means small and neutral.

The positron produced in the decay annihilates immediately with an electron, creating two gamma rays. Several microseconds later the neutron is captured by cadmium creating another gamma ray. This delayed coincidence signal, on the order of $\sim$5 μs between the 2 γ-rays, provided a distinction between likely neutrino events and other background signals. The gamma rays were detected by placing a scintillator material in a tank of water, which emits photons that are detected by photomultiplier tubes.

After months of data collection, they saw on average 3 ν/hour in their detector, corresponding to a cross-section of 6.3×10^{-44} cm^2 to be compared to a predicted one of $\sim 6 \times 10^{-44}$ cm^2.

The first generation of neutrino, the "electron" neutrino (ν_e), discovered by Reines and Cowan was named after its associated lepton. In 1962, Leon Lederman, Melvin Schwartz and Jack Steinberger discovered a second type of neutrino, the muon neutrino (ν_μ) [5], establishing that neutrinos existed in different "flavours."

Following the muon neutrino discovery, Maki, Nakagawa, and Sakata suggested these two neutrinos mix via unitary couplings [6]. In 1958, M. Goldhaber *et al.* measured neutrino helicity which was negative (spin anti-parallel to momentum) [7]. Furthermore, Pontecorvo suggested that neutrinos oscillate, originally proposed between neutrino-anti-neutrino states and later between the flavour states [8].

In 1968 R. Davis *et al.* working on the Homestake experiment measured the solar electron neutrino flux for the first time [9]. The experiment consisted of a 100,000 gallon tank of perchloroethylene, a common dry-cleaning fluid which acted as a target placed underground. Upon interaction with an electron neutrino, a chlorine-37 atom transforms into a radioactive isotope of argon-37, which can then be extracted and counted. The reaction of neutrino capture is

$$\nu_e + {}^{37}Cl \longrightarrow {}^{37}Ar + e^- \tag{1.2}$$

Every few weeks, Davis bubbled helium through the tank to collect the argon that had formed. A small gas counter was filled by the collected few tens of atoms of argon-37 (together with the stable argon) to detect its decays. In this way, Davis was able to determine how many neutrinos had been captured and found solar neutrino flux to be significantly less than that predicted by the solar models, giving rise to the *solar neutrino problem* which was later solved by the SNO

experiment which will be discussed in detail later in this section.

In 1976, M. Perl *et al.* discovered the tau lepton, evidence that another neutrino type existed [10]. It was eventually observed by the DONUT experiment at Fermilab in 2001[11] which accelerated protons using a Tevatron. This produced tau neutrinos via decay of charmed mesons. When a tau neutrino interacted in the detector, it produced electrically-charged particles which left visible tracks in the emulsion and could be electronically registered by a system of scintillators and drift chambers.

The Large Electron Positron Collider (LEP), built at CERN near Geneva, collided electrons with positrons at energies that reached 209 GeV. When an electron and a positron collide, they annihilate to a virtual particle, either a photon or a Z boson. The virtual particle almost immediately decays into other elementary particles like neutrinos, which are then detected. Statistical analysis of the LEP neutrino results constrained the number of neutrino flavours to 3 in 1989: the electron neutrino, ν_e; the muon neutrino, ν_μ; and the tau neutrino, ν_τ [12].

An *atmospheric neutrino anomaly*, the unexpected difference between measured and predicted muon/electron flavour composition of the atmostpheric neutrino flux, was observed in 1988 by the IMB [13] and Kamiokande [14]. The anomaly was later solved by Super-Kamiokande in 1998, which found an energy and zenith-angle-dependent deficit of the muon neutrinos, or rather, evidence towards neutrino oscillations and implication of a neutrino mass [15] [16]. Super-K's result set minimum limits on the neutrino mass by measuring differences in mass squares and oscillation parameters.

In 2002, The Sudbury Neutrino Observatory, SNO, solved the *solar neutrino problem*, showing a deficit in the electron neutrino flux and no deficit in the total neutrino flux, implying oscillation of the electron neutrinos into muon or tau neutrinos [17]. Dr. Art MacDonald of Queen's University, Canada who led the SNO experiment was recently co-awarded the 2015 Nobel Prize in Physics [18] for this discovery of neutrino oscillations, which shows that neutrinos have mass[2].

[2]Neutrino flavour oscillation requires that the mass eigenstates of neutrinos are not equal and that the mass eigenstate is also not a flavour eigenstate. Since a neutrino is always produced in a flavour eigenstate, this flavour eigenstate wave function will be a mixture of the 3 mass eigenstates such that at the time of production it is a pure flavour eigenstate. However, as the neutrino wave function propagates, the 3 mass eigenstates will effectively move at different speeds so that at the point in space where the propagating neutrino interacts with the measuring apparatus, it will be a different mixture of flavour eigenstates. Thus, the possibility of flavour oscillation requires that the masses of the mass eigenstates are not equal.

1.3 Neutrino Theory

1.3.1 Neutrinos in the Standard Model

The Standard Model (SM) of particle physics is the theoretical framework that describes the interactions between the elementary building blocks of matter and their force carriers. It is the theory that condenses hundreds of particles and interactions into a simplified and structured model which allows predictions to be made about particle interactions.

The SM includes three fundamental forces: the electomagnetic, the weak, and the strong. Every particle is also expected to couple to the graviton, which carries the gravitational force, but this coupling is not part of the SM. The SM is not a complete theory of fundamental interactions, primarily because it does not describe the fourth known interaction: gravity.

Each fundamental force between matter particles is carried by distinct subatomic particles. The force carrier particles are called gauge bosons and are characterized by integer values of the spin quantum number. As seen in Figure 1.1 developed by CERN, the gauge bosons of the SM are 8 gluons (g), which mediate the strong force, one photon (γ), mediating the electromagnetic interaction, and three intermediate vector bosons (the $W^{\pm}$ and the Z^0), mediating the weak force. Exchange of the Z^0 boson is called the neutral current weak interaction. Exchange of either the W^+ or W^- boson is called the charged current weak interaction. The SM gauge bosons also includes a single scalar (spin-0) particle, the Higgs boson (H), which is associated with spontaneous electroweak symmetry breaking. François Englert and Peter W. Higgs were jointly awarded the Nobel prize in physics in 2013 for their theoretical discovery of the Higg's mechanism that contributes to our understanding of the origin of mass of subatomic particles, and which was confirmed through the discovery of the predicted fundamental particle, the Higgs boson, by the ATLAS and CMS experiments at CERN's Large Hadron Collider in 2012 [19].

The Standard Model (SM) contains 12 fermions, each existing with their complementary antimatter particle for a total of 24 fermions and 6 bosons. The fermionic elementary particles which make up the SM are quarks and leptons, both of which exist in three sets of distinct pairs for a total of 6 quarks and 6 leptons. Each set of quark and lepton pairs is called a generation of matter which is organized by increasing mass, as seen in Figure 1.1 as 1^{st}, 2^{nd} and 3^{rd} Generation. Leptons and quarks in the first generation of matter are considered stable "everyday matter" since

they represent the matter constituting the physical world, whereas those in the 2^{nd} and 3^{rd} are considered exotic.

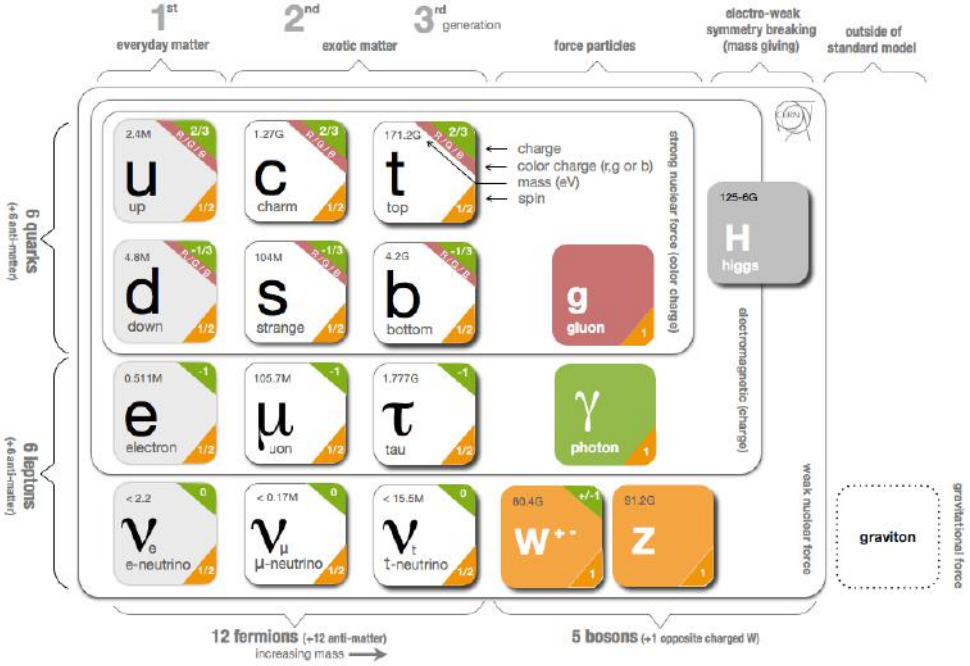

Figure 1.1: The Standard Model of particle physics as it currently stands includes 3 flavours of neutrinos and antineutrinos. Neutrinos and antineutrinos are classified as leptons along with electrons, muons, and tau particles and their respective antiparticles. Three gauge bosons (W^+, W^- and Z^0) are defined as force carriers that mediate the strong, weak, and electromagnetic fundamental interactions. Six types of quarks - up, down, charm, strange, top, and bottom - are the fundamental constituents of matter and can combine to form composite particles called hadrons, the most stable of which are protons and neutrons [20].

The fermions in the SM are six quarks organized into pairs: (u, d), (c, s), (t, b), which couple to all three of the fundamental forces (strong, weak, electromagnetic), three charged leptons: e^-, ν^-, τ^-, which couple to the electromagnetic and weak forces, and three neutral leptons, the neutrinos: ν_e, ν_μ, ν_τ, which couple only to the weak force. Each of these particles has its own antiparticle.

The pairs of quarks in the SM are separated by one fundamental unit of charge, and each exists in a corresponding antimatter particle called an antiquark. Quarks do not possess any internal structure and cannot be divided into smaller constituents. They typically exist in groups of quarks or antiquarks in hadronic form, ie. protons, neutrons, and pions to create integer charges.

The leptons in the SM are fermions, thus they are also spin-$\frac{1}{2}$ particles obeying Fermi-Dirac statistics. As a result, leptons are subject to the Pauli Exclusion Principle which states that

two identical fermions cannot occupy the same quantum state simultaneously[3]. Neutrinos are electrically-neutral leptons in the SM with 0 mass and considered fundamental particles. Neutrinos are not deflected by electric or magnetic fields, since they lack electric charge and magnetic moments. These electrically neutral leptons do not interact by the strong or electromagnetic force, but only through the gravitational and weak forces. Neutrinos' weakly-interacting nature makes them difficult to detect since they rarely interact with matter.

There are three distinct neutrino flavours, electron (ν_e), muon (ν_μ), and tau (ν_τ), along with their corresponding anti-neutrinos $\bar{\nu_e}$, $\bar{\nu_\mu}$, and $\bar{\nu_\tau}$. These 6 types of neutrinos interact via the weak force, which couples the $W^\pm$ and Z^0 bosons to negative helicity neutrinos and positive helicity[4] anti-neutrinos. In the SM, neutrinos have left-handed helicities and anti-neutrinos have right-handed helicities. Right-handed helicity neutrinos and left-handed helicity anti-neutrinos, if they exist, are either very massive and/or "sterile", meaning they do not interact with any fundamental forces in the SM and interact only gravitationally. These sterile neutrinos, if existent, would interact only via gravity and not via the other fundamental interactions of the Standard Model. These hypothetical particles could be responsible for a number of unexplained phenomena in physical cosmology and astrophysics.

1.3.2 Neutrino Sources

The neutrinos in the universe originate from weak interactions (like beta decays in atomic nuclei). Three sources can be distinguished: the neutrinos from space, the neutrinos from the Earth, and the neutrinos from human activity. But there are many neutrino origins, which can be classified, as listed in Table 1.1. For each of them, various features are listed, including the flux of the neutrinos from the source on Earth's surface, the average energy of the neutrinos, and the distance of the source from Earth.

[3]For example, if two electrons reside in the same orbital, and if their principle quantum number, angular momentum number and magnetic quantum number are the same, then their spin quantum number must be different, and thus the electrons must have opposite half-integer spins of 1/2 and -1/2.

[4]In particle physics, helicity is the projection of the angular momentum, or spin, onto the direction of momentum. Left-handed or negative helicity would imply spins anti-parallel to momenta and right-handed or positive helicity would imply parallel spins to momenta.

Neutrino Source	Flux ($cm^{-2}s$)	Average Energy	Distance	Reference
Sun	3×10^{10}	0.2 MeV	1.5×10^{8} km	[21]
Earth	3×10^{5}	2 MeV	–	[22]
Reactor	3×10^{4}	4 MeV	1000 km	[22]
Relic Supernova	2.5	10 MeV	–	[23]
Galactic Supernova	10^{10}	20 MeV	10 kpc	[24]
Atmosphere	1	1 GeV	500 km	[24]
Accelerators, ν_μ	0.1	10 GeV	500 km	[24]
Accelerators, ν_τ	0.01	120 GeV	700 km	[25]
Galactic Sources	10^{-12}	3 TeV	<10 kpc	[26]
HE Neutrinos	2×10^{-12}	100 TeV	–	[26]

Table 1.1: Neutrino sources and properties. 1 kpc = 3.086×10^{16} km. Table adapted from [27].

Solar neutrinos, or those originating in the Sun, are produced by thermonuclear fusion. Their energies are low (some MeV) and they can travel long distances through space. Most of the solar neutrinos originate from the $p-p$ reaction:

$$p + p \rightarrow^{2} H + e^{+} + \nu_e \tag{1.3}$$

where p is a proton, ^{2}H is a deuterium nucleus, e^+ is a positron (anti-electron) and ν_e an electron neutrino.

The Earth is also a source of "geo"-neutrinos. Natural radioactivity in the decay chains of U, Th, and K in the Earth's crust, mantle, and core from fusion produces power on the order of 10s of TeraWatts and creates low-energy anti-neutrinos. Measurements of these could serve to shed light on the nature of the Earth's heat production mechanisms.

Neutrinos can also originate from human activity. These include the high energy neutrinos/anti-neutrinos produced by particle accelerators (GeV-scale) and low energy neutrinos produced as a by-product of nuclear fission in reactors (MeV-scale). Measurements of reactor antineutrinos have better constrained the neutrino mass oscillation parameter, Δm^2_{12} [28]. Both reactor and geo- anti-neutrinos are used for measurements of oscillation parameters and to probe the mass hierarchy of neutrinos.

Supernovae are also a source of high-MeV neutrinos. Galactic supernovae occur on average 3 times per century within the Milky Way [29]. A more detailed description of supernova neutrino origins and physics is encountered in Chapter 2 of this thesis.

High-energy cosmic rays originating in space and entering the Earth's atmosphere produce atmospheric neutrinos. When a cosmic ray (i.e. proton coming from somewhere in space) penetrates the atmosphere, it interacts with an atomic nucleus and this generates a particle shower [30].

The model of the Big-Bang predicts a cosmic background of neutrinos, relic neutrinos, which have not yet been detected due to their small energies (eV-scale). In contrast, high-energy (HE) neutrinos on the TeV-scale originate in space from galactic sources. Some PeV neutrinos have even recently been detected by the IceCube and Antares experiments [31].

1.3.3 Neutrino Oscillations

The discovery that neutrinos can change from one flavour to another and therefore have non-zero masses was a major milestone for elementary particle physics. It represented the compelling experimental evidence for the incompleteness of the Standard Model as a description of nature. Although the possibility of neutrino flavour change, i.e. neutrino oscillations, had been discussed ever since neutrinos were first discovered experimentally in 1956, it was only around the turn of the millennium that two convincing discoveries validated the actual existence of neutrino oscillations: in 1998, Takaaki Kajita of the Super-Kamiokande Collaboration presented data showing the disappearance of atmospheric muon-neutrinos, i.e. neutrinos produced when cosmic rays interact with the atmosphere, as they travel from their point of origin to the detector [30]. And in 2001/2002, the Sudbury Neutrino Observatory (SNO) Collaboration, led by Arthur B. McDonald, published clear evidence for conversion of electron-type neutrinos from the Sun into muon- or tau-neutrinos [32]. These discoveries are of fundamental importance and constitute a major breakthrough. Neutrino

oscillations and the connected issues of the nature of the neutrino, neutrino masses, and possible CP violation[5] among leptons are today major research topics in particle physics.

Neutrino oscillations were first proposed by Bruno Pontecorvo in 1957 as the quantum mechanical process in which a massive neutrino of a specific lepton flavour can later be measured to have a different lepton flavour [8]. The discovery of neutrino oscillations implies that the neutrino flavour states travel as mass eigenstates composed as a superposition of the three flavour states. Oscillations are not possible if neutrinos are massless, and so the observation of neutrino oscillations would demonstrate the massive nature of neutrinos.

Oscillations occur as the neutrino flavour eigenstates do not correspond to the neutrino mass eigenstates of the Hamiltonian in free space. Flavour eigenstates, $|\nu_\alpha\rangle$ where $\alpha \in e, \mu, \tau$, are a linear combination of the mass eigenstates, $|\nu_k\rangle$, related by the Pontecorvo-Maka-Nakagawa-Sakata (PMNS) unitary neutrino mixing matrix, $\mathrm{U}_{\alpha k}$, which is generally complex and discussed further in the next section of this chapter. The flavour eigenstates can be denoted as:

$$\begin{aligned} |\nu_\alpha\rangle = \textstyle\sum_{k=1}^{N} U_{\alpha k} \, |\nu_k\rangle \,, \\ \alpha \in e, \mu, \tau, \\ k \in 1, 2, 3 \end{aligned}$$

where N is the number of neutrino flavours. Two types of oscillations are known: vacuum (free of matter) and matter-induced.

The PMNS matrix [8] is generally expressed as a 3×3 matrix for all three neutrino species:

$$\begin{bmatrix} \nu_e \\ \nu_\mu \\ \nu_\tau \end{bmatrix} = \begin{bmatrix} U_{e1} & U_{e2} & U_{e3} \\ U_{\mu 1} & U_{\mu 2} & U_{\mu 3} \\ U_{\tau 1} & U_{\tau 2} & U_{\tau 3} \end{bmatrix} \begin{bmatrix} \nu_1 \\ \nu_2 \\ \nu_3 \end{bmatrix} \tag{1.4}$$

Vacuum Oscillations

It is empirically observed that one of the oscillation lengths is much longer than the other, or rather that one of the mass differences: $\Delta m^2_{kj} = |m^2_k - m^2_j|$ (where $k, j = 1, 2, 3$) is much larger than the

[5]CP violation is a violation of the postulated charge conjugation parity symmetry. CP is a discrete symmetry of nature given by the product of two components: charge conjugation (C) and parity (P). Charge conjugation transforms a particle into the corresponding anti-particle, i.e. charge conjugation maps matter into anti-matter. Parity is the transformation that inverts the space coordinates, producing the mirror image of reality.

other two. It is often easier to describe neutrino oscillations between two flavours. If the two neutrino masses are not identical, the mass eigenstates are different and the neutrino propagates with independently-evolving phases for the two mass eigenstates. As a result, neutrinos propagating over a distance, L, e.g. from a supernova core to Earth, will undergo different combinations of flavour eigenstates over the course of the journey. When the neutrino reaches Earth, the observed flavour is determined by a mixture of the mass eigenstates.

The Dirac equation gives the time evolution for a general neutrino state, $|\nu_k\rangle$ and means that the mass neutrino states evolve in time as plane waves:

$$|\nu_k(t)\rangle = e^{iE_k t}\,|\nu_k\rangle\,, \tag{1.5}$$

where $E_k = \sqrt{p^2 + m^2}$ are the energy eigenvalues.

The two eigenstates $|\nu_k\rangle$ and $|\nu_\alpha\rangle$ can be related by a mixing matrix:

$$U_{\alpha j} = \begin{bmatrix} \cos\theta & \sin\theta \\ -\sin\theta & \cos\theta \end{bmatrix} \tag{1.6}$$

where θ is the mixing angle in vacuum. The flavour and mass bases relate as follows:

$$|\nu_1\rangle = |\nu_e\rangle\cos\theta + |\nu_\mu\rangle\sin\theta \tag{1.7}$$

$$|\nu_2\rangle = |\nu_e\rangle\sin\theta + |\nu_\mu\rangle\cos\theta \tag{1.8}$$

From these, an expression for the survival probability of, for example, an electron neutrino can be resolved.

In the case of three massive neutrinos, the matrix U can be parametrized in terms of three Euler angles (called mixing angles) and phase parameters. If the neutrinos are Dirac fermions (and so have distinct anti-particles), only one of the phases is physical and gives rise to CP violation. If, however, neutrinos are Majorana particles (identical with their antiparticles), additional CP-violating phases are required. The PMNS matrix is often conveniently parametrized as [33]:

$$U_{\alpha k} = \begin{bmatrix} 1 & 0 & 0 \\ 0 & c_{23} & s_{23} \\ 0 & -s_{23} & c_{23} \end{bmatrix} \begin{bmatrix} c_{13} & 0 & s_{13}e^{-i\delta} \\ 0 & 1 & 0 \\ -s_{13}e^{-i\delta} & 0 & c_{13} \end{bmatrix} \begin{bmatrix} c_{12} & s_{12} & 0 \\ -s_{12} & c_{12} & 0 \\ 0 & 0 & 1 \end{bmatrix} \begin{bmatrix} e^{i\alpha_1/2} & 0 & 0 \\ 0 & e^{i\alpha_2/2} & 0 \\ 0 & 0 & 1 \end{bmatrix} \tag{1.9}$$

where $c_{ij} = \cos\theta_{ij}$ and $s_{ij} = \sin\theta_{ij}$. The angle θ_{ij} is the mixing angle between neutrino i and neutrino j. The δ term is a Dirac phase which is non-zero if neutrino oscillations violate CP-symmetry. The phase factors α_1 and α_2 are non-zero if neutrinos are Majorana particles.

From the PMNS matrix, several expressions involving the mass eigenstates in terms of the flavour eigenstates can be re-arranged to find an approximation of the oscillation probability over a finite distance. For neutrino oscillations in vacuum, the above relation allows simple derivation of the flavour change probability. The oscillation probability for ν_α to evolve into ν_β over distance L is then:

$$P_{\nu_\alpha \to \nu_\beta} = 1 - 4 \sum_{j,i>1} U_{\beta i} U^*_{\alpha i} U^*_{\beta j} U_{\alpha j} \sin^2 \left(\frac{1.27 \Delta m^2_{ij} L}{E_\nu} \right) \tag{1.10}$$

where L is the distance of travel, E_ν is the starting neutrino energy, $\Delta m^2_{ij} = |m^2_j - m^2_i|$, α and β are flavour-state indices, and i and j are mass-state indices.

Flavour Change in Matter

When electron neutrinos, ν_e, pass through matter, such as a neutrino passing through the infalling matter or condensed core of a supernova, another process can occur: the MSW (Mikheyev-Smirnov-Wolfenstein) effect. The MSW effect describes the flavour change that occurs in matter. The non-zero electron density in matter results in charged current coherent forward scattering of the electron neutrinos resulting in flavour oscillations. The muon and tau neutrinos only interact with electrons through the Z-boson, whereas the electron neutrinos can interact through either the W or Z-bosons. This results in a difference of probability for changing flavour for the electron and muon and tau neutrinos.

When neutrinos pass through the matter of a star, neutrinos created in the high-density core propagate radially outward to lower densities and eventually hit a critical density layer where

two energy eigenvalues will "cross." At this MSW resonance, at a particular electron density, the neutrino has a maximum probability of flavour change:

$$\frac{\Delta m_e^2}{2E_e}\cos 2\theta = \sqrt{2}G_F n_e \tag{1.11}$$

where E_e and m_e are the neutrino energy and mass, θ is the mixing angle, G_F is the Fermi constant and n_e is the electron number density.

The MSW effect induces a change in the oscillation probability [34]:

$$P_{\nu\to\nu_\mu} = \frac{\sin 2\theta}{W^2}\left(\frac{1.27W\Delta m^2 L}{E}\right) \tag{1.12}$$

where $W^2 = \sin^2 2\theta + \left[\sqrt{2}G_F n_e(\frac{2E}{\Delta m^2}) - \cos 2\theta\right]^2$.

The MSW effect along with vacuum oscillations describe how neutrinos change flavour as they travel through (stellar) matter. These oscillations ultimately caused a "deficit" or disappearance of electron neutrinos from the Sun on Earth, known as the *solar neutrino problem.* Electron neutrinos interact with the electrons that are present throughout the Sun's layers, and the electron density of the Sun varies adiabatically as neutrinos travel radially outward. This slowly-varying electron density causes a a high conversion probability at the critical electron density corresponding to the MSW resonance of electron neutrinos to ν_2. Thus, only a third of the number of expected electron neutrinos were detected from the Sun on Earth via charged current reactions. This deficit was explained by neutrino measurements of solar neutrinos by the SNO experiment which were consistent with the presence of the MSW effect in the Sun [17].

1.3.4 Neutrino Mass Limits

Neutrino oscillation and MSW observations confirmed that neutrinos do actually have a non-zero mass and gave a lower limit on the mass. The absolute scale of neutrino mass has not been directly measured, yet upper limits have been obtained from both tritium beta decay experiments and cosmology.

To date, an upper limit on the electron (anti)neutrino of 2.2 eV (95% C.L) has been obtained from tritium beta decay experiments [35] [36]. The KArlsruhe TRItium Neutrino, (KATRIN), experiment aims to lower this limit to $m_\beta < 0.2$ eV [37] [38]. The muon neutrino has an upper

limit of 190 keV (90% C.L) and the tau neutrino has an upper limit of 18.2 MeV (95% C.L.) [39].

1.3.5 Neutrino Interactions

Neutrinos only experience the weak force, and there are three categories of possible interactions with matter that neutrinos may undergo: neutral current, charged current, or a combination of both: elastic scattering. These will also be discussed in Chapter 3 with regard to neutrino interactions in the SNO+ detector.

Charged current reactions are reactions that involve the exchange of a $W^{\pm}$ boson. Through the emission of a virtual W^{+} boson, an up quark can become a down quark, while the emission of a W^{-} boson will convert a down quark to an up quark. It is by these two processes that a proton is converted to a neutron and vice versa. In a charged current interaction, a charged lepton is produced as well as a neutrino. The reaction has an energy threshold corresponding to the difference between the summed masses of the initial state particles and the summed masses of the final state particles. Because the mass of a muon is 105.6 MeV and the mass of a tau is 1776.8 MeV, while the energy of supernova and solar neutrinos are significantly less, muon and tau neutrinos produced in a supernova will not undergo charged current interactions.

Neutral current reactions are mediated by the neutral Z^{0} boson and hence do not involve any change in charge of the participating particles. Unlike charged current interactions, no charged lepton is produced in neutral current interactions.

All flavours of neutrinos will scatter elastically off of electrons. Other neutrino flavours will only interact through the neutral current channel and so possess a smaller scattering cross section.

1.3.6 Majorana Neutrinos and Neutrinoless Double Beta Decay

In the Standard Model of particle physics all fermions (quarks, leptons and neutrinos) have their distinct anti-particle. Such particles are called Dirac fermions. Since the neutrino doesn't carry electric charge, in principle it is possible for it to be its own anti-particle, which would hint at more physics beyond the Standard Model. This possibility was first considered by Ettore Majorana and W. H. Furry in 1937 and 1939, respectively [40]. Therefore these kind of particles are called Majorana fermions.

If neutrinos are Majorana particles, then anti-neutrinos are simply neutrinos with right-handed helicity. In this case, the emission of a neutrino is identical to the absorption of an anti-neutrino, and *vice versa*. This property implies that a hypothetical physical process known as neutrinoless double beta decay is allowed if the neutrino is a Majorana particle.

Single beta decay takes place when a free or nucleus-bound neutron decays to a proton, an electron and an electron anti-neutrino: $n \rightarrow p + e^- + \bar{\nu}_e$. The decay is mediated by the W boson. This process balances charges since the beginning neutron is neutral, the proton is positive, and the electron is negative, summing to zero. It also increases the number of protons in the nucleus by one (Z becomes (Z+1)), and decreases the neutron number by one. For some nuclei, this is impossible since the nucleus with these changes has more mass than the starting nucleus. Yet in some cases, if another beta decay occurs at the same time, leading to the Z+2 nucleus with less mass than the starting nucleus, then double beta decay or $2\nu\beta\beta$-decay, is energetically allowed (see Figure 1.2). The Feynman diagram for this process is seen in Figure 1.3. Since the weak process of beta decay takes a long time, two simultaneous beta decays into exactly the required energy difference between nuclear masses takes much longer.

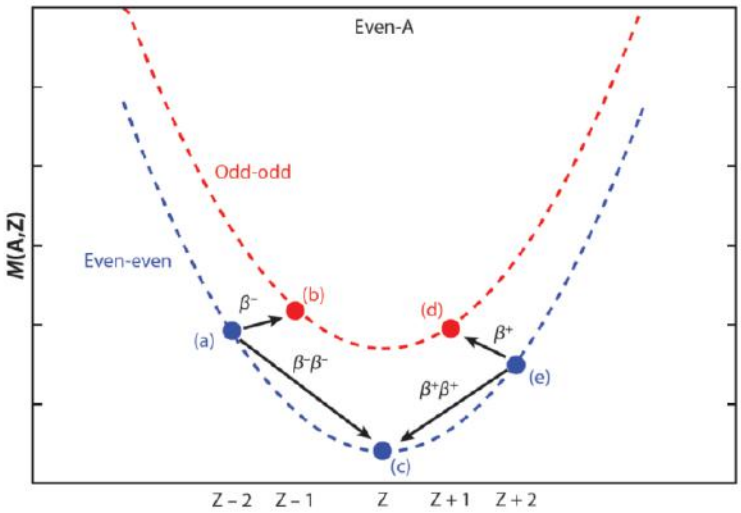

Figure 1.2: Mass parabolas for nuclear isobars with even A with Z protons, N neutrons. Even-even nuclei have lower masses than odd-odd nuclei. Single β-decays of some isotopes are forbidden (i.e. point (a) to point (b)) as it is not energetically-favourable for the daughter energy level to be higher, but 2β-decay is energetically possible as a second-order process from point (a) to point (c) [41].

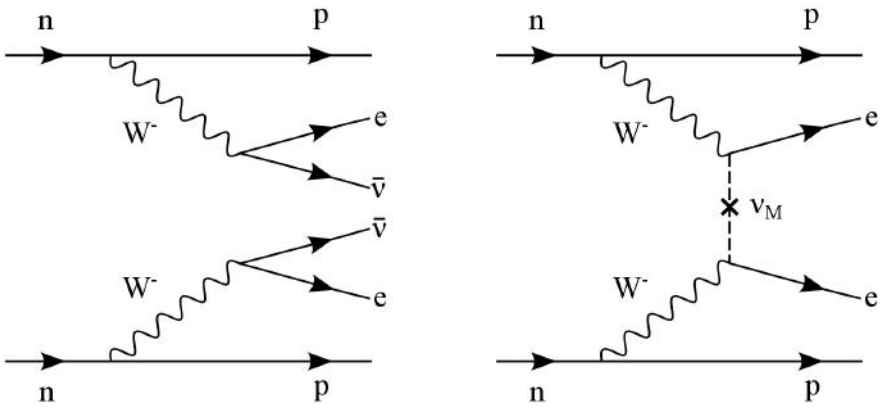

Figure 1.3: Feynman diagram of the elementary particle transition which induces $0\nu\beta\beta$-decay. $0\nu\beta\beta$-decay can only occur if the neutral neutrino is its own anti-particle. The decay process is mediated by the W-boson. In that case, the anti-neutrino which is emitted from the first beta decay, is really also the incoming neutrino to hit a neutron and produce another electron and a proton. This process has two neutrons converting to two protons and emitting two electrons, but not emitting any neutrinos.

Neutrinoless double-beta, or $0\nu\beta\beta$, decay is the yet unconfirmed nuclear process in which two neutrons in a nucleus are converted to two protons via the exchange of two W bosons without the emission of two neutrinos; the Feynman diagram for the process is also shown in Figure 1.3 along with the ordinary $2\nu\beta\beta$ decay. In order for neutrinoless double-beta decay to be possible, the neutrino must be a Majorana particle, that is, it must be its own antiparticle. In neutrinoless double-beta decay, one neutrino is emitted at one reaction vertex and absorbed as an antineutrino, at the other. Whereas ordinary double beta decay involves the emission of two neutrinos, if the neutrino is its own anti-particle (opposite helicity), then this can be replaced with the exchange of a (virtual) neutrino; equivalently, one can think of this as the two emitted neutrinos annihilating with each other. Neutrinoless double beta decay would violate lepton number conservation as there are unbalanced leptons on either side of the reaction.

Neutrinoless double beta decay can be seen as two simultaneous β-decays, in which two neutrons are converted into two protons and two electrons, as the neutrinos from the two weak vertices mutually annihilate. The unique signature of this theoretical process is a discrete peak at the Q-value of the reaction in the summed energy spectrum of the two outgoing electrons as seen in Figure 1.4, which is the mass difference between the mother and daughter nuclei minus two electron masses. Since no neutrinos would leave the nucleus, they would not carry away any energy. The measured quantity is then the half life of the decay.

Ordinary double-beta decay, $2\nu\beta\beta$ is identifiable in isotopes where a single beta decay is energetically forbidden. Because of energy conservation of certain nuclei, e.g. ^{130}Te, cannot decay via beta decay, but only via double beta decay ($2\nu\beta\beta$). There are 35 naturally occurring isotopes for which double-beta decay is observable. However, only eleven isotopes with Q-values beyond 2 MeV are considered for experimental searches due to background constraints.

Since $2\nu\beta\beta$-decay is a rare, 2nd-order weak process, its half-life is long: $T_{1/2} = 2.11 \pm 0.21 \times 10^{21}$ yr for the isotope ^{130}Te [42]. In fact, double beta decays are the rarest processes ever observed up to now. In comparison, the age of the universe is $T = 13.798 \pm 0.0037 \times 10^9$ yr [43]. For ^{130}Te, double beta decay to ^{130}Xe is allowed with $Q_{\beta\beta} = 2527.518 \pm 0.013$ keV, roughly 2.5 MeV at the endpoint of the $2\nu\beta\beta$ spectrum [44]. SNO+ will be using ^{130}Te for its search of neutrinoless double beta decay. This is discussed further in Chapter 3.

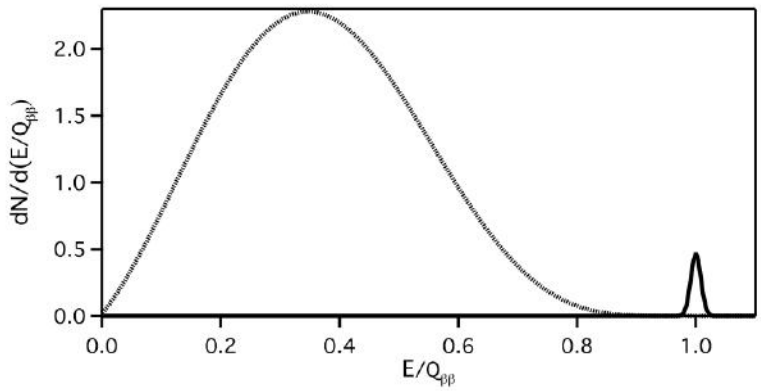

Figure 1.4: Spectra of the sum of electron energies for $2\nu\beta\beta$ (dotted curve) and $0\nu\beta\beta$ (solid curve). The curves were scaled and drawn for a 1-σ energy resolution of 2% [45].

Understanding the Majorana nature of neutrinos is one of the most active areas of research in modern neutrino physics. In particular, $0\nu\beta\beta$-decay can address the issues of lepton number non-conservation, the particle-antiparticle nature of the neutrino, and the absolute mass scale of the neutrino. If neutrinoless double beta decay were to be observed, it would demonstrate lepton number violation. One of the main physics goals of the SNO+ experiment at SNOLAB is to determine whether the neutrino is a Dirac or Majorana particle. ^{130}Te has been selected for use in SNO+'s search for $0\nu\beta\beta$-decay. A successful observation of neutrinoless double-beta decay and measurement of the rate would allow a conclusive statement concerning the Majorana nature of the

neutrino to be made and would also provide a measure of the effective neutrino mass. Searches for neutrinoless double beta decay, such as with the SNO+ experiment, are thus the a very promising path to further determining the nature of the neutrino.

Chapter 2

Fundamentals of Core-Collapse Supernovae

2.1 Introduction

Supernovae (SNe; singular SN) are the energetic explosions of dying stars which can outshine entire galaxies. Massive stars, between 8-40 solar masses ($M_\odot$) evolving in isolation, typically undergo gravitational collapse, the inward collapse of the core of a massive star which has exhausted its nuclear fuel. These core-collapse supernovae (CCSNe) events make up some of the most energetic events in the universe and leave behind compact remnants such as neutron stars or stellar mass black holes. It is estimated that <1% of the gravitational binding energy of the former star is carried away by the supernova optical signal and the kinetic energy of the explosion, while >99% is converted into neutrinos and antineutrinos of all flavours which leave the star [46].

Since Baade & Zwicky's prediction that "a supernova represents the transition of an ordinary star into a neutron star" over 80 years earlier [47], great efforts have been invested in understanding supernovae and their ejecta. The very basics of CCSNe theory, summarized by Bethe in 1990 [48], were confirmed by the observation of only a few neutrinos from SN1987A [49],[50]. No measurements of CCSNe neutrinos have been made since.

The explosion mechanism of massive progenitors remains a puzzle, and might involve the not-fully-explored properties of neutrinos [51]. Even in the lack of a complete theory of core-collapse

supernova explosions, the neutrino emission from the event is believed to be well established. Future detection of neutrinos from the next supernova event in the Milky Way (MW) Galaxy would bring a wealth of information as neutrinos are particularly well-suited as probes of the nature of cosmological objects and their dynamics. The weakly-interacting particles can escape in-falling matter during core collapse and emerge hours ahead of the optical signal, traversing the interstellar medium (ISM) essentially unhindered, and thus acting as interstellar messengers which conserve the directionality and energetic characteristics of their origin. The early observation of the supernova light curve turn-on will bring information about the progenitor and its environment, and possibly the opportunity to learn more about the nature of the core collapse (e.g. study of the explosion mechanism, black hole formation, accretion disks, explosive nucleosynthesis). It could also provide valuable feedback on neutrino properties themselves such as the absolute mass, mass hierarchy and neutrino mixing since many neutrinos can be measured from one supernova event. See [52] for more information on mass measurements of supernova electron neutrinos.

A future core-collapse supernova in our Galaxy will be detected by several online neutrino detectors around the world. SNEWS is network of neutrino detectors whose aim is to provide early warning of a supernova's occurrence and improve global sensitivity to the neutrino burst via inter-experiment collaboration. The onset of a supernova has not yet been detected with an electromagnetic signal, thus SNEWS will be able to provide early recognition for an event. As of 2016, the current detectors capable of detecting supernova neutrinos and members of SNEWS are Borexino, IceCube, LVD, Super-Kamiokande (Super-K), Daya Bay, KamLAND, and HALO (the dedicated supernova detector located at SNOLAB). SNO+ will also be capable of detecting supernova bursts and will become a member of SNEWS once fully online.

2.2 Supernovae Classification

Classification of SNe is generally performed based on the optical spectra, and SN types are assigned on the basis of the chemical and physical properties of the outermost layers of the exploding stars. Figure 2.1 displays the current supernovae classification algorithm. The two main classes of SNe, types I and II, were firmly established by Minkowski *et al.* in 1941 [53] and are assigned on the presence or absence of hydrogen in the supernova's spectra. SNe lacking H lines are labeled type I

(SNI), while those with an obvious presence of H lines are labeled type II (SNII).

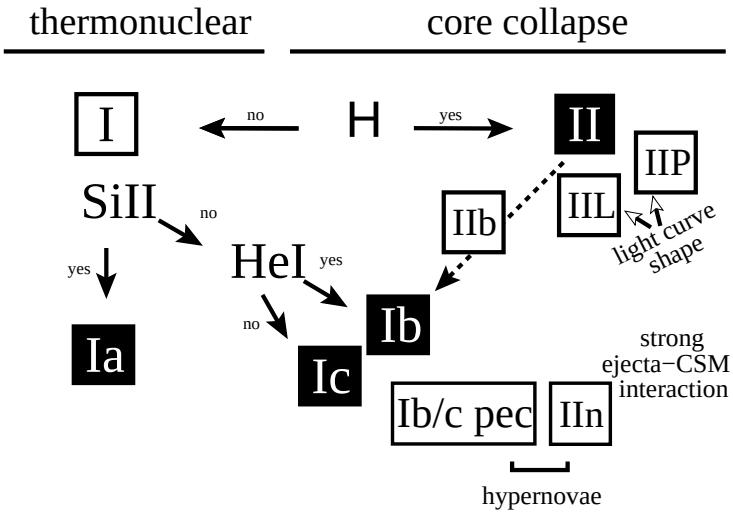

Figure 2.1: The current classification scheme of supernovae which is based on the observation of spectral lines and light curves. Type Ia SNe are associated with the thermonuclear explosion of accreting white dwarfs while the other SN types (Type II and Ibc) are associated with the core collapse of massive stars. Figure taken from [20].

Type I are subdivided by the presence or absence of Si. Those with Si in their spectra are labeled the "classical" type Ia SNe and most Type I SNe fall in this category. Type Ia have a consistent light output and are often referred to as "standard candles" for determining distance scales in the Universe. The SNe without Si in their spectra can be further categorized by the presence or absence of He. SNe containing He are labeled Ib, and those without are labeled Ic. In several contexts, both SN lacking the Si spectral feature are referred to simply as SNIbc[1]. Type Ibc are likely produced by the same gravitational collapse mechanism as Type II, except that the progenitors were stripped of their hydrogen (SN Ib) and possibly helium (SN Ic) envelopes prior to exploding, either via mass transfer to companion stars or through winds.

Type II SNe are characterized by the obvious presence of H in their spectra. These SNe are strongly associated with regions of recent star formation and the core collapse of massive stars. Type II SNe can occur for O/Ne/Mg and Fe cores. While the luminosity peaks of Type II SNe tend to be less than the brighter Type I, they do reach high enough temperatures to pair-produce neutrinos, and the tails of their light curves extend for longer periods of time. Four subclassifications

[1]Type Ibc SNe: Classification into Ib or Ic categories can be ambiguous, thus Ibc is often used as an umbrella term for both.

are made (IIb, IIP, IIL, and IIn) according to the shape of the optical light curves and their time evolution. The spectra of a Type IIb SN can evolve into that of a Type Ib SN. Type IIP/L are subdivided by either having **n**arrow or intermediate-width lines (Type IIn) or not having them (Type IIP/L) and a light curve that reaches a **p**lateau or displays a **l**inear decrease. Some Type Ibc and IIn SNe with explosion energies $E > 10^{52}$ erg are often called "hypernovae." For Type In SN in the intermediate width case, the ejecta from the explosion may interact strongly with gas around the star (ie. the circumstellar media (CSM)).

It should be mentioned that several stellar objects do not fit the current schema, though in many cases are probably core-collapse SNe exploding in unusual configurations and/or conditions. For example, the recent SN2000er was classified as peculiar, but is hypothesized to be a core-collapse SN which lost its He envelope shortly before explosion [54].

2.3 Supernovae Progenitors

The types of explosion and remnant each supernova produces depends chiefly on the mass of the star progenitor and its metallicity[2]. Figure 2.2 maps, as a function of mass and metallicity, where black holes and neutron stars are likely to form and where different types of supernovae are produced.

SN Ia begin in an evolved binary system where at least one star is a white dwarf consisting mainly of carbon and oxygen and the other is either a red supergiant, main sequence star, or another white dwarf. Prior to explosion, the white dwarf accretes matter from its companion star and converts it to helium. Once the white dwarf reaches the Chandrasekhar limit of 1.4 $M_\odot$[3], a thermonuclear explosion is ignited. These supernova events produce negligible neutrino emission since nuclear burning does not reach high enough temperatures to produce neutrino reactions. Progenitor stars for Type Ia SN are not particularly massive since they evolve into white dwarfs and additional mass is required to produce the explosion instability. The progenitor masses of Type Ia SNe fall below ∼1.4 $M_\odot$ (See Fig. 2.2 low mass star region for white dwarfs). In these thermal runaway SNe, most of the explosion energy is transferred into heavy element synthesis instead and

[2]In astronomy and physical cosmology, the metallicity, or Z, is the fraction of mass of a star (or other astronomical object) that is not hydrogen and helium. Most of the physical matter in the universe is in the form of hydrogen and helium, so astronomers conveniently use the blanket term "metals" to refer to all other elements. Metallicity within stars is an approximate estimation of their chemical abundances that change over time by the mechanisms of stellar evolution, thus providing an indication of their age.

[3]See Section 2.6.3 for explanation of the Chandrasekhar limit.

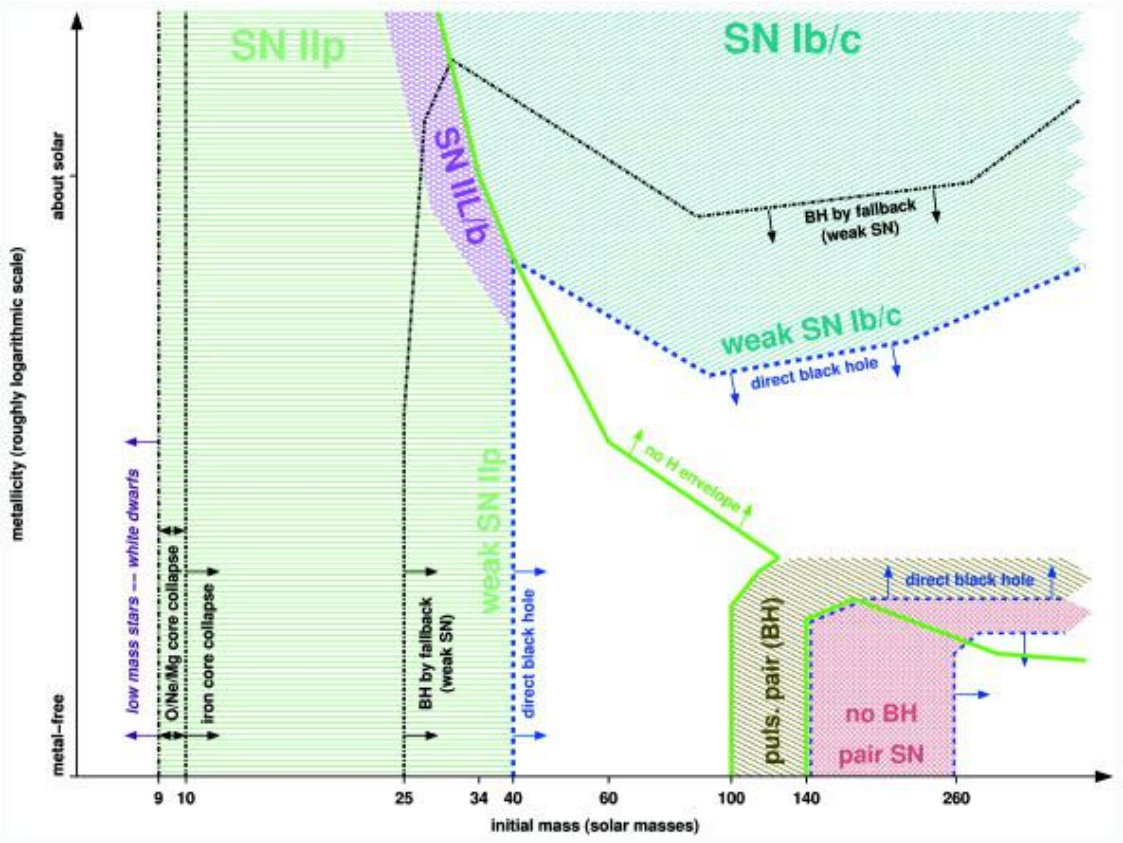

Figure 2.2: Supernovae types of non-rotating massive stars as a function of initial metallicity (*y-axis, qualitatively*) and initial mass (*x-axis*). The thick green line separates the regimes where the stars keep their hydrogen envelope (left and lower right) from those where the hydrogen envelope is lost (*upper right and small strip at the bottom between 100-140* $M_\odot$). The dashed blue line indicates the border of the regime of direct black hole formation (*white*). Light green horizontal hatching indicates the domain where Type IIp supernovae occur. At the high-mass end of the regime they may be weak and observationally faint because of fallback of ^{56}Ni (*black line*). These weak SN Type IIp should preferentially occur at low metallicity. At the upper right-hand edge of the SN Type II regime, close to the green line of loss of the hydrogen envelope, Type IIL/b supernovae that have a hydrogen envelope of $\lesssim 2$ $M_\odot$ are made (*purple cross-hatching*). In the upper right-hand quarter of the figure, above both the lines of hydrogen envelope loss and direct black hole formation, Type Ib/c supernovae occur; in the lower part of their regime (*diagonal dark green cross-hatching*) they may be weak and observationally faint because of fallback of ^{56}Ni, similar to the weak Type IIp SNe. In the direct black hole regime, no "normal " (non–jet-powered) supernovae occur since no SN shock is launched. An exception are pulsational pair-instability supernovae (*lower right-hand corner; brown diagonal hatching*) that launch their ejection before the core collapses. Below and to the right of this we find the (non-pulsational) pair-instability supernovae (*red cross-hatching*), making no remnant, and finally another domain where black holes are formed promptly at the lowest metallicities and highest masses (*white*) where no SNe are made. White dwarfs do not go supernova as a single star (*white strip at the very left*). Figure and caption taken from [55].

kinetic energy of the ejecta instead of the thermal creation of neutrinos.

Progenitors with masses between (9-10) $M_\odot$ have an O/Ne/Mg core that can withstand the inward gravitational pressure by its own outward electron degeneracy pressure. However, the density in the core can increase by He and H shell burning, which leads to increased electron capture on core elements and reduces degeneracy pressure. These progenitors eventually undergo gravitational core collapse Type IIp SNe and turn into a neutron star. These SNe are associated with the emission of neutrinos.

SNe associated with Fe core collapse are thought to arise from evolved, massive progenitors with initial masses (10-100) $M_\odot$ which leave a neutron star or in some cases a black hole when the progenitor mass exceeds 25 $M_\odot$ [56]. For lower masses $\sim$(10-40) $M_\odot$, collapse results in Type IIp SNe which make up about 60% of all core-collapse SNe (CCSNe) releasing neutrinos and are often referred to simply as CCSNe and will thus be the focus of this work. For moderate to high metallicities, progenitor masses can extend to result in Type Ibc SNe. At masses greater than $\sim$40 $M_\odot$, a direct black hole can result since the star is too massive to launch a shock wave.

Massive progenitors beyond 100 $M_\odot$ with low metallicities undergo pulsational pair instability from electron-positron pair production via high-energy photons. These cores become unstable when these reactions reduce the internal thermal pressure allowing core collapse (See [55] for more explanation on pair-instability supernova). In the case of black-hole formation after pair-instability, an energetic emission and subsequent cut-off of neutrinos occurs, but this is assumed to be < 1 % of all CCSNe cases.

At the highest masses and low metallicities above 260 $M_\odot$, gamma rays can be produced by the hot core, which can lead to photodisintegration eventually leading to a black hole without a SN occurring. Supermassive black holes can occur for stars reaching $>10^5$ $M_\odot$.

2.4 Progenitor Locations

The types of galaxies in which SNe occur provide important clues as to their nature and to the mass of their progenitor stars. Galaxies are classified into three general types based on their shape: elliptical (En), spiral ($Sa/b/c/d$), and irregular. A fourth type, lenticular ($S0$), has been used to

classify those galaxies which have both spiral and elliptical features.[4] [58] The Milky Way galaxy is classified as a spiral *Sbc* galaxy.

Type Ia SNe are found in all types of galaxies, but mainly in elliptical (*En*). Of the few supernovae that do occur in elliptical galaxies, essentially all are of Type I with no contribution from other types. Therefore a neutrino burst due to gravitational collapse is not expected from elliptical galaxies. Most supernovae occur in spiral and irregular galaxies because of the large population of massive stars in those types of galaxies. Type II occur almost exclusively in the arms of spiral (*Sa/b/c/d*), where stars are more likely to be massive. Type II and Ibc have never been seen in *En* and rarely if ever in lenticular (*S*0) [57], and are generally in or near spiral arms [58], implying that their progenitors must have started their lives as massive stars ($\gtrsim$ 8-10 $M_\odot$).

2.5 Galactic and Extragalactic Supernovae Rates

Various methods have been used to determine the supernova rates in our galaxy such as the observation of historical galactic (Milky Way) and extra-galactic supernova, the observation of supernova remnants, the estimation of the iron abundance of the universe (assuming that a large fraction of it was manufactured by previous SNe), stellar evolution rates, and neutrino detection limits.

CCSNe are extremely rare events that are not reliably predictable and have prompted many groups to attempt to measure the rates of SN in local galaxy clusters. Supernova data from other galaxies can also be used to predict the frequency of supernova within our own (Milky Way Galaxy). Neutrino detectors, in particular, are sensitive to bursts from very near galaxies outside the MW. Two small satellite galaxies outside the Milky Way called the Large Magellanic Cloud (LMC) and the Small Magellanic Cloud (SMC) exist. Beyond the Magellanic Clouds there are effectively no stars until reaching Andromeda, the next neighbouring galaxy at a distant 890 kpc. Thus, the expected frequency of CCSNe in these nearby galaxies is remarkably low, on the order of every 200 years for the LMC and 900 years from the SMC.

In summary, a wide range of values are suggested in the literature for the mean interval time of supernovae within the Milky Way based on prediction models, star populations, and historic supernova rates. Tammann *et al.* suggest that the combined estimate for the total galactic su-

[4] See [57] for explanation of the Hubble Sequence classification system and cosmic supernova rates.

pernova rate is $2.5^{+0.8}_{-0.5}$ supernova per century [29]. Others have suggested a rate of $3.2^{+7.3}_{-2.6}$ per century for Galactic CCSNe [59]. As 80% of these are expected to be Type II and Ib supernovae, the widely-accepted range that a supernova neutrino burst could occur is every 30-50 years [60]. Combining the galactic and extragalactic frequencies, the estimated frequency of CCSNe events (Type Ib/c and Type II) has is roughly one burst every 37 years or ∼3 times per century [29].

2.6 Dynamics of Iron Core-Collapse Supernovae

The underlying processes that give rise to Type I and Type II supernovae are different, however their explosion energies are quite similar. During thermonuclear Type Ia SNe, most of the explosion energy is transferred into heavy-element synthesis and ejecta kinetic energy, whereas Type II and Ibc SNe transfer nearly all of their gravitational potential energy into the form of neutrinos. Since supernova of Type Ibc and Type II are known to generate a substantial supernova neutrino signal and make up the majority of CCSNe, this subchapter will focus on those as opposed to Type Ia SNe arising from explosive thermonuclear burning. This section will describe the evolution of a star from its birth to death by the gravitational collapse mechanism as based on current models. The focus will also be on iron core collapse due to the prevalence of that process in neutrino-emission supernovae. Particular reference is made to [61],[51],[62],[63], and [64].

2.6.1 Stellar Formation & Classification

Star formation occurs when matter condenses from an interstellar cloud consisting of mainly hydrogen and helium among other elements. The protostar contracts under the influence of gravity, converting gravitational potential energy to thermal energy, until the core temperature is high enough to ignite hydrogen "burning," essentially nuclear fusion. A protostar continues to grow by accretion of gas and dust from the surrounding cloud until reaching stability.

Most commonly, stars are characterised from observing their luminosity, spectral class and/or surface temperature. The Hertzsprung-Russell diagram plots solar luminosity[5] vs. star color (temperature) ranging from the high-temperature blue-white stars on the left to low temperature red stars on the right (See Figure 2.3).

[5]One solar luminosity $\mathcal{L}_\odot$ is 3.846×10^{26} W or 3.846×10^{33} erg/s.

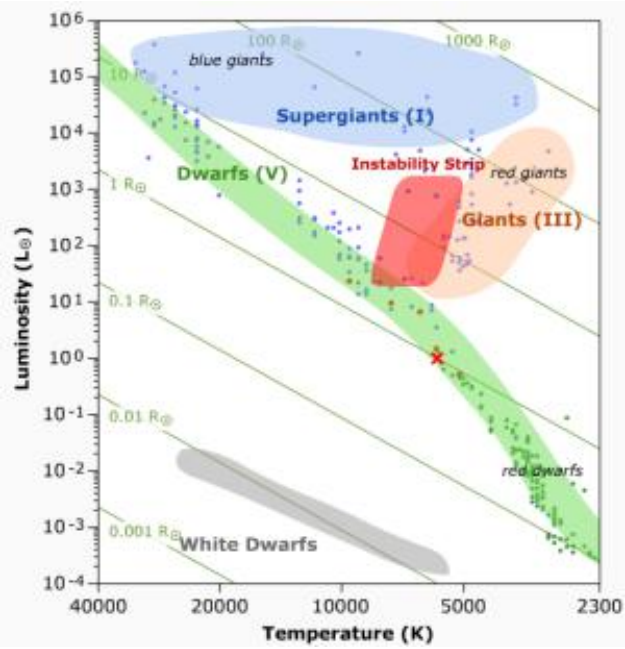

Figure 2.3: The Hertzsprung-Russell (H-R) diagram plotting star luminosity vs. temperature. Cooler, dimmer stars are placed towards the lower right and hotter, more luminous stars towards the upper left. Our Sun is marked by an "X" and falls along the Main Sequence (*green diagonal strip*) along with most other stars during the course of their lives. The more massive the star, the greater the luminosity and temperature. Stars of smaller mass, like the Sun, burn at a lower temperature and luminosity for longer periods of time. Stars are often listed with an associated roman numeral from I to V as a measure of the size and luminosity of the star. Classification by letters according to spectral type is also common, in order from hottest to coolest, O, B, A, F, G, K, and M (*not shown*). Our Sun is a GII star. Diagonal lines represent $\mathcal{L}$-T relations for constant star radii [65].

The ordinary hydrogen-burning dwarf stars like the Sun are found in a band running from top-left to bottom-right called the "Main Sequence." The stars which lie along this nearly straight diagonal line are known as Main Sequence stars, and these account for about (80-90)% of the total stellar population. Giant stars form their own clump on the upper-right side of the diagram. Above them lie the much rarer bright giants and supergiants. At the lower-left is the band of white dwarfs. These are the dead cores of old stars which have no internal energy source and over billions of years slowly cool down towards the bottom-right of the diagram. Some stars have times in their evolutionary track where they are not in equilibrium. These stars pulsate, expanding and contracting depending on the relative states of their thermal pressure vs. gravitational force. When stars are in this state of imbalance or instability, they are crossing an area called the Instability Strip. This is an area around 1000K wide that sits above the Main Sequence, as shown in the

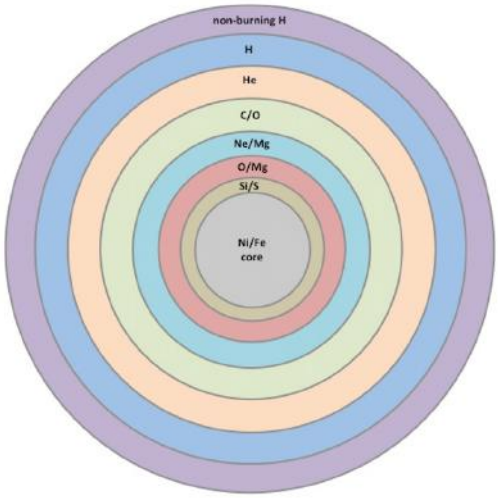

Figure 2.4: Schematic concentric shell structure of a Type II supernova progenitor prior to collapse of the Fe core. The burning stages are labeled from iron-nickel to hydrogen-helium. There is a non-burning H outer mantle. In reality, the frontiers between zones are not that sharp due to convection processes. Only the most abundant elements are indicated (Ar, Cr, Ti, and Ca are not shown). Shell layer colors are arbitrary and not to-scale.

Fig. 2.3 (*red strip*). During most of the star's lifetime, it is located along the Main Sequence at a position determined primarily by its mass. All Main-Sequence stars are in hydrostatic equilibrium, where outward thermal pressure from hydrostatic burning is balanced by the inward gravitational pressure from the overlying layers. As the star ages, it may become a giant or supergiant once its hydrogen fuel is consumed. After a star goes supernova, they typically become white dwarfs or neutron stars.

2.6.2 Pre-supernovae Star

At the end of hydrostatic burning, a massive star consists of concentric shells that are the relics of its previous burning phases (typically hydrogen, helium, carbon, neon, oxygen, silicon) (See Figure 2.4). Over tens of millions to billions of years, the thermal pressure from these nuclear burning reactions provides a balancing force to counteract the inward gravitational attraction, resulting in a state of hydrostatic equilibrium. Iron is the final stage of nuclear fusion in hydrostatic burning, and, since it cannot further fuse under pressure, the end result is a highly compact iron core. The fusion of hydrogen and helium take millions of years, but the last stage of silicon burning only lasts for several weeks. The iron core collapse occurs in the span of only $\sim$10 ms., releasing $\mathcal{O}(10^{15}$ solar units) of neutrinos during this short time period. The timeline of the various burning stages along with their estimated neutrino emission for a 15 $M_\odot$ star are listed in Table 2.1. The neutrino losses increase with the star's lifetime through its burning stages of H to Si until reaching iron core collapse.

Stage	Time Scale	Fuel	Product	Temp. (10^9 K)	Density (g/cm^3)	Luminosity, $\mathcal{L}_\odot$ (10^{31} W)	Neutrino Losses (solar units)
Hydrogen	11 My	H	He	0.035	5.8	1.1	1800
Helium	2 My	He	C, O	0.18	1390	1.7	1900
Carbon	2000 y	C	Ne, Mg	0.81	2.8×10^5	2.8	3.7×10^5
Neon	0.7 y	Ne	O, Mg	1.6	1.2×10^6	2.9	1.4×10^8
Oxygen	2.6 y	O, Mg	Si, S, Ar, Ca	1.9	8.8×10^5	2.9	9.1×10^8
Silicon	18 d	Si, S, Ar, Ca	Fe, Ni, Cr, Ti	3.3	4.8×10^7	2.9	1.3×10^{11}
Iron Core (*Collapse*)	<1 s	Fe, Ni, Cr, Ti	Neutron Star	≥ 7 .1	$\geq 7.3 \times 10^9$	2.9	$\geq 3.6 \times 10^{15}$

Table 2.1: Evolution of a 15 $M_\odot$ star from its burning stages to its non-burning stage of collapse. Neutrino losses are integrated over the time scale of each stage. Adapted from [61].

2.6.3 Core Collapse

When the iron core, formed in the center of the massive star, grows by silicon shell burning to a mass around the Chandrasekhar limit [66] given by:

$$M_{Ch} \simeq 1.457 \left(\frac{2}{\mu_e}\right)^2 M_\odot = 5.828 \mu_e^{-2} M_\odot \tag{2.1}$$

where μ_e represents the ratio of atomic mass to atomic number (A/Z) or the mean molecular weight per electron, electron degeneracy pressure can no longer stabilize the core under the pressure exerted due to gravity, and it collapses. This begins what is called a core-collapse supernova in which the star eventually explodes and parts of the star's heavy-element core and outer shells are ejected into the Interstellar Medium (ISM). This mass limit is dependent on star composition (not density), and for an iron-nickel core, the mass limit if $M_{Ch} \sim 1.2$ $M_\odot$.

2.6.4 Neutronization

The onset of core compression induces various large-scale nuclear processes. Photodisintegration is believed to be the dominant process in higher mass stars and contributes to core de-stabilization via the reactions:

$$\gamma + {}^{56}\mathrm{Fe} \rightarrow 13\,{}^{4}\mathrm{He} + 4n \tag{2.2}$$

$$\gamma + {}^{4}\mathrm{He} \rightarrow 2p + 2n \tag{2.3}$$

This breakdown of Fe nuclei creates free neutrons at the expense of thermal energy, thus the support against gravitational pull diminishes, further allowing the core to contract.

As temperature and density in the core rises, the rate of electron capture on heavy element protons and the protons produced by photodisintegration increases:

$$e^{-} + p \rightarrow n + \nu_e \tag{2.4}$$

This is also referred to as *neutronization* as the reaction produces excess neutrons. While the star is still collapsing, a large fraction of the weakly-interacting electron neutrinos produced by these captures are able to escape from the infalling matter to the ISM since the neutrino mean free path is much greater than the size of the star. This high-luminosity neutrino "burst" at core-collapse, carries away the gravitational binding energy in the form high-energy ν_e ($\mathcal{O}(\sim 10^{52}$ erg)) as seen in Figure 2.5 before core bounce at t = 0 ms. In this phase, the neutrinos escape freely and with increasing luminosity. This outflux of particles reduces the overall number of particles in the core leading to further neutronization of the matter and further collapse.

The core-collapse model by Buras *et al.* is used to depict the neutrino luminosity and energy signal from a 15 $\mathrm{M}_{\odot}$ progenitor star from collapse onset to protoneutron star (PNS) cooling. Core collapse is seen prior to $t = 0$ ms at core bounce. The initial burst of high-energy ν_e is seen prior to core bounce, followed by a small dip in $\mathcal{L}_{\nu_e}$ just after the initial rise. This dip in the asymptotic luminosity signals the end of the infall/collapse phase of the supernova.

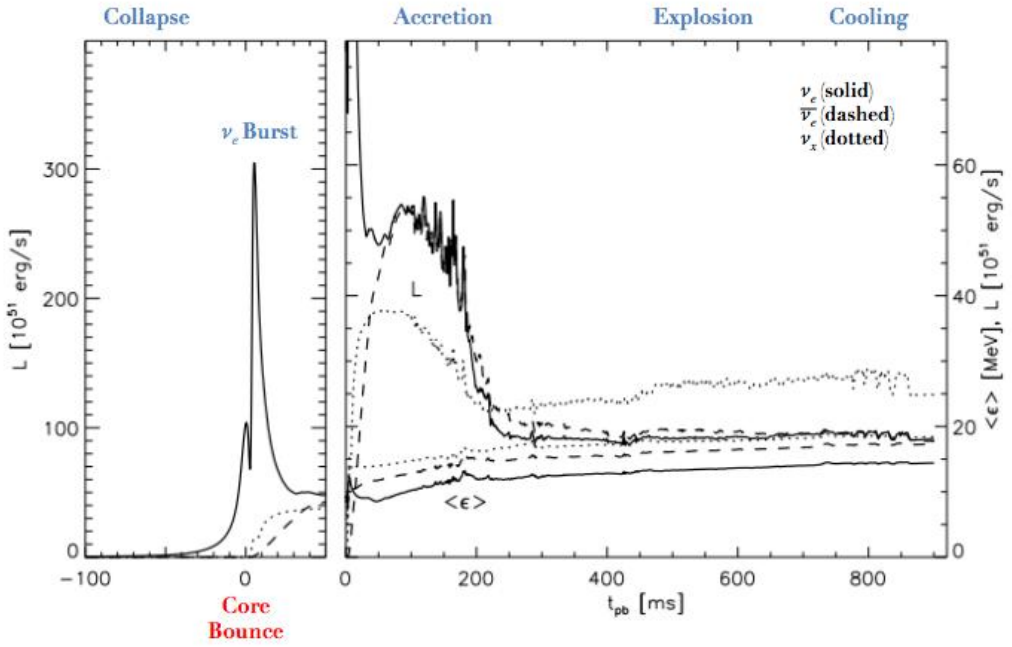

Figure 2.5: Model plotting neutrino luminosity as a function of time derived from a 2D hydrodynamic core-collapse supernova simulation of a 15 $M_\odot$ star. The SN neutrinos, ν_μ, ν_τ, $\bar{\nu}_\mu$ and $\bar{\nu}_\tau$ are grouped together as "ν_x" since they can only interact via the flavour and particle type independent neutral current (NC) reaction. If none of the flavours or types is distinguishable, the neutrinos are labeled as simply "x". The portion of the plot is described by a coarse luminosity scale, ranging from (0-400)$\times 10^{51}$ erg/s, for a zoomed-in time region near core bounce. The right portion of the plot has a zoomed-out time axis and fine luminosity scale (0-80)$\times 10^{51}$ erg/s from average energy value scale to show the features of the luminosity after core bounce. The right plot also shows the scaling for the average energy, $< \epsilon >$, of the neutrino flavours, which range from 12-20 MeV. Prior to core bounce at 0 s., the generation of hydrostatic pressure by thermal fusion declines with Fe core growth. Eventually, the core collapses under its own gravity and neutronization produces an initial burst of high-energy ν_e. The inner core eventually decelerates and bounces, colliding with the infalling matter. This disintegrates material into free nucleons leading to increased electron capture reactions and ν_e creation. During the accretion phase, the remaining supersonically-infalling star matter heats the nascent protoneutron star while other ν-species (indicated by arbitrary ν_x and $\bar{\nu}_x$ where x can be μ or τ flavour classes) are thermally created and escape. In the cooling phase, infalling matter reverses at the point of explosion (exact mechanism uncertain), and slow spectral softening of neutrino species occurs. The SN remnant then evolves to a neutron star (black holes for stars > 25 $M_\odot$) [62].

2.6.5 Neutrino Trapping

As collapse continues, electron neutrinos diffuse out of the core until the core reaches densities $\mathcal{O}(10^{12}$ g/cm$^3)$ at which point neutrinos are unable to escape, as their mean free path for neutral current ν_e scattering becomes less than the size of the core for several milliseconds. At this point,

all energy becomes trapped within a radius of only 30 km inside the core. The spherical outer shell separating the inner "opaque" core and the outer area which is transparent to neutrinos is called the *neutrinosphere*. Neutrinos inside the neutrinosphere are trapped while others outside are free to propagate outwards. A unique neutrinosphere exists for each flavour, dependent on the primary interactions that the neutrinos undergo.

2.6.6 Core Bounce and Shock Break-out

After neutrino trapping occurs, collapse continues and the core density continues to increase. Eventually, the core reaches the density of nuclear matter, $\rho = 2.7{\times}10^{14}$ g/cm^3, can no longer be compressed any further due to nucleon degeneracy pressure, and the core bounces (Figure 2.5: $t = 0$ ms). After a neutrino breakout (described further in Sec. 2.6.7), a shock wave is created inside the core and begins propagating outward and interacting with the outer layers of matter, which are still falling supersonically inward toward the core. The shock wave is a discontinuity in pressure, density, and temperature, and it compresses and heats the matter it passes through. The shock begins at a radius of $\sim$ 10 km inside the core and moves outward with a velocity of $\sim 7{\times}10^7$ m/s. During this process, the PNS continues to accumulate mass by accreting infalling matter that successfully passes through the shock front.

Material behind the shock front, mainly composed of free nucleons, electrons, and photons is heated by accretion on the PNS inducing further creation of positrons and electrons which capture on neutrons and protons to produce $\bar{\nu}_e$ and ν_e:

$$e^+ + n \rightarrow p + \bar{\nu}_e \tag{2.5}$$

$$e^- + p \rightarrow n + \nu_e \tag{2.6}$$

2.6.7 Neutrino Break-out

At roughly 1 ms after bounce, the shock hits the neutrino sphere, allowing newly-created neutrinos to escape in a high-energy burst by transfer of kinetic energy. The main ν_e breakout pulse just after the small downturn in $\mathcal{L}_{\nu_e}$ results from the dissociation of nuclei and subsequent electron capture on free protons. All flavours of neutrinos are actually created in the high-temperature wake directly

behind the shock wave through a wide variety of pair processes:

$$\text{Pair Annihilation: } \gamma + \gamma \rightleftharpoons e^+ + e^- \rightarrow \nu + \bar{\nu} \tag{2.7}$$

$$\text{Plasmon Decay: } \textit{plasma excitation} \rightarrow e^+ + e^- \rightarrow \nu + \bar{\nu} \tag{2.8}$$

$$\text{Photoannihilation: } \gamma + e^{\pm} \rightarrow e^{\pm} + \nu + \bar{\nu} \tag{2.9}$$

$$\text{Nucleon-Nucleon Bremsstrahlung: } (A,Z) + (A,Z) \rightarrow (A,Z)' + (A,Z)' + \nu + \bar{\nu} \tag{2.10}$$

$$\text{Beta-Nucleon Bremsstrahlung: } e^{\pm} + (A,Z) \rightarrow (A,Z)' + e^{\pm} + \nu + \bar{\nu} \tag{2.11}$$

The photoannihilation processes dominate at lower temperatures, while the main contributions at higher temperatures are due to pair annihilation. Additional ν_x are created from the annihilation of electron neutrino-antineutrino pairs:

$$\nu_e + \bar{\nu}_e \rightarrow \nu_{\mu,\tau} + \bar{\nu}_{\mu,\tau} \tag{2.12}$$

Newly-created neutrinos (ν_e, $\bar{\nu}_e$, and "ν_x") stream outward during what is known as the "neutrino break-out" (refer to $t \sim 0$ - 400 ms. in Fig. 2.5). This sudden release of neutrinos is a characteristic of the theory of collapse and supernovae, which if measured would speak volumes concerning the dynamics of a dense core otherwise obscured from view. It leaves a defined signature in the time spectrum in Figure 2.5. Since ν_e and $\bar{\nu}_e$ are created via electron and positron capture during several preliminary phases, their luminosities are larger than those of ν_x.

2.6.8 Explosion

The explosion of the star occurs when the radius of the shockwave reaches ∼400 km and some of the outer material of the star is ejected. A "prompt" explosion can occur in lower mass stars if the shock wave is able to propel the outer layers of the star. In low mass stars, once the shock has emerged from the small core, the temperature lowers, and electron capture processes no longer decrease the pressure.

If the star is massive, the shock wave will not have sufficient energy to move through the outer layers, essentially stalling in the process. Neutrinos are thought to revive the shock wave

by transfering some of their momentum, though the mechanism is not fully understood. A small portion of neutrinos streaming out of the core may be absorbed by nucleons behind the stalled shock wave and effectively transfer kinetic energy, resulting in a "delayed" explosion [67],[63],[51],[64]. Understanding the mechanism that revives the stalled shock into explosion has been the goal of the community for many decades. Since the pioneering work of Bethe and Wilson (1985) [68],[69], the favoured shock revival mechanism has been the delayed-neutrino mechanism, whereby the neutrinos transfer some or all of their kinetic energy to the outgoing shock wave, but some theories have also suggested that this neutrino-driven mechanism might be secondary to other mechanisms such as the acoustic or magnetorotational described in [70] and [71].

2.6.9 Cooling & Aftermath

In most supernovae cases, a neutron star remains behind and cools by emitting neutrinos over a timescale of a few seconds (Fig 2.5: $t \sim 800+$ ms). Neutrinos of all flavours are emitted as $\bar{\nu}\nu$ pairs via the pair processes listed in Equations 2.7-2.12, until the core temperature decreases to a point that cooling reactions with neutrino products are no longer possible. Most neutrinos emitted during this phase have an average energy between 12-20 MeV per particle. For massive stars above 25 $M_{\odot}$, the supernova remnants can be consumed by a newly-formed black hole which results in a defined end to the neutrino emission. For extremely-high progenitor masses (> 260 $M_{\odot}$), collapse can continue to a supermassive black hole ($> 10^5$ $M_{\odot}$) [63].

The end result of a supernova may also include intense stellar winds and various heavy-elements created during explosion. Various kinds of electromagnetic radiation can also have resulted from the interaction of the shock wave and the outer material which lead to supernova remnants with distinct optical signatures. An expanding shell of gas continues to radiate radio waves and x-rays for thousands of years leaving behind an expanding nebula known as a supernova remnant (SNR) and typically a neutron star which often appears in the form of a pulsar.

At later times, the supernova light curve is dominated by the decay of ^{56}Co as gamma rays from this decay escape as the ejecta expands and thins in the ISM.

2.7 Once in a Lifetime Measurement

The fundamental role of neutrinos in the core-collapse process was confirmed by the set of neutrino data from SN1987A [49]; however, a larger number of events is required to establish constraints on the supernova explosion mechanism and test predictions of current supernova models. While the general picture of core-collapse supernova theory may be well established, details of the explosion mechanism, its dependence on pre-collapse conditions and input physics, and its neutrino and possibly gravitational wave (GW) signals remain to be determined. A fundamental problem of stellar astrophysics involves the yet unknown details of the catastrophic core infall and subsequent reverse into a powerful ejection of the stellar mantle and envelope - the supernova explosion. It has been a matter of intense research since the crucial role of SNe in the synthesis of heavy elements and the dissemination of the nuclear burning products of stars was recognized by Burbidge *et al.* in 1957 [72]. Since EM radiation does not to convey information about the inner workings of the supernova core, neutrinos are the only known means to study this process. Neutrino breakout is a characteristic of the theory of supernova collapse and explosion, which if measured would speak volumes concerning the dynamics of the dense core otherwise obscured from view.

Detection of the next galactic supernova is likely to yield important information about the supernova collapse mechanism, explosion, and convey information about the properties of neutrinos. It could provide more information on the neutrino mass hierarchy and set lower limits on the neutrino lifetime. Detection of SN neutrinos could provide a more complete picture of stellar evolution, providing model constraints on the explosion mechanism along with protoneutron star and black hole formation. SN neutrino detection also provides early supernova alert as the neutrinos reach earth often hours earlier than the electromagnetic signal.

Chapter 3

Introduction to the SNO+ Experiment

The SNO+ experiment is the successor to the SNO experiment [73] and a kilo-tonne-scale, multipurpose liquid scintillator detector designed to observe the theoretical process of neutrinoless double-beta ($0\nu\beta\beta$) decay in the isotope ^{130}Te. It will also be able to detect low-energy solar neutrino fluxes, geo- and reactor antineutrinos, and possibly more exotic physics events such as invsible nucleon decay in water.

SNO+ can also serve as a supernova neutrino detector during all phases of the experiment and is preparing to participate in the inter–experimental Supernova Early Warning System (SNEWS), which has the goal of providing a fast and reliable alert using the coincident observation of burst signals in several operating detectors.

The primary physics goal of SNO+ is the investigation into the Majorana nature of neutrinos with a search for the neutrinoless double-beta ($0\nu\beta\beta$) decay of ^{130}Te. As mentioned in Chapter 1, $0\nu\beta\beta$ is a rare process which can only occur if neutrinos are Majorana fermions, that is, if they are their own antiparticles. The measured half life of $0\nu\beta\beta$-decay can be used to calculate the effective Majorana neutrino mass, $m_{\beta\beta}$. The expected value for the $0\nu\beta\beta$ half life of ^{130}Te is of the order of 10^{25} years for a neutrino mass range of about 200–400 meV. With an initial loading of 0.3% of natural tellurium and moving to 0.5%, the aim is to reach a sensitivity of 100 meV on the effective Majorana neutrino mass after several years of data gathering. The large Te-loading and

low background of SNO+ allows for the investigation of such a rare event.

3.1 Detector Design

SNO+ is currently under construction and is based on the original SNO infrastructure at SNOLAB, within the Creighton Mine near Sudbury, Ontario, Canada. The detector is located 2,070 m underground in an active mine giving it an overburden of 5890±94 meters water equivalent (m.w.e.) as seen in Figure 3.1. This overhead shielding reduces the cosmic ray muon flux to ∼70 muons/day (0.27 μ/m^2/day in the detector volume). The maintenance of the lab as a Class-2000 clean room further reduces low-energy backgrounds.

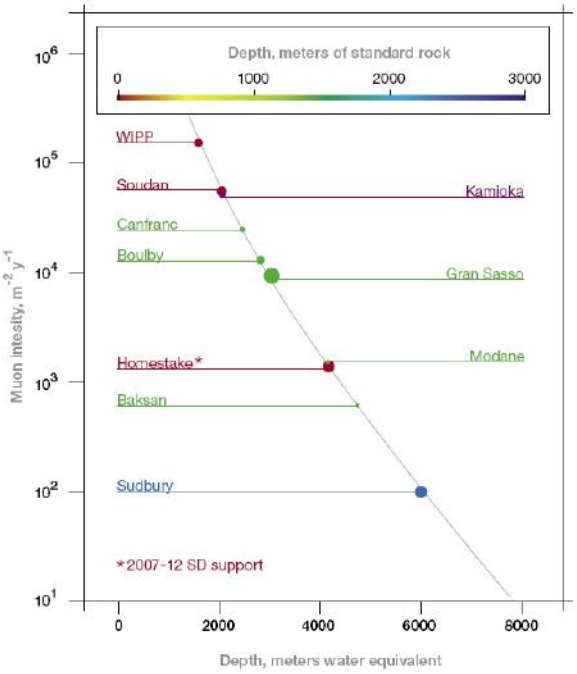

Figure 3.1: Major underground laboratories of the world. Each dot's size is proportional to the area available for science at each lab. The intensity of muons created by cosmic rays is shown as a function of the depth in feet of standard rock (density 2.65) and in meters water equivalent, m.w.e. (density 1.00). SNOLAB (located in *Sudbury*) is at roughly 6000 m.w.e. giving a muon intensity on the order of 100/m^2y [74].

The SNO+ experiment re-purposes most of the original hardware of the Sudbury Neutrino Observatory (SNO) detector which was used to solve the *solar neutrino problem*. The original SNO experiment was designed to detect neutrinos interacting with 1000 tonnes of heavy water inside a

12 m-diameter, spherical acrylic vessel. Its size allowed for an efficient radial fiducial cut reducing external surface backgrounds, while allowing for a significant isotropic mass. A schematic diagram of the SNO+ detector is shown in Figure 3.2.

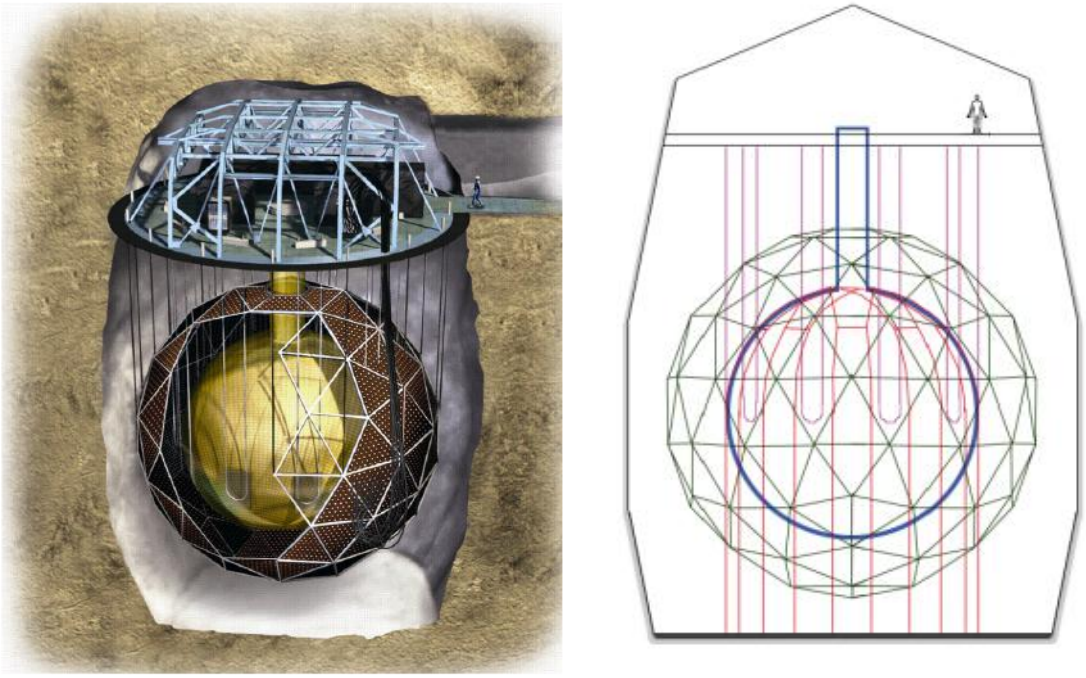

Figure 3.2: *Left*: Artist's rendition of the SNO detector (D. Foley, National Geographic, 2000). The 12-m diameter acrylic sphere is surrounded by a geodesic, stainless steel PMT support structure holding ∼9500 inward-looking PMTs. The entire infrastructure is located in a large cavity blasted out of the surrounding rock which contains light water for shielding from mine-rock backgrounds. A deck located above the experiment allows for access around the neck region for calibration and maintenance purposes. *Right*: Schematic of the SNO+ detector. SNO+ uses a tensylon rope net system (shown in red) to offset the buoyancy of the acylic vessel (AV) (blue) containing LAB while it rests in the light water filling the rock cavity. There are also a rope system (pink) which was the original rope hold-up system for the detector when it contained hard water in SNO. The geodesic PMT support structure (PSUP) (green) surrounds the AV and holds the roughly 9500 PMTs (not shown) [75].

Neutrinos interacting with the electrons and nuclei in heavy water produced charged particles which produced Cherenkov light inside the detector. This light was detected by surrounding photomultipler tubes pointed inwards, attached to a geodesic stainless steel support structure. Approximately 7000 tonnes of light water surrounding the acrylic vessel shielded the target from the surrounding rock.

Once the SNO experiment was successfully completed, the infrastructure was upgraded to a

detector for the SNO+ experiment in search of neutrinoless double beta decay in ^{130}Te, which, if observed, would indicate that neutrinos are Majorana particles. As the decay rate for neutrinoless double-beta decay is indirectly proportional to effective Majorana neutrino mass squared, the observation would also help determine the neutrino mass hierarchy. SNO+ is expected to be sensitive to a decay rate of 10^{26} years after five years running at 0.5% loading of ^{130}Te [17],[76]. Future phases should improve the sensitivity by increasing Te loading to 5%. Studies are ongoing to prepare for this phase.

SNO+ uses the original SNO spherical acrylic vessel of 6-m radius and 5.5-cm thickness, but fills it with 780 tonnes of linear alkyl benzene (LAB),or $C_{18}H_{30}$, surrounded by ∼7000 tonnes of ultra-pure, light water. Since LAB is lighter than water (H_20) with a density of ($\rho = 0.86$ g/cm^3), it will cause the acrylic vessel to be buoyant in the surrounding light water. For this reason, a hold-down rope-net system has been installed on the top part of the AV and anchored at the cavity floor. The original 18-m diameter stainless steel PMT support structure (PSUP) surrounds the 12-m diameter acrylic vessel in the form of a geodesic sphere holding over 9500 photomultiplier tubes (PMTs) pointed inwards to detect photons from particle interactions within the acrylic vessel. The stainless steel PMT support structure, photomultiplier tubes, their light concentrators and associated hardware are seen as the geodesic sphere surrounding the yellow acrylic vessel in Fig. 3.2. The front faces of the PMTs are at a mean distance of 8.35 m from the center of the detector and offer about 54% coverage of the acrylic volume. Light produced inside the scintillator volume by the interaction of particles will be detected by these inward-looking PMTs. In general, the SNO+ PMTs have the ability to detect single photons created within the liquid scintillator. Several outward-looking PMTs (OWLs) point away from the acrylic towards the surrounding light water for the purpose of detecting muons. A newly constructed scintillator plant external to the detector will be used to purify the LAB to achieve minimal backgrounds [77]. A number of additional significant upgrades have been made to the original SNO detector itself, including an improved cover-gas system (now sealed to prevent Radon gas ingress), a new interface port for deploying calibration sources, upgrades to the data acquisition electronics to keep up with higher light output scintillator events, an embedded fiber-optic calibration system, an updated source/calibration deployment and umbilical retrieval mechanism (URM).

3.2 Scintillation Technique

SNO+ uses a liquid scintillator target which is a combination of a solvent, a fluor[1], and additional wavelength shifters and is sensitive to all flavours of neutrinos. Scintillation is a chemical process of luminescence whereby light of a characteristic spectrum is emitted following the absorption of radiation. This radiation is usually of a higher energy than the emission. Scintillation occurs when the fluor is excited by a charged particle or high-energy photon, and a visible or ultraviolet photon is then emitted by fluorescence. Scintillation light is isotropic and generally has a very small (or no) energy threshold, implying a high light yield. This latter quality means SNO+ is able to detect particles down to very low energies. Scintillators are available in a range of materials: inorganic crystals (NaI is common), organic plastics (robust and easy to manipulate, but tend to lose light yield as they age), and organic liquids, where the scintillating material is dissolved in a bulk carrier such as mineral oil. The fluor in SNO+ consists of 2,5-diphenyloxazole (PPO) which is dissolved in a concentration of 2 g/L in the bulk carrier called linear alkyl benzene (LAB), an aromatic hydrocarbon, which is essentially a mineral oil. LAB was chosen for its optical transparency and long scattering length, and hence, good light travel efficiency; its compatibility with acrylic; linear response in energy; its long time stability; and its low handling and environmental volatility and high flash point. Additionally, SNO+ can be locally supplied by a Quebec manufacturing plant which can provide high purity levels which help to limit cosmogenic activation. The scintillator will be purified in the underground SNO+ scintillation purification plant, which will further reduce contaminants contributing to backgrounds from radioisotopes (U, Th, K, Ra) that could interfere with the low-energy data in the experiment [77]. In addition, the scintillator will also be loaded with the double-beta isotope Tellurium-130 (^{130}Te) which is further discussed in Section 3.4.

Approximately 780 tonnes of this ultra-pure liquid scintillator cocktail will be used in SNO+. Since the scintillator is enclosed in a large transparent acrylic vessel, any light originating from within can be viewed by surrounding photomultiplier tubes (PMTs). The isotropy of scintillation light means that particle direction is not able to be reconstructed as well as it would be from Čerenkov radiation in water. However, scintillation will allow for a higher gain in light output for low-energy interactions and increased sensitivity to the anti-neutrino spectra.

[1] Fluor is used to refer to the scintillating compounds added to the solvent (linear alkyl benzene).

3.3 Photomultiplier Tube Response

3.3.1 Introduction to PMT Design and Operation

The photomultiplier tubes used in SNO+ are the same as SNO (Hamamatsu R1408 PMTs) and detect the light produced by the target material in the acrylic vessel (either scintillator or water). Among many desirable features, the most important PMT parameters for SNO+ are the noise rate, the efficiency, the transit-time spread and the amount of K, U and Th[2] in each PMT. The energy resolution and the event vertex spatial resolution are largely determined by the first three parameters and the detector energy threshold is also strongly affected by the radioactivities in the carbon-14 decay background from the linear alkyl benzene. The R1408 PMTs provide a high photon detection efficiency and fast anode pulse rise time and fall time < 1.7 ns and low amounts of radioactive materials [73].

On the order of 9500 inward facing PMTs collect photons produced in the scintillator and provide a photocathode coverage of roughly 31% of 4π steradians. To improve the light collection efficiency, a 27 cm-diameter light concentrator, as seen in Figure 3.3, is mounted on each PMT, increasing the effective photocathode coverage to about 59%. In the right pane of Fig. 3.3, the general structure of the PMT consists of a glass vacuum tube, a photocathode (not shown), several dynodes (not shown) which multiply the photoelectrons, an anode to collect the signal (not shown), and accompanying circuitry (not shown) to set the dynode potentials.

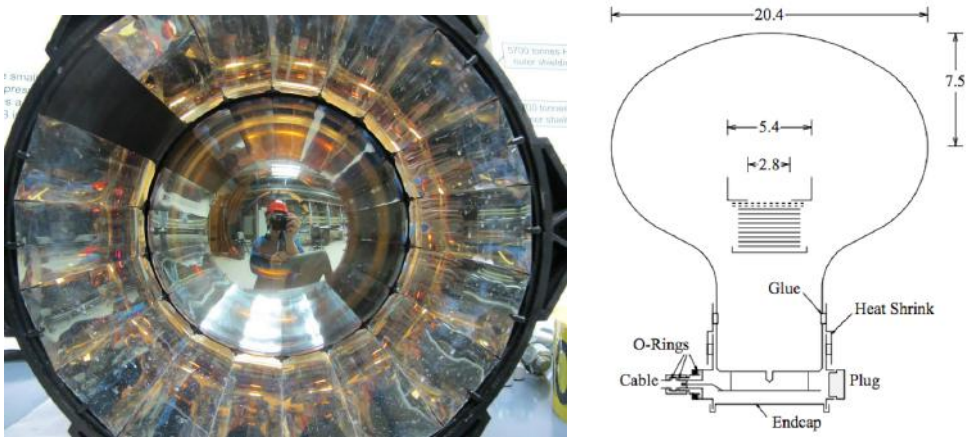

Figure 3.3: **Left**: A SNO+ photomultiplier tube surrounded by a concentrator. **Right**: Schematic of the SNO+ PMT [73].

[2]K, U, and Th are elements originating from mine dust and are backgrounds which need to be reduced in the experiment (more on backgrounds in Section 4.1.6)

After striking the photocathode, the photoelectron is focused onto the first dynode by an electrode. The dynodes are held at increasingly high voltages which accelerate electrons from dynode to dynode. Secondary emission results in multiple electrons, which is related directly to the dynode voltage difference, leaving the dynode surface per incident electron. This "gain" on the PMT results from the geometry of the dynode chain and is such that a cascade occurs with an exponentially-increasing number of electrons being produced at each stage. For example, if at each stage an average of 5 new electrons are produced for each incoming electron, and if there are 12 dynode stages, then at the last stage one expects for each primary electron about $5^{12} \sim 10^8$ electrons.

The PMT anode is at positive high voltage, typically in the range 1700-2100 V, and the photocathode is at ground voltage, such that the amplified signal is collected at the anode and passed out to the measurement circuits. The obtained negative electrical signal is proportional to the number of photoelectrons, N_{pe}. A single RG59/U type cable is used to carry the high voltage and the fast negative anode pulse which is then capacitively coupled to the front-end electronics.

3.4 Experimental Phases

SNO+ will operate in several experimental phases:

1. Internal H_2O, Water Phase ($\sim$ 3 months)
2. LAB+PPO, Pure Scintillator Phase ($\sim$ 2 months)
3. **0.3% (or 0.5%) Te-loaded Scintillator (*Phase* I), $0\nu\beta\beta$-Decay Phase**
4. Solar neutrino phase
5. 3% (or 5%) Te-loaded Scintillator (*Phase* II), Higher-loading $0\nu\beta\beta$-Decay Phase

Critical backgrounds such as the activities of the scintillator, AV, water shield, and PMT array can be thoroughly measured during the preliminary unloaded phases of the experiment (discussed further in the next section). The preliminary phases will be used to verify the optical model and detector response. SNO+ also aims to measure reactor antineutrino oscillations, low-energy solar neutrinos, and geo- antineutrinos during these stages. Neutrinoless double beta decay will be

searched for during Te-loaded phases. Throughout all stages of the experiment, SNO+ is sensitive to SN neutrinos of all flavours. Antineutrino measurements can also be made in all phases.

During water phase, the acrylic vessel will be filled with roughly 1 kilotonne of ultra-pure water. Over several months, the main physics goals will be a search for exotic physics, such as invisible nucleon decay of ^{16}O, the watch for supernova neutrinos, and the measurement of reactor and geo-antineutrinos. This phase is currently ongoing with the detector partially filled.

In the pure scintillator phase, the detector will be filled with about 780 tonnes of LAB-PPO liquid scintillator. The detector will be sensitive to low energy solar neutrinos during this phase, along with supernova, reactor, and geo-neutrinos.

The Te-loaded or $0\nu\beta\beta$-decay phase of the experiment is expected to start in 2017 and remain active for 5 years. For this phase, SNO+ will load about 2.3 tonnes of natural tellurium (0.5% loading by weight) into the liquid scintillator for the $0\nu\beta\beta$-decay search of ^{130}Te. Simultaneously, reactor neutrinos can still be observed, and the detector will be live to a potential, close-by supernova. Monte Carlo studies have demonstrated that the timing of scintillation light means that many remaining backgrounds (such as internal ^{214}Bi) can be significantly reduced through $\beta-\alpha$ coincidence cuts. The liquid nature of the scintillator cocktail allows purification and re-loading after each physics run, and the purification technique has been shown to reduce cosmogenics by factors of 100-1000 per pass [78]. In addition, cooling Telluric acid underground can reduce cosmogenically-activated backgrounds further.

To better match the quantum efficiency of the PMTs, additional wavelength shifters can be added to the scintillator cocktail along with 2,5-diphenyloxazole (PPO) which will act as the primary fluor. This will be done to shift the emission spectrum beyond the absorption tail and increase light yields.

Currently, two wavelength shifters, perylene and bisMSB, are being investigated. Perylene shifts the emission peak to ∼480 nm with a predicted light yield in SNO+ of about 300 Nhits (detected photoelectron hits) per MeV of energy, and bisMSB shifts the emission peak to ∼430 nm with a light yield of 200 Nhits/MeV[3] [75]. These wavelength shifters are discussed in further detail in Section 4.4.2 (See Figure 4.8). Both perylene and bisMSB shift the light to even longer wavelengths,

[3]The scintillator cocktail light yield values have since been updated as the studies for the scintillator cocktail are still ongoing, with the goal of achieving the highest light output.

getting well above the absorption of the scintillator, thus the final choice will depend on the timing optical properties, the light yield and the scattering length of the full scintillator mixture. Based on bulk optical properties measurements of the detector, a prediction of a detected light yield has been estimated to be 400 photoelectrons/MeV averaged over the detector volume [78].

3.5 Backgrounds & $0\nu\beta\beta$ Sensitivity

In all phases of the experiment, it is important to control and reduce the sources of energetic background. This is especially important for the neutrinoless double beta decay and solar neutrino searches due to inherently-low energetic signatures. Both internal and external sources of backgrounds exist for SNO+, and the levels are assumed to be equal to those initially achieved by Borexino [79],[80]. Internal backgrounds include all the non-signal interactions that occur inside the AV inside a fiducial radius <6 m. External backgrounds are interactions occurring outside the scintillator target that can induce events within it. External backgrounds include decay products of Radon gas and mine dust, which means the detector must be sealed from mine air and cleaned thoroughly with ultrapure water (UPW) to remove any mine debris. The SNO+ inner AV was cleaned by hand to remove a layer of dust that had accumulated since SNO. The level of cleanliness was measured before and after cleaning with a tapelifting procedure. Small samples of tape were placed on the AV and used to lift debris from it; these were then analyzed using x-ray fluorescence methods to determine the concentration of mine dust and radioactivity from uranium and thorium decay chains. The author was involved in the creation of tapelifts, AV cleaning, and XRF analysis of tapelifts during the AV cleaning period of SNO+, and the results of this study are found in Appendix A of this thesis.

The energies of these backgrounds around the sensitive Q-value region for neutrinoless double beta decay of ^{130}Te is shown in Figure 3.7. For the $0\nu\beta\beta$ search, an asymmetric region of interest (ROI) is defined, which extends from 0.5σ to 1.5σ around the Gaussian signal peak. For the 0.3% Te-loaded cocktail with a light yield of 200 Nhits/MeV, the energy resolution at 2.5 MeV is $\sim$270 keV (FWHM), while the averaged position resolution at the same energy is $\sim$15 cm at the detector's center. An asymmetric ROI retains most of the $0\nu\beta\beta$ decays but considerably reduces the backgrounds from $2\nu\beta\beta$ and low energy ^{238}U- and ^{232}Th-chain decays. Most external backgrounds

are rejected by a 3.5 m fiducial radius cut, which preserves 20% of signal events.

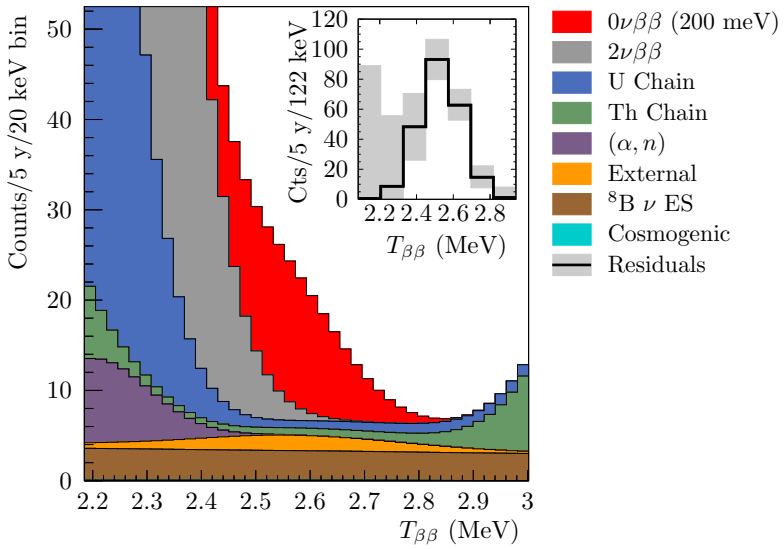

Figure 3.4: Energy spectra of $0\nu\beta\beta$ signal plus backgrounds near the $0\nu\beta\beta$ region of interest [75].

Inside the 3.5 m fiducial volume (FV) and 2.47 MeV to 2.70 MeV energy ROI, the main background sources are:

- **$2\nu\beta\beta$**: The $2\nu\beta\beta$ spectrum is an irreducible background due to the $2\nu\beta\beta$ decays of ^{130}Te. A high-energy tail of these events appear in the ROI due to the energy resolution of SNO+.

- **Internal ^{238}U- and ^{232}Th-chain Backgrounds**: The dominant backgrounds in the signal ROI are due to ^{214}Bi-Po and ^{212}Bi-Po decays stemming from the ^{238}U- and ^{232}Th-chain (see Appendix A for more explanation). In Monte Carlo simulations, SNO+ has currently achieved ~100% rejection of separately triggered ^{214}Bi-Po and ^{212}Bi-Po decays falling inside the ROI and FV using $\beta-\alpha$ delayed coincidence (see [75] for more details on this decay process). Cuts based on PMT hit timing achieve a rejection factor of ~50 for ^{212}Bi-Po and ^{214}Bi-Po pile-up events that fall in the ROI and FV. Other minor contributions in the ROI are due to ^{234m}Pa (^{238}U chain), ^{210}Tl (^{238}U chain) and ^{208}Tl (^{232}Th chain).

- **(α,n) Backgrounds**: Neutrons can be produced in the liquid scintillator by (α,n) reactions on ^{13}C or ^{18}O atoms, muon interactions in the scintillator volume, ^{238}U fission, and (γ,n) reactions for $E_\gamma > 3$ MeV. These neutrons will scatter from protons during the thermalization

process, resulting in recoils emitting scintillation light. The visible proton energy together with the energy lost by the alphas before interaction is the prompt signal. If the isotope is in an excited state, the emitted de-excitation gammas are also part of the prompt signal. Both the prompt signal and the delayed 2.22 MeV-γ, from neutron capture on a proton, produced by (α,n) reactions can leak into the $0\nu\beta\beta$ ROI. Coincidence-based cuts have been developed that remove more than 99.6% of the prompt and ∼90% of delayed events.

- **External Backgrounds**: ^{208}Tl and ^{214}Bi nuclides contained in the AV, hold-down rope system, water shielding, and PMT glass are the major contributors; however, the fiducial volume of 80% (radius of 3.5 m) reduces these events by several orders of magnitude.

- **^{8}B ν ES**: The ^{8}B solar neutrino flux is a flat continuum background from the elastically scattered (ES) electrons normalized using the total flux and published solar mixing parameters [73]. Although a background to $0\nu\beta\beta$ detection in the ROI with 0.3% Te-loading, the solar neutrino background is also another signal SNO+ can measure with excellent sensitivity to CNO, pep, and low-energy ^{8}B solar neutrinos. The first measurement of the flux of neutrinos from the subdominant CNO fusion cycle would constrain the metallicity of the solar interior. This would provide critical input to the so-called *solar metallicity problem* - the current disagreement between helioseismological observations of the speed of sound and model predictions, due to uncertainties in the heavy element (metal) content of the Sun.

- **Cosmogenic Backgrounds**: Besides the natural radioactivity present in the scintillator, LAB can be activated by cosmic ray neutrons and protons while it is above ground. Cosmic-ray particles are capable of forming multiple radionuclides within germanium and copper, the most relevant isotopes being ^{60}Co, ^{110m}Ag, ^{88}Y, and ^{22}Na, which decay in the energy region of interest for neutrinoless double-beta decay. These cosmogenically-induced backgrounds will be reduced to less than one event per year with the developed purification techniques for the scintillator [77] along with a long period of underground storage.

- **Pile-up Backgrounds**: Pile-up events, caused by two or more decays in the same trigger window, become important when the event rate of one or all of the contributing decays is very high (hundreds of Hz), like ^{14}C decays or ^{210}Bi or ^{210}Po. ^{14}C ($T_{1/2}$ = 5700 yr, Q-value

= 0.16 MeV) is naturally present in the liquid scintillator. It is a direct background for the very low-energy *pp* solar neutrino measurements. In SNO+, we expect a kHz decay rate for ^{14}C which can produce a background energy level on the order of 150-200 keV. The most important pile-up backgrounds for the $0\nu\beta\beta$ search are due to high-rate ^{210}Po+$2\nu\beta\beta$ and ^{210}Bi+$2\nu\beta\beta$, with bismuth and polonium coming from both the Te-loaded scintillator and the acrylic vessel surface. A rejection technique, using the distortion of the timing, is used to efficiently reduce all of these backgrounds to a negligible level [81],[82].

Table 3.1 lists the expected background counts in the signal ROI and fiducial volume (3.5 m) in SNO+ for the first year (Year 1) and in 5 years of the 0.3% Te loading phase[4]. A light yield of 200 Nhits/MeV has been assumed in these values, though the value has been found to be on the order of 400 Nhits/MeV more recently, and several other cuts have been applied as decribed in [75].

Background	**1 Year**	**5 Years**
$2\nu\beta\beta$	6.3	31.6
^{8}B ν ES	7.3	36.3
Uranium Chain	2.1	10.4
Thorium Chain	1.7	8.7
External	3.6	18.1
(α, n)	0.1	0.8
Cosmogenics	0.7	0.8
Total	**21.8**	**106.8**

Table 3.1: Expected backgrounds counts in the region of interest and 3.5 m FV for $0\nu\beta\beta$ in SNO+ for the one and five years of running with 0.3% Te-loaded scintillator [75]. These values are the most recently-published, but since studies are ongoing for 0.5% Te-loading, these will be updated.

Most sources of backgrounds in SNO+ are negligible for an MeV supernova signal, though there are a few natural backgrounds of this magnitude, some induced by instrumental effects. The only sources of background known to give rise to multiple synchronous physics events in the detector are high energy cosmic ray muons. The muon flux at SNOLAB depth is roughly 3 per hour (∼70 per day). This muon flux can give rise to multiple spallation products which are detected as a burst of events. A high energy muon may penetrate the overburden of rock, and arrive in the detector

[4]SNO+ has recently received more funding to upgrade to 0.5% Te loading, and background studies are ongoing. The recently published values ([75]) are described in this section.

volume with a considerable amount of energy, lighting up the detector. Muon-induced backgrounds are generally very short-lived however, on the order of milliseconds to seconds half-life, and can be rejected by veto-ing the detector for a few minutes after each muon event. Muon events are often accompanied by a prompt burst of neutrons

The expected energy spectrum for a 0.3% Te-loading, 2 years of running with a radial fiducial volume cut of 3.5 m is shown in Figure 3.8. The expected neutrinoless double beta decay signal, assuming an effective Majorana neutrino mass of 200 meV is shown with the dominating $2\nu\beta\beta$ background in red. SNO+ is expected to reach a sensitivity to $0\nu\beta\beta$-decay at a level lower than 100 meV.

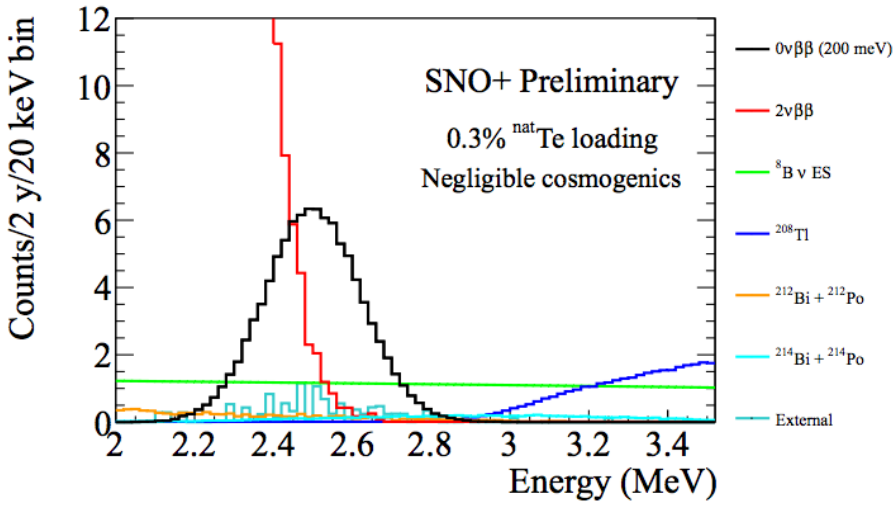

Figure 3.5: Expected energy spectrum (average profiles) for the SNO+ $0\nu\beta\beta$-decay search [83]. The spectrum is obtained for 2 years of running, a fiducial volume (FV) cut of 80% and 0.3% Te-loading (800 kg of ^{130}Te). External backgrounds are reduced by the FV cut and by a likelihood ratio. Negliglible cosmogenic induced background is assumed. The expected $0\nu\beta\beta$-decay signal, assuming an effective Majorana neutrino mass of 200 MeV, is also shown for comparison [84],[85]. Plot from [81].

In five years of running LAB loaded with 0.3% by mass of natural Te (corresponding to nearly 800 kg of ^{130}Te), SNO+ will be able to set a limit on the lifetime for neutrinoless double beta decay of $T_{1/2} \geq 9\times10^{25}$ years. A loading of 3% would provide a lifetime limit of $T_{1/2} \geq 7\times10^{26}$ y in 5 years, corresponding to a limit on $m_{\beta\beta} \leq 25$ meV. With a 0.3% loading, SNO+ anticipates being able to set a 90% CL lifetime limit of $T_{1/2} \geq 9\times10^{25}$ y in 5 years of running, corresponding to a limit $m_{\beta\beta} \leq 67$ meV ([85] [84]), just above the inverted mass hierarchy.

3.6 SNO+ Supernova Neutrino Detection

Generally, the gravitational binding energy carried away by neutrinos can be estimated for a star using:

$$E_b \simeq \frac{GM_{core}^2}{R_{core}} \simeq 3 \times 10^{53} erg \tag{3.1}$$

where $M_{core} \sim 1.4$ $M_\odot$ is the mass of the collapsing core and mass of the resulting neutron star and $R_{core} \simeq 10$ km is the radius of the proto-neutron star. Approximately 1% of E_b is from the electron neutrinos created in the initial neutronization burst, whereas the majority of the energy is attributed to the neutrinos created subsequently during accretion on the proto-star and in the high-temperature wake behind the shock wave and the cooling of the PNS. It's estimated that 50% of the entire neutrino signal is ejected within the first 1-2 seconds of collapse [86],[87].

The shape of the individual SN ν energy spectra is expected to approximate a thermal spectrum in the absence of neutrino flavour changing mechanisms [88]. Models agree on the following hierarchy for the average neutrino energies:

$$\langle \mathrm{E}_{\nu_\mathrm{e}} \rangle < \langle \mathrm{E}_{\bar{\nu}_\mathrm{e}} \rangle < \langle \mathrm{E}_{\nu} \rangle \tag{3.2}$$

The hierarchy in particle temperatures is due to the different flavour-dependent processes by which neutrinos are trapped within the core. The neutrinosphere of the electron neutrinos will have a greater radius than the radii of the neutrinospheres of the other neutrinos. Consequently, the electron neutrinos will be confined to the greatest volume in regions that are more distant from the core. Here the temperature is lowest, thus electron neutrinos will have the lowest energy of all the flavours. Muon and tau neutrinos are confined to the deeper and hotter regions of the core, giving them the greatest average energy.

SNO+ has a low trigger threshold and is sensitive to both charged current (CC) interactions and neutral current (NC) interactions. Neutrino proton elastic scattering (ES) is the main channel, and provides spectral information about all flavours with a relatively high cross section. The possible SN neutrino interaction channels during the SNO+ pure scintillator phase are listed in Table 3.2 together with the expected event rates. SNO+ is expecting ∼383 events in total from a SN 10 kpc

away, mainly through proton elastic scattering and inverse beta decay by electron anti-neutrinos. This is considering losses due to trigger thresholds (∼200 keV) to avoid low-background noise.

Supernova electron neutrinos, ν_e, and antineutrinos, $\bar{\nu_e}$, can weakly couple with neutrons in the scintillator hydrocarbon through the following charged current (CC) processes: $\nu_e + n \rightarrow p + e^-$ and $\bar{\nu}_e + p \rightarrow n + e^+$ (Inverse Beta Decay). Muon and tau type neutrinos have fewer interaction channels available to them since they do not possess energy sufficient to interact via the CC channel. The CC reaction has a large cross section in SNO+.

Additionally, SNO+ can measure the flux of ν_x and ν_e. As the mean neutrino energy is below about 30 MeV, ν_e and $\bar{\nu}_e$'s will be detected mainly by the charged current (CC) interactions, while supernova ν_x's can only be detected by the more challenging neutral current (NC) reactions. One NC reaction is neutrino–proton elastic scattering (ES), $\nu_x + p \rightarrow \nu_x + p$, which is the only channel that provides spectral information about the ν_x's [89]. The total cross section of this process is about a factor of three smaller than the cross section of inverse beta decay, however, the reaction is possible for all six neutrino types yielding a similar number of events for a detector threshold above $\sim$ 0.2 MeV.

Reaction	**No. of Events**
NC: $\nu + p \rightarrow \nu + p$	429.1±12.0[a]
CC: $\bar{\nu}_e + p \rightarrow n + e^+$	194.7±1.0
CC: $\bar{\nu}_e$ + ^{12}C $\rightarrow$ ^{12}B$_{g.s.}$ + e$^+$	7.0±0.7
CC: ν_e + ^{12}C $\rightarrow$ ^{12}N$_{g.s.}$ + e$^-$	2.7±0.3
NC: ν + ^{12}C $\rightarrow$ ^{12}C* (15.1 MeV) + $\nu^{'}$	43.8±8.7
CC/NC: ν + ^{12}C $\rightarrow$ ^{11}C or ^{11}B + X	2.4±0.5
ν-electron elastic scattering	13.1

Table 3.2: Supernova neutrino interaction channels in LAB-PPO. The integrated number of events for the entire SN burst, per 780 tonnes of target material, assume the incoming neutrino time-integrated flux described in [90]. No flavour changing mechanisms are considered. The uncertainties on the event rates only include the cross section uncertainties. [a]118.9±3.4 above a trigger threshold of 0.2 MeV visible energy. This allows for approximately 383 total events from all reactions above a trigger threshold of 0.2 MeV. ν indicates all other neutrino flavours not including ν_e and $\bar{\nu_e}$. Table from [75].

Monte Carlo simulations [90] have been completed for SNO+ to determine the expected energy signal for the elastic scattering reaction. The simulation assumes that the distance from the SN

to Earth is d = 10 kpc and that 3×10^{53} erg of binding energy (E_b) is released in the form of neutrinos, equally partitioned amongst all six flavours and types. SN have mean ν_e, $\bar{\nu}_e$ and ν_x energies of 12 MeV, 15 MeV and 18 MeV, which are consistent with the findings from SN1987A [91].

Figure 3.9 shows the reconstructed energy spectrum from these simulations of all neutrinos emitted in the first second of the SN and detected in SNO+ via the ν–p ES reaction. This is shown together with the true neutrino spectrum emerging from the SN. The resulting best fit $\langle E_\nu \rangle$ spectrum is also shown and is in excellent agreement [90]. The corresponding best fit values are $\langle E_\nu \rangle = 17.8^{+3.5}_{-3.0}(\text{stat.})^{+0.2}_{-0.8}(\text{syst.})$ MeV and $\epsilon_{\nu_x} = 102.5^{+82.3}_{-42.2}(\text{stat.})^{+16.2}_{-13.0}(\text{syst.}) \times 10^{51}$ erg [92], while the respective expectation values are 18 MeV and 100×10^{51} erg.

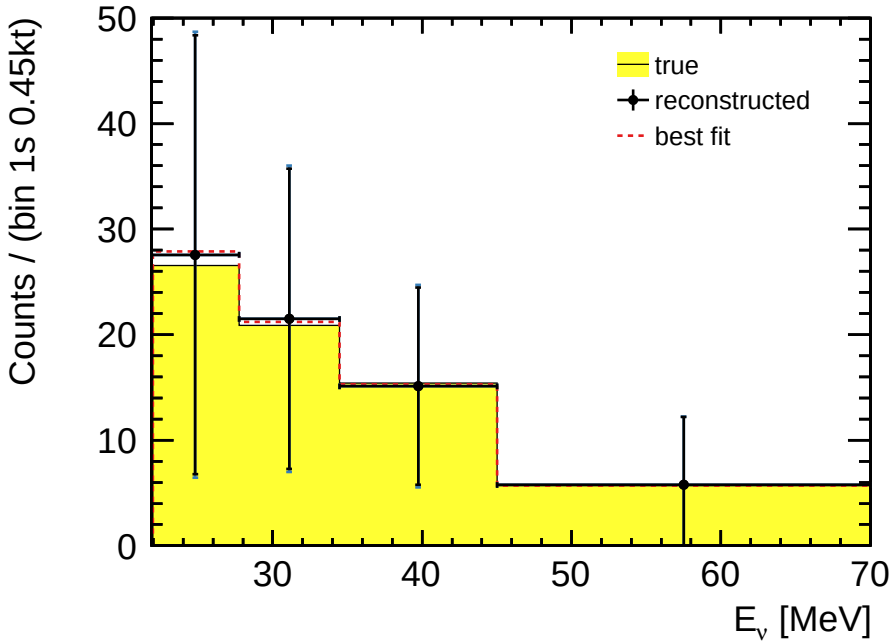

Figure 3.6: True, reconstructed and best fit SN neutrino energy distribution of the ν_p elastic scattering (ES) detection channel within the fiducial volume (FV) and above the detector threshold [93]. The shown spectra are the sum of the ν_e, $\bar{\nu}_e$, and ν spectra, considering their fluence in the first second of the reference SN. The uncertainties shown in black are statistical uncertainties. The uncertainties shown in blue are the total uncertainties including the systematic uncertainty added in quadrature. The contribution from systematics is too small to be well–resolved [90].

3.7 Electronics and Data Acquisition System

3.7.1 Overview

As seen in the example above, during a supernova event in which the SNO+ detector could expect up to 383 events within 1-2 seconds (190 in the first 2 seconds) for a 10 kpc supernova (a closer SN would increase the flux), the data acquisition system must be able to intake, process and save the data.

Event triggering and measurement of PMT pulses are performed by the electronics system. The time and integrated charge of PMT pulses, along with the event trigger information, are read out by the data acquisition system, or DAQ, and built into an event record. This event record is a brief snapshot of the overall signal, and forms the basic unit of signal measurement. Events are recorded to digital archive for later analysis, and dispatched over ethernet for data monitoring in realtime. The event data can be monitored without interfering with the archive data by accessing this dispatched datastream.

Although the SNO+ datastream is actually a continuous flow of data, it is logically divided into runs for ease of analysis. Each run indicates a period of static detector configuration which is controlled by ORCA[5], the SNO+ electronics graphical control interface. Detector configuration information is incorporated into the datastream in the form of a Run Record and a Trig Record.

SNO+ mostly uses electronics inherited from the SNO detector but also newly created additions and upgrades, specifically to address the challenges presented by the addition of scintillation light. A very basic overview of the electronics and DAQ is shown in Figure 3.10.

[5]ORCA (Object-oriented Requirements Capture and Analysis) is a modern electronic structure program that is used in the user interface software for SNO+, which was developed by collaborators at Washington University.

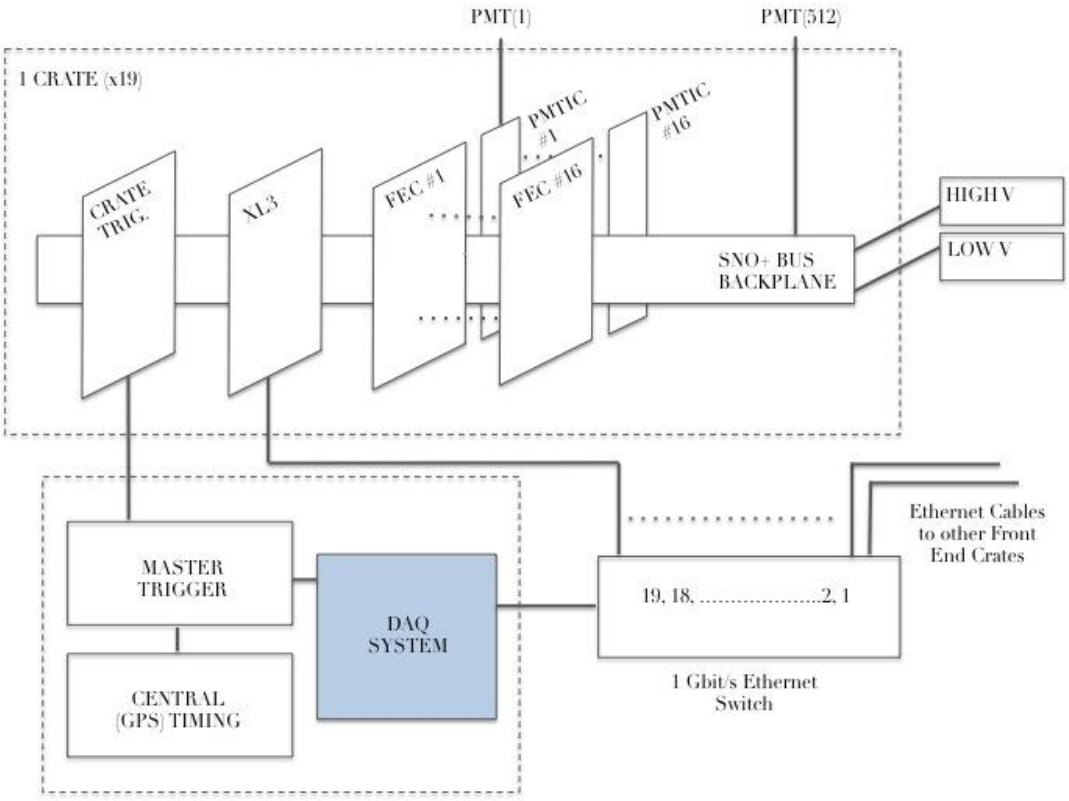

Figure 3.7: Basic overview of the SNO+ electronics and data acquisition system. The DAQ is designed to read out the PMT data stored in the electronics and assemble the individual PMT NHits into events. Diagram has been modified from [73].

The electronics act as the interface to the PMT array. The signals from the roughly 9500 PMTs are individually processed, including their charge integration and discrimination, analogue-to-digital conversion, time-to-digital conversion, analogue and digital buffering and multiplexing I/O tasks. The approximately 9700 data acquisition channels (one for each PMT) in the detector are divided among 19 crates of electronics, allowing the electronics to have the ability to buffer data at MHz event burst rates. The majority of these channels are from the inward-looking PMTs mounted on the PSUP, while a few are outward-looking (OWL) tubes mounted on the PSUP, which veto muon interactions which would begin in the surrounding cavity light water. In addition, there are four channels that act as a veto for light coming from the AV neck or chimney.

Each crate contains 16 Front-End Cards (FECs) and each FEC hosts 32 PMT channels. Every time a channel crosses a set threshold, various pulses: 100ns, 20ns, and ESUM are injected. The crate trigger card (CTC) adds up these sums for the crate and sends them to the Master Trigger

Card-Analogue (MTC/A+) which sums all crates and then triggers if above a certain threshold. The Master Trigger Card-Digital (MTC/D) looks at the MTC/A+ triggers and triggers if the trigger is masked-in. The trigger is discussed further in the Section 3.7.2. A 12-bit, 8-channel, 250 MHz digitizer for trigger waveforms replaces the scope from SNO and is controlled and read out through the ORCA user interface. The raw data recorded for each event consists of trigger time, channel number, and unique event number and all pulses.

The entire system of readout electronics contains gigabytes of memory. The average supernova event contains 1000s of PMT hits (NHit) leading to memory requirements on this level. The Front-End Cards (FECs) should be able to buffer approximately 11,000 supernova events. In SNO, the data was read out at ∼2 Mb/s and normal data rates were only ∼16 kbit/s. New boards allow for parallel asynchronous data readout. The crates are now limited to ∼13 Mbit/s each giving the experiment a 250 Mbit/s upper limit.

3.7.2 Trigger System

The trigger system determines if there is a large enough coincidence in the firing of the PMTs to signify a physics event. The trigger system collects all the signals, forming an analogue sum of certain characteristics, such as how many channels fired (NHit) and the total signal energy (ESUM). A global trigger is formed at the MTC; if the analogue sum is above a programmable threshold, a global trigger causes the data stored on the FECs to be collected by the data acquisition system and built into an event. Pile-up[6] is something that will most likely occur during a supernova event. This is something that needs to be characterized by supernova calibration of the detector.

3.7.3 Supernova Monitoring System

The DAQ contains a supernova monitoring system which works in concert with components of the SNO+ datastream to detect and evaluate spikes in the signal rate and provide the appropriate level of notification to the detector operator and the SNO+ supernova experts. It will eventually provide

[6] A pile-up event occurs when two or more decays (signal or background or a mixture) happen in the same trigger window and thus are potentially detected as a single event with energy equal to the sum of the individual energies. Pile-up events become important when the event rate of one or all of the contributing decays is very high (hundreds of Hz), as is the case with ^{14}C, ^{210}Bi or ^{210}Po decays. A rejection technique, using the distortion of the timing, is used to efficiently reduce these backgrounds. In water, from ^{14}C, SNO+ sees a reasonable fraction of NHit in the trigger window of 500 ns.

information to the international supernova watch community once SNO+ becomes a member of SNEWS.

The monitoring system consists of three levels. The Level 1 system monitors event data through the dispatched datastream, defines a burst criteria, and writes bursts of events to burst files. The Level 2 system analyzes the burst files, and identifies significant bursts based on the fraction of events passing a set of data cleaning cuts. Notification and summary of the Level 2 analysis are then provided to detector operators and a group of supernova experts by phone, email, and audiovisual alerts for those in the control room. The Level 3 system performs event reconstruction on the surviving events of significant bursts. A summary of the Level 3 analysis, including several plots of event distributions, is presented to the supernova experts who perform the final evaluation of the burst source. If it is concluded that supernova neutrinos are a possible source of the burst, the astronomical community would be notified through SNEWS (once SNO+ goes online). The SNEWS notification requires a coincidence with one other supernova-capable detector at a graphically-different location to alert the astronomical community.

3.8 Supernova Calibration

3.8.1 Directives

During a supernova event, the directives of SNO+ involve recording the data and quickly analyzing and interpreting the data. SNO+ will also aim to alert the worldwide supernova group using SNEWS capabilities once fully online. For these objectives to be realized, a calibration source must be used to stress test the data acquisition system prior to a supernova event's occurrence in the Milky Way galaxy, to ensure the system does not fail in the event of a supernova neutrino burst in the detector.

The SN neutrino detection efficacy is dependent on high livetime and robust data acquisition. The dataflow must be capable of handling supernova bursts that could happen at any point during running the experiment[7]. A high-energy neutrino source is ideal for calibration, but not feasible based on current technology. A photon source with similar SN neutrino pulse timing and intensity

[7]Recall that supernova are expected to take place in the Milky Way galaxy on the order of 3 times per century, and the last one occurred in 1987 (SN1987A).

can simulate a "neutrino" burst in the SNO+ scintillator and characterize the pile-up and burst capacity of the DAQ.

3.8.2 Overview of SNO+ Calibration

The calibration of SNO+ involves several redundant techniques using optical photons, gamma rays, alpha, beta, and neutron sources to fully characterize the detector. Calibration of the SNO+ detector is an integral part of the data acquisition process and analysis, and any data set ideally starts and ends with calibration runs. Calibration is typically divided into low-level calibration of detector electronics and PMTs and the detector optical, energy and physics response.

Low-level electronics and PMT calibration must be frequently updated and monitored due to the possibility of drifting PMT gains and changes in the detector condition.

To calibrate energy and optics response, the SNO+ detector will use both radioactive sources (beta, gamma, alpha, and neutron) and optical sources (LEDs and lasers coupled to optical fibers).

Radioactive sources are used to check energy scale, energy resolution, linearity of response, and detector asymmetries. They will also be used to determine the systematic uncertainties and the efficiency of all reconstructed quantities (i.e. energy, position, and direction). A list of radioactive sources that are being used are shown in SNO+ can be found in [75] and cover an energy range from 0.1 MeV to 6 MeV. In addition, the internal radioactivity can be used to calibrate the detector and check any energy shift or variation of the response over time.

Optical sources are used to verify the PMT response and to measure *in situ* the optical properties of the detector media. The optical calibration hardware consists of external systems consisting of sets of optical fibers attached to the PSUP in fixed positions, which are able to pulse light from fast LEDs or lasers into the detector. These external sources include TELLIE, SMELLIE, and AMELLIE which have been developed for calibrations of the PMTs response, time, and gain, and measuring the scattering and attenuation length of the scintillator without the need for source insertion through the SNO+ neck. An isotropic "laserball" device will be part of the optical calibration system and is discussed further in Section 3.8.4.

3.8.3 Source Deployment

Several calibration sources will be periodically deployed into the SNO+ detector using a source manipulator system and umbilical retrieval mechanism (URM). Deployment and retrieval is accomplished with the URM which is shown in Figure 3.8.

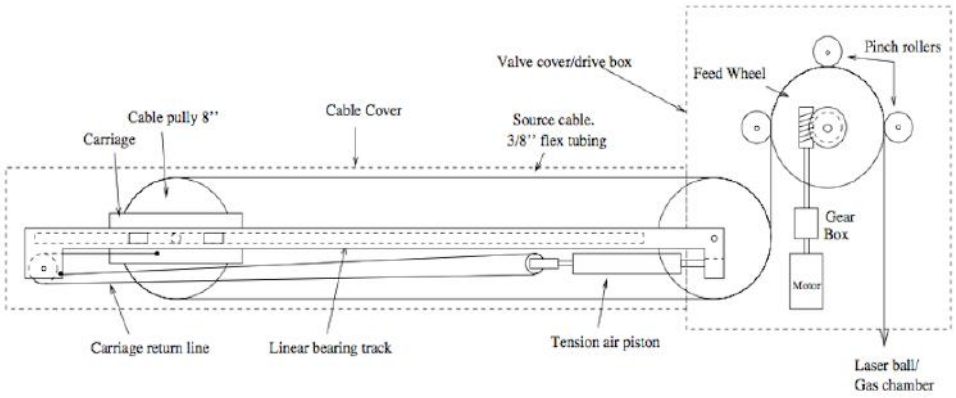

Figure 3.8: The SNO+ umbilical retrieval mechanism which manipulates calibration sources within the detector. The umbilical wraps around a set of textured pulleys [94].

The URM has been upgraded for SNO+ from the SNO model; it now incorporates textured, gripping pulleys to function with the slippery nature of the liquid-scintillator-covered umbilical. The URM is used to deploy and store a central rope that holds the calibration sources and an umbilical that brings services to the sources and is capable of monitoring the deployment with load cells and encoders. It is encased in a sealed box with low-Radon permeability. All the SNO+ calibration hardware has been designed to match the purity requirements of SNO+ and the need to have materials compatible with LAB.

AV deployment of the umbilical is shown in Figure 3.9, along with the source manipulator rope system that is used to manoeuvre different calibration sources inside.

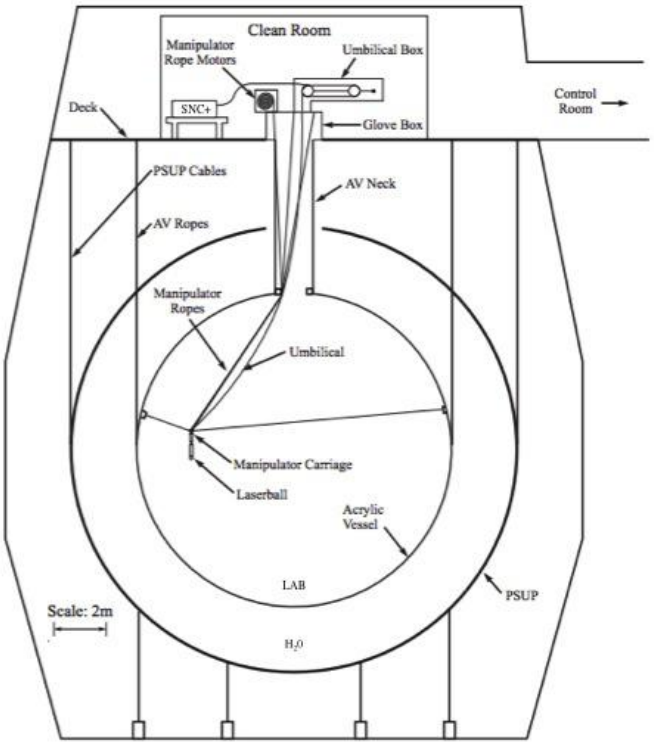

Figure 3.9: Deployment of the laserball calibration system in the SNO+ detector. The laserball enters the detector via an umbilical deployed from the umbilical retreival mechanism (shown in Figure 3.8 and in this image as "Umbilical Box"). A set of ropes adjust the location of the laserball inside the AV. A central rope adjusts the ***** Light from the SNO+ supernova calibration source (SNC+) is carried by the optical fibers in the umbilical and distributed by a glass sphere (laserball) into the scintillator. Figure has been modified from [95].

Calibration sources are attached to an umbilical, consisting of a series of coaxial cables, lines for instrumentation, gas transport and optical fibers inside a LAB-resistant, immersible tygothane tube. The umbilical can be moved up-and-down with the URM and moved side-to-side by a system of high-purity ropes inside the AV in order to scan the detector off the central axis in two orthogonal planes. A new system of cameras in underwater enclosures can be used to monitor the position of the acrylic vessel and the hold-down rope system, and to triangulate the positions of the calibration sources inserted into the detector.

3.8.4 Laserball

The URM and umbilical are also used with a laserball to transfer light into the detector for optical calibrations. The laserball will act as the conduit to the SNC+.

A laserball was used in SNO for both the PMT and optical calibration, and has been upgraded for SNO+. SNO originally used a laser as an optical calibration source in D_20. Light from this laser was transported via optical fibers in the umbilical which entered a laserball device in the detector. The new design is seen in Figure 3.10.

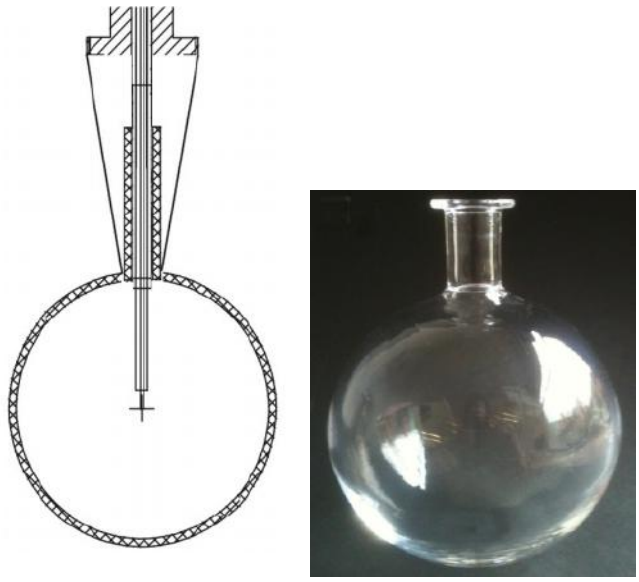

Figure 3.10: The SNO+ laserball has been updated from the original SNO version to include a conical reduced neck allowing for increased isotropy. It consists of a quartz sphere containing glass beads suspended in a colloid mixture. A set of 24 fibers enter the sphere and light is distributed isotropically by the glass beads [96].

The laserball is a light-diffusing sphere which isotropically emits light from the optical fibers in the umbilical into the detector. The laserball was designed and built to calibrate the optical characteristics of the SNO+ detector by emitting a quasi-isotropic light distribution in the far-field (i.e. at distances large compared to the laserball's dimensions). The laserball consists of an 10 cm diameter fuzed quartz flask filled with silicone gel and 50 μm diameter air-filled hollow glass spheres which are suspended in the colloid. In the fabrication of the laserball, a uniform distribution of the scattering spheres was achieved by continuous agitation of the flask during the cure time of the silicone gel. The laserball has an estimated transmission loss of $\sim$40-50% at 420nm [95].

The new laserball allows more light to be incident on the PMTs due to its reduced neck size and increased isotropy, thus the number of photons (PMT hits) is higher for the new laserball design. Simulations have shown that there is an increase in the number of photons emitted within the

angular range most likely to cause a successful PMT hit (see Figure 3.11) and delivery through the laserball is nearly isotropic. This should improve the physics sensitivity for PMTs within the upper hemisphere of the PSUP. Since testing of the new laserball is still in progress, initial calibrations will utilize the existing SNO laserball.

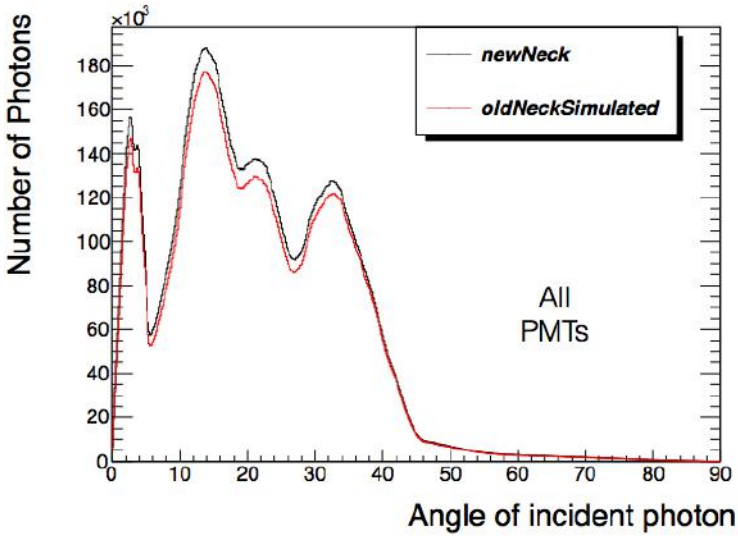

Figure 3.11: Monte Carlo simulations of the laserball photon output before (*old Neck Simulated*) and after (*new Neck*) the modification of the neck. The Number of Photons refers to the incident photons on all the SNO+ PMTs, which is higher for the new laserball (*newNeck*) [97].

3.8.5 Source Tagging

Since continuous supernova monitoring is carried out in SNO+, sources of instrumental background attributed to calibration activities must be considered and possibly rejected as SN neutrino events. Calibration sources give rise to an increased rate of real physics events, and two methods of coping with this increase are used in the supernova monitoring system. Some sources provide an independent tag of calibration events through the detector trigger system, allowing these events to be discarded on an event-by-event basis. Sources which do not tag calibration events require the supernova monitoring system to discard all events below an appropriate NHIT during the source deployment.

3.9 Current Status of SNO+

The upgrades to SNO+ are nearing completion. The first "air-fill" stage of the experiment has been completed, and the water fill of the acrylic vessel has begun.

The scintillator plant is mechanically completed and currently being commissioned. The cover gas system has been installed. PMT repairs and fibre installations are on-going as the water fill proceeds.

The newly installed electronics and trigger system and part of the optical calibration system have been tested in air and partial water fill. The data acquisition (DAQ) software is in place for communicating calibration information and adjusting burst thresholds accordingly. The calibration system requires further installation. The new "slip-proof" umbilical retrieval mechanism (URM) for the calibration sources deployed into scintillator is not yet installed.

SNO+ expects to fill scintillator in 2017 and load tellurium in late 2017. This should allow the start of the double-beta phase to take place in the spring of 2018.

Chapter 4

The SNO+ Supernova Calibration Source

4.1 Introduction

The SNO+ Supernova Calibration Source (SNC+) simulates SN neutrino interactions in the SNO+ liquid scintillator using pulsed light from a high-powered, blue-violet laser diode controlled by a driving circuit and a user interface. Using a set of realistic pulse lengths and energies of a supernova neutrino signal, the source can deposit bursts of photons equivalent to a total deposition energy of up to 60 MeV within the liquid scintillator volume. This equates to all PMTs in the detector being hit multiple times each. This "stress-testing" of the data acquisition system will characterize the detector's ability to process and save data from a nearby supernova event in which a large number of neutrino events could occur within seconds in the detector. Light from the source's laser diode is transmitted via an optical fiber bundle to the laserball which distributes the light isotropically from the center of the detector.

4.2 Design Requirements

There are several design requirements for the SNC+ as it must be (a) realistic (b) flexible and data-driven and (c) safe for both source operators and the SNO+ detector.

4.2.1 Realistic Supernova Pulser

1. The SNC+ must be realistic by producing short pulses of light similar to real supernova neutrino physics events in the scintillator. It's of interest to change the pulse series to mimic various scenarios, but most importantly, create a burst event which will overload the data acquisition system.

2. The SNC+ also has to cover the large dynamic energy range of supernova neutrino emission. As discussed in Chapter 2, supernova neutrinos have mean energies of the order 15-20 MeV, but can reach energies of ∼60 MeV. This dictates that the source have a dynamic range of approximately 0-60 MeV.

3. The pulse energy should be randomly sampled from the expected supernova energy distribution for a more realistic supernova event. Ideally, the pulse energy should be sampled from the expected energy distributions in the SNO+ detector.

4. To more accurately mimic the timing signal of a real supernova, the pulse-to-pulse timing separation should be sampled from a Poisson distribution corresponding to the instantaneous rate. The distribution of the time intervals between successive events is stochastic, thus it will follow a Poissonian distribution with a fixed probability.

5. Moreover, the minimum pulse-to-pulse timing separation should be small enough to produce event pile-up in the SNO+ 500 ns trigger window.

6. The source should also be able to simulate supernovae as close as 0.5 kpc.

7. Lastly, supernova neutrino events would be uniformly distributed within the SNO+ scintillator and evenly illuminate the PMTs to distribute data over all SNO+ crates. The SNC+ should evenly illuminate PMTs within the detector using the isotropic laserball delivery.

4.2.2 Flexible and Data-driven

8. The SNC+ should be able to load a supernova "burst" file into a FIFO memory.

9. The burst file should be calculated in advance for several supernova models and distances.

10. A look-up table (LUT) file should be created which will allow for control over the fineness of energy steps, particularly at low energies. This fine sampling will also allow the SNC+ to be used for other low-energy calibration activities in SNO+, and adequately sample the low-energy $\nu - p$ elastic scattering energy region of a supernova.

11. The SNO+ data acquisition system requires that an electronic "tag bit" be sent, from calibration sources when possible, to the detector electronics to later distinguish calibration source events from real physics events.

4.2.3 Personnel and Detector Safety Features

12. The SNC+ must follow safety regulations of SNOLAB for the source operators and must adhere to the device safety requirements.

13. The source must also be safe for the SNO+ detector's sensitive PMT array and electronics. It is important that uncontrolled light is not present in the detector and that there is a safety interlock system which prevents this.

These design requirements are satisfied by the design decisions addressed in Section 4.4.

4.3 Design Criteria

4.3.1 High-Powered Laser Diode

Design requirements 1 and 2 imply the need of a high-powered optical source to create short pulses similar to real physics events in the scintillator. The optical source must emit light at a wavelength for efficient transmission to the SNO+ PMTs considering the materials and transmission losses.

Figure 4.1 shows the wavelength dependence of the PMT quantum efficiency and acrylic transmission in SNO; SNO+ should have similar transmission values with the exception of Cherenkov absorbance. The PMT QE is most efficient in the region between 300-450 nm, and the acrylic transmission is most efficient in the region >350 nm. This implies that a light source should produce a wavelength in the overlapped regions around 350-450 nm and preferrably closer to 400 nm.

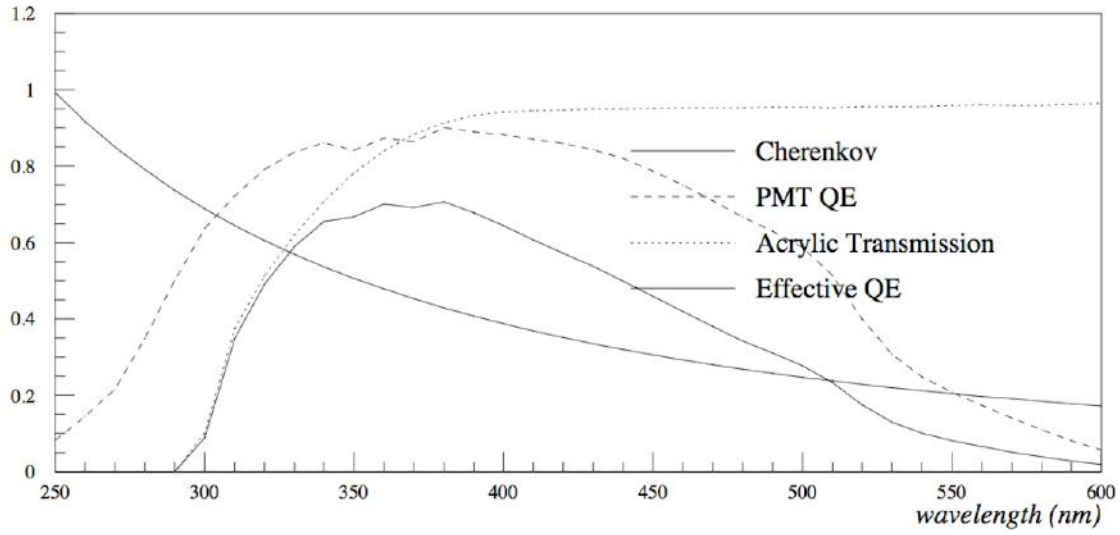

Figure 4.1: Acrylic vessel and PMT QE transmission in the SNO detector. Figure taken from [94].

Several transmission factors were considered in estimating the pulse power required to deliver around 60 MeV in the scintillator volume. The transmission factors can be divided into two categories: internal and external. Internal transmission factors are determined by the components inside the SNC+ whereas external transmission factors result from the components the light must travel through having left the SNC+.

The external transmission of light in the laserball fiber bundle and acrylic vessel was measured during the SNO era, and these transmission factors are listed in Table 4.1 along with some new values to roughly estimate the required light power from a calibration source to reach a pulse energy deposition of 60 MeV in the scintillator. These transmission factors won't be exactly the same for the new SNO+ laserball, which could improve them, but are used as current estimates. For the SNO nitrogen laser calibration system, the following losses were estimated: a 95% loss for the old SNO laserball, a $(1-e^{-2})$ loss for the laserball optical fiber bundle, and a 10% loss for the laserball ST fiber connectors [98]. For SNO+, the following rough transmission losses were included in the laser diode power calculation based on SNO calibration values and current estimates of the SNO+ scintillator mixture transparency:

External Component	**Percent Loss**	**Reference**
Laserball Fiber Bundle	$(1 - e^{-2}) = 86.5\%$	[98]
Upgraded SNO+ Laserball	40%	SNO laserball: ∼40% at 420 nm [95]
LAB Scintillator Mixture	20%	∼20% absorption at 400 nm [99] [100]
Acrylic Vessel	∼10%	@ 406 nm [95]
Cavity Light Water (H_2O)	∼10%	@ 406 nm [95]
PMT Quantum Efficiency	∼78.5%	∼21.5% efficient @ 440 nm [95]
PMT Coverage	∼46%	∼54% PMT coverage [73]
Total External Loss	**∼99.39%**	–
Total External Transmission	**∼0.61%**	–

Table 4.1: Estimated external transmission losses from the SNC+ to the SNO+ PMT array. The total transmission is found using Equation 4.1.

The total percent transmission is calculated using:

$$\%T = \prod_{i=1}^{N} (100\% - \%Loss_i) \tag{4.1}$$

The total internal losses were estimated from the components inside the SNC+ and are indicated in the following table:

Internal Component	**Percent Loss**	**Reference**
SNC+ Internal Optics[a]	30%	estimate
SMA-ST Laserball Fiber Coupler	10%	[98]
Internal Fiber Patches	10%×3	@ 400 nm
Total Internal Loss	**∼54%**	–
Total Internal Transmission	**∼46%**	–

Table 4.2: Estimated internal transmission losses of the SNC+. [a]The internal optics of the supernova source include 2 lens tubes, an iris, 2 spherical lenses and a fiber mode mixer (10%). The total transmission is found using Equation 4.1.

The internal transmission was also determined using Equation 4.1, and this is used to estimate the required power needed from the SNC+.

The SNC+ is the successor to the original SNO supernova calibration source (SNC) which used a green, 530 nm, 115 μW LED (light-emitting diode) pulser. It created variable pulse lengths of order t=100 ns which resulted in 1 NHit per ns of pulse length. Whereas the SNO Cherenkov light

yield was on the order of 8-9 photoelectrons for every MeV (8-9 Nhits/MeV) deposited in the target medium (heavy water, D_20), SNO+ expects on the order of 400 Nhits/MeV within the scintillator. Light yield will be less in light water, H_20, on the order of 8-9 Nhits/MeV. This means that the SNC+ needs to produce more power per pulse to extend to the required energy ($\mathcal{O}$(60 MeV)). This requires a high-mW optical output (considering the external transmission losses that occur from source to laserball to PMT).

Based on these requirements, a high-powered laser diode was chosen for the SNC+. The laser diode power required to deposit 60 MeV in the scintillator is based on the power specifications of the SNO SNC. The SNC LED produced on the order of t = 100 ns pulses of power P = 115 μW for a pulse energy of E = PΔt = 1.15$\times 10^{-13}$ Joules per PMT NHit. To deposit an energy of 60 MeV in the SNO+ scintillator, which has a light yield of 400 pe/MeV or NHit/MeV, we need 400 $\times$ 60 = 24,000 NHits. In a short t=2.5 ns pulse, we find the power needed per pulse of:

$$P_{pulse} = \frac{E_{SNC} \times NHit}{t_{pulse}} = \frac{(1.15 \times 10^{-13} J/NHit) \times (24,000 NHit)}{2.5 \times 10^{-9} s} = 1.104 J/s \sim 1104 mW \quad (4.2)$$

This value already takes into account all the external transmission factors listed in Table 4.1. However, the quantum efficiency (QE) of the PMTs is much higher at the wavelength of the λ=406 nm SNC+ laser diode compared to the λ=530 nm SNC LED as seen in Figure 4.1. Comparing the PMT QE curve at 406 nm and 503 nm, we see that the efficiency is approximately 10$\times$ greater at 406 nm. This means that the pulse power, P_{pulse} can be roughly 10$\times$ less:

$$P_{pulse} = 1104 mW/10 = 110.4 mW \approx 111 mW \quad (4.3)$$

The SNC+ laser diode must then have a power $>$ 111 mW if using a 2.5 ns pulse. Finally, the SNC+ internal transmission losses must be considered when the laser diode light has to travel from the laser diode printed circuit board (PCB) to the fiber output of the SNC+. The total internal transmission of the SNC+ is $\sim$46% (refer to Table 4.2) so the total laser diode pulse power should be upwards of:

$$P_{pulse} = \frac{111mW}{0.46} \approx 241.3mW \tag{4.4}$$

Digital Events

Design requirements 3 and 4 necessitate a digital design of the SNC+ wherein a supernova "event" can be specified by intensity and a time in between events which can both be encoded as a single number. This allows for the pulse energy and timing separation to be sampled from the appropriate distributions describing realistic supernova events.

Because of requirement 5 which dictates that the minimum pulse-to-pulse timing separation should be small enough to produce realistic event pile-up in the SNO+ 500 ns trigger window, the minimum time in between each event must be << 500 ns, which implies the need for a high pulse rate > 2 MHz.

The expected flux (as detected on Earth) from a 1 kpc supernova is on the order of 50,000. This implies the need for an event capacity >50k at least. Considering our requirement to simulate supernovae as close as 0.5 kpc, the SNC+ should be able to cover an event count greater than ∼200,000.

Requirements 6 and 8 suggest the use of digital memory in the form of a FIFO[1] which can hold the values from a burst file. The memory size is determined by the supernova event count which can be upwards of 100s of thousands at 0.5 kpc. A memory size of 1MB for 256K 32-bit events can be used with a 16-bit digital-to-analogue convertor (DAC) to cover this requirement. This also demands the use of FPGA[2]. circuitry, which can transfer data in a sophisticated manner.

Requirement 9 mentioned that the burst file should be calculated in advance for arbitrary supernova models and distances. This implies the need to be able to load data into memory from a computer, specifying a file format, specify an event size, energy and time in bytes.

To control the fineness of energy steps in the file, a lookup table can be introduced which can calculate fine or coarse energy sampling by translating bits into the full energy range of the DAC.

[1] FIFO is an acronym for "first in, first out", a method for organizing and manipulating a data buffer, wherein the oldest (first) entry is processed first. FIFOs are commonly used in electronic circuits for buffering and flow control between hardware and software. In its hardware form, a FIFO primarily consists of a set of read and write pointers, storage and control logic. The SNC+ FIFO is implemented as a hardware shift register.

[2] An FPGA or field-programmable gate array, is an integrated circuit designed to be configured after manufacturing – hence "field-programmable"

The tag bit must be generated by the SNC+ for the detector to distinguish events. A BNC cable running from the SNC+ to the detector electronics allows for this.

Calibration Delivery

To satisfy Design Requirement no. 7, the SNC+ will use the laserball calibration system described in Section 3.8 to evenly illuminate the PMTs. To use this calibration system, the SNC+ needs to match to a fiber bundle of 24 fibers with a coupling diameter of 1 mm. Thus the SNC+ needs to have a 1 mm coupling fiber and a mode mixer for uniform illumination of the fiber bundle.

Safety Designs

Because of requirement 12, several features must be included in the calibration source to reduce and/or eliminate the risk to operators. The American Laser Safety Committee requires that all laser-containing devices have an involved interlock safety system with a keylock, closed containment box, indication lighting, mechanical laser shutter. SNO+ requires that calibration sources containing laser devices have similar safety features including an operator's user manual.

As mentioned, the SNC+ must also be safe for the SNO+ detector. The design must not include a failure mode where the laser diode remains on. An emergency off mushroom button in the SNO+ control room is used to cut power in case of an emergency.

4.4 Final Component Selection

It was decided that a 406 nm 210-250 mW SHARP GH04P21A2GE [101] laser diode (LD) meets the requirements of the source (no. 1-4) and was easily available at a reasonable cost. The initial idea was to use a current digital-to-analogue convertor (DAC) to drive the laser diode wherein the DAC input was proportional to the laser diode current and the light output. The final design consists of a 16-bit 500 MHz DAC along with a high-powered fast op-amp as a current source through the LD.

To allow for pulse pile-up in the DAQ (Requirement 5), the time to the next event could be measured in ticks of a 12.5 MHz clock. This gives a minimum time separation between SNC+ events of 80 ns which is good for pile-up in a 500 ns detector event time window.

A 32-bit event size was convenient for programming with some bits specifying the pulse intensity and the rest specifying the time delay between pulses and would satisfy Requirements 6 and 8. The initial thought was to use a FIFO with a capacity for 10^6 events, which would require a 4 MB memory. However, the Altera starter kit that we selected to use had a 1 MB memory chip which meant 256K (= 256×1024 = 262,144 events at 32 bits) could be used instead of 1M = 1,048,576. 256K events is enough for simulating an event rate correlated to a supernova as close as 0.5 kpc. This was a compromise because there were many benefits to using the Altera starter kit (i.e. reasonable cost, simple design, included clock and additional features).

We also selected 1 mm SMA fiber connectors, 1 mm fiber patches, and a mode mixer to uniformly illuminate with the laserball's fiber bundle (Requirement 7). This drove the whole optical design and selection of the internal optical Thorlab components discussed in the next section.

The NI USB-8451 and LabWindows GUI were selected based on the need to be able to load files into memory (Requirements 9 and 10).

The event size of 32 bits was divided into energy and time information, wherein 24 bits were allocated to timing and 8 bits to pulse energy. The 24 bit timing word gives a range of 80 ns - 1.34 s intervals based on the 12.5 MHz clock frequency. The 8-bit energy words are translated into 16 bits through the look-up table. The LUT can be customized to allow for finer energy sampling in regions of interest.

To meet the safety requirements 11 and 12, an interlock system was designed for the source which removes power from the normally-closed shutter. A keylock is used to enable the system. A proximity switch is used to satisfy the condition that the laserball fiber is connected. An emergency-off button was also designed to be located in the detector control room which removes power from the Altera board immediately upon depression of the mushroom button.

4.4.1 Digital Design

The SNC+ is a data-driven laser diode pulser capable of producing ∼2.5 ns 0-200 mW 406 nm pulses with repetition rates up to 12.5 MHz. Its digital design is depicted in Figure 4.2.

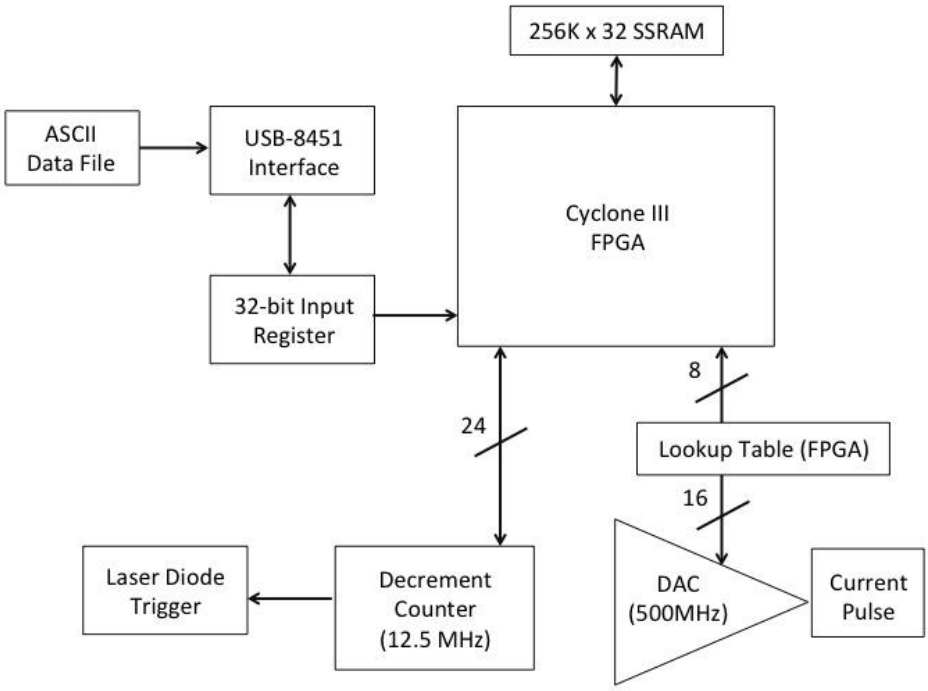

Figure 4.2: The basic digital design of the SNC+.

The input to the SNC+ is an ASCII file with entries that specify a burst of pulses simulating a supernova. The file can be generated via Monte Carlo simulation or by other means[3] and consists of a vector of up to 256K x 32 bit events. The ASCII file is loaded into a 32-bit FIFO input register via USB SPI communication. Each pulse is described by 32 bits split into pulse spacing and amplitude values. 24 bits are allocated to the timing between pulses (values range from 0 to 16,777,215). The timing word is copied to a decrement counter which counts down to 0, at 12.5 MHz, to trigger the diode. (This programmability is achieved through use of the FPGA). The dynamic range of 12.5 MHz down to 0.75 Hz allows for a simulation of pile-up in SNO+ which has a ∼400 ns trigger window. The other 8 bits of the 32-bit pulse word specify the amplitude of the pulse. A user-definable lookup table converts the 8-bit amplitude value into a 16-bit word for the 16-bit voltage DAC. The choice of lookup table allows for finer sampling at lower energies and courser sampling at higher. A voltage DAC operating at up to 500 MHz, combined with an op-amp current source, converts the digital DAC amplitude signal to an analogue current pulse through the

[3]The SNC+ event file can be modified to provide a random time intervals between pulses based on the Poisson distribution. To more closely resemble supernovae, the laser diode pulse amplitude could also be sampled from expected SNO+ energy distributions.

laser diode. In between pulses, a 16-bit user-definable "idle DAC" value is sent to the DAC input at its operating speed.

The FPGA was programmed by Jean-Pierre Martin at the University of Montreal in collaboration with the SNO+ Supernova Group. This involved setting up the FIFO and its associated controller, various registers, and command interpretor.

J.P. Martin also designed and constructed the laser diode PCB which contains resistors, capacitors and several voltage regulators, and an analogue op-amp to drive the laser diode.

A notional layout for the DAC daughterboard was developed at Laurentian, and J.P. Martin's group finalized the design, circuit schematics, purchasing of components, PCB fabrication and testing. The daughterboard is shown in Figure 4.3 and schematics for the design are found in Appendix C.

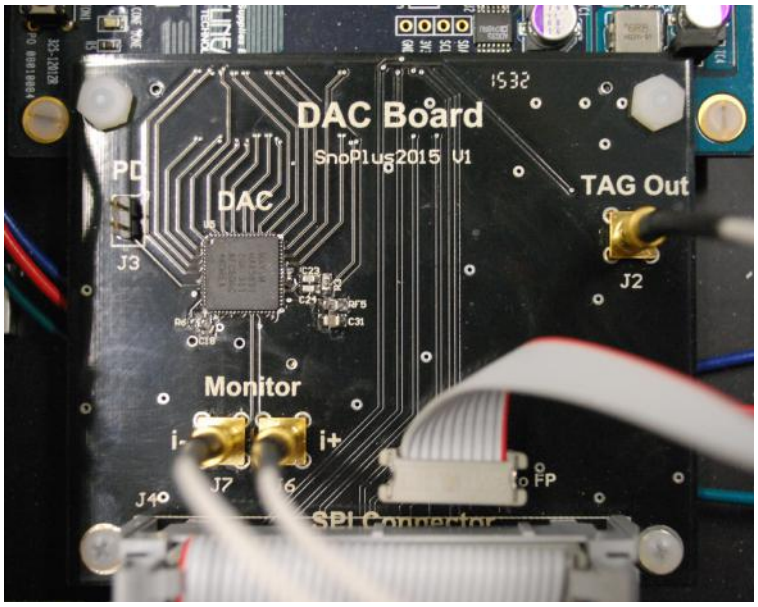

Figure 4.3: The DAC daughterboard (J.P. Martin).

The DAC daughterboard (containing a Maxim 5891 16-bit voltage DAC chip) interfaces with the USB board, the laser diode PCB, the Altera Cyclone III FPGA board, and a front panel display and interlock safety board. The DAC also contains the output for the tag bit which is sent via BNC cable to the SNO+ Digital Master Trigger Card (MTC/D). A 10-pin header on the daughterboard provides connections between the LEDs on the front panel PCB and the USB-8451 board. The daughterboard contains the signal connections to the laser diode PCB Signal (Sig) connectors.

A Samtec ASP-122952-01 HSMC male connector is placed on the upper underside of the board such that it connects to the mating connection of the Altera host board header (Samtec ASP-122953-01 HSMC female connector) when the daughterboard is placed on top. Part of the FPGA programming generates a TTL tag bit that is re-triggerable and that has a programmable delay, set by the contents of a register with respect to the LD pulse time, and that has a programmable width, set by a second register. The MCX connectors ($J6$ and $J7$ or $i+$ and $i-$) attach to cables heading to the MCX Signal connectors of the laser diode PCB. The daughterboard $J6/i+$ connection sends the signal, and the $J7/i-$ connection terminates in 50 Ω when not attached to a scope. A 500 MHz clock is generated within the FPGA and passed through the HSMC (high-speed mezzanine card) connection to the DAC chip. A 10-pin header interfaces with the header on the front panel PCB which contains the LED indicators and shutter safety circuitry (See Appendix C for connection mapping).

4.4.2 Optics and Analogue Design

Overview

The SNC+ uses a SHARP GH04P21A2GE high-power blue-violet laser diode (LD), commonly used in Blu-ray DVD disc recording, as a light source. Several LDs that were purchased were presumably extracted from unused Blu-ray DVD players. With an estimated 6× recording speed for dual-layer Blu-ray^{TM} discs, these laser diodes are capable of ∼216 MBPS (MHz) signal speeds. Most of the intrinsic properties of this model are corporate secrets, but we assume this diode to be based on an InAlGaN semiconductor chip material as are most blue-violet laser diodes in this power category. The laser diode has a typical wavelength of 406 nm which is within the acceptable wavelength range for the SNO+ scintillator mixture. The laser diode also has a pulse optical maximum power output of 210 mW within a small ϕ 5.6 mm can package. An op-amp is used to drive the laser diode; this is described in the next subsection.

Driving PCB

The laser diode is inserted into a socket and mounted on a custom-designed PCB which contains the circuitry for driving the LD. The laser diode PCB (seen in Figure 4.4) is attached directly to an

aluminum heatsink with nylon standoffs and is powered by an isolated voltage supply (+12V and -6V) via two shielded MCX coaxial cables that provide low-RF interference and GHz performance. Another MCX cable for the laser diode pulse signal exits the PCB and attaches to the DAC daughterboard. The heatsink also serves as a collimation and lens tube for the laser diode light.

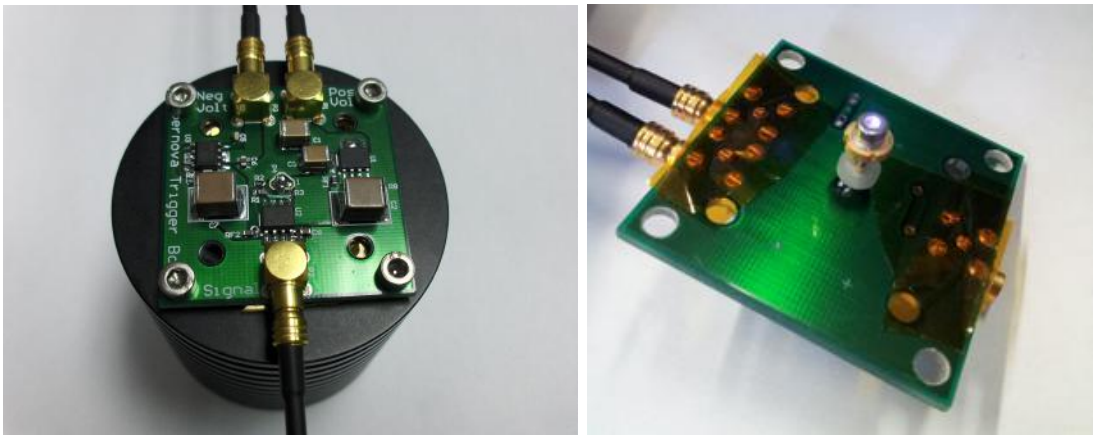

Figure 4.4: (a) Laser diode printed circuit board attached to the heatsink collimator (b) Underside of the PCB showing the laser diode in its socket.

The PCB circuit is seen in Appendix C. It features the op-amp which drives the laser diode. In pulsed mode, the single AD8009 op-amp can deliver somewhere between 175-330 mA. The PCB has low-ESR 100 μF capacitors on the voltage regulators to prevent excessive RFI radiation.

Theoretical Pulse-Shape

The pulse shape of the diode was initially tested at The University of Montreal with a SPICE model based on the circuit design (J.P. Martin). Based on Figure 4.5, the signal showed a rise time of roughly 2 ns and a pulse width on the order of 4 ns. The drive signal is longer than the delays due to wire lengths. It was determined that the system would be completely stable in pulse reproduction.

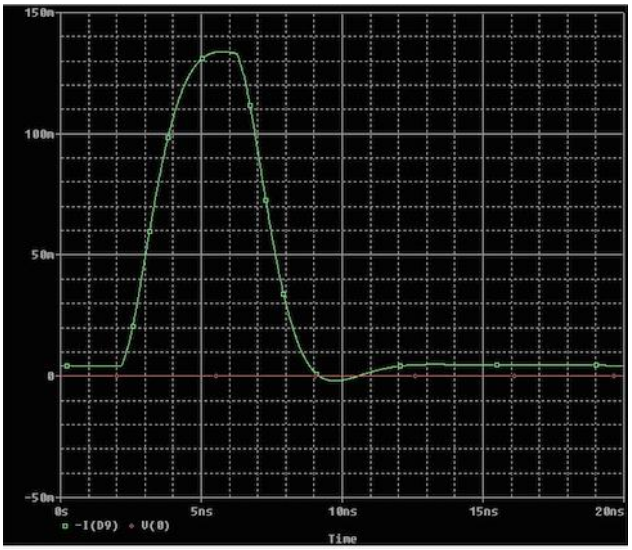

Figure 4.5: SPICE model of the laser diode pulse based on circuit design (J.P. Martin).

Power and Current Characteristics

The laser diode power and current characteristics, taken fom the model specifications, are seen in Figure 4.6. In the left plot, the optical power output, P_O, of the diode is a function of the forward current, I_F, supplied to the diode. A linear extrapolation of the 25°C curve to an optical power output of ∼250 mW correlates to a forward current of ∼188 mA in the diode. Using the equation for the line of 25°C ($P_O = (1.64)I_F$ - 59), the x-intercept of the curve was found to be a forward "threshold" current, I_{th}, of ∼36 mA. The slope of this extrapolated linear curve was found to be: $I_F = 101.62$. At lower currents, below the lasing threshold, the laser diode undergoes spontaneous emission[4], and after I_{th}, the diode begins stimulated emission. The right plot of Figure 1.13 shows the forward voltage vs. the forward current in the diode. Extrapolating the 25°C curve to a current of 188 mA implies a forward voltage of approximately 5.8 V for the laser diode to operate with a 250 mW pulse.

[4]Spontaneous emission below the lasing threshold has similar properties to that of a laser-emitting diode (LED). As the forward bias across a laser diode is increased, stimulated emission occurs in the active layer. Stimulated emission thus becomes dominant at a certain bias point called the "lasing threshold" or "threshold current", I_{th}. Injected current above the threshold induces stimulated emission and coherent light is emitted from the laser diode.

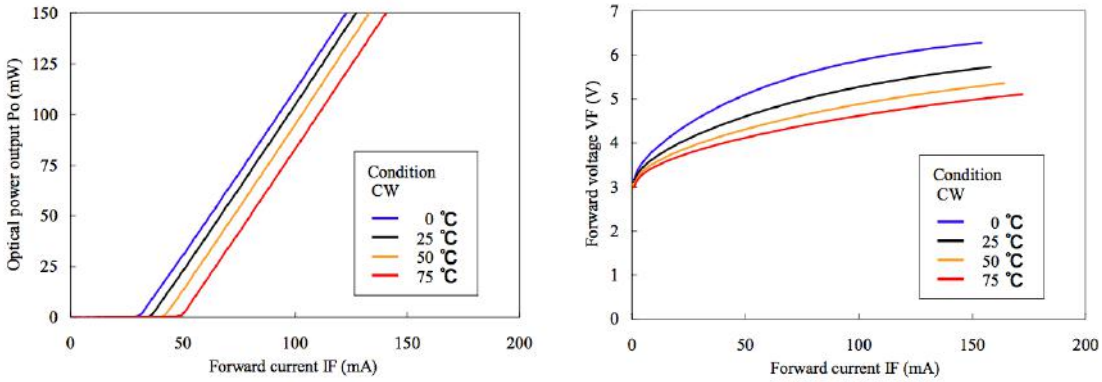

Figure 4.6: **Left**: SHARP GH04P21A2GE laser diode luminosity vs. applied forward current on the diode. The current at which the laser diode stimulated emission occurs is the threshold current (I_{th}). **Right**: Forward voltage vs. applied forward current across the laser diode.

Optical Characteristics

The stimulated emission wavelength of the laser diode is negligibly dependent on the optical power output as seen in Figure 4.7. The typical wavelength of a laser diode is directly proportional to its operating temperature. Increases in power cause a shift towards slightly longer wavelengths as seen in Figure 4.7. LD's typically have a wavelength tolerance of ±10 nm. The SHARP laser diode should have a wavelength of 406±10 nm based on the manufacturer's quotes. It may be of interest to measure the true wavelength of the laser diode as a function of its operating power range in later studies.

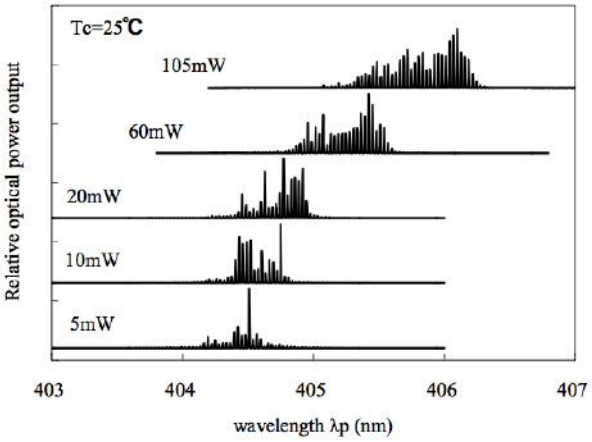

Figure 4.7: Stimulated emission wavelength dependence of the SHARP laser diode.

The 406 nm wavelength is reasonable for the SNO+ detector considering transmission losses

and scintillator mixture absorption levels as seen in Figure 4.8. The combined absorption is lowest in the region around 400 nm and after 450nm. It's unsure whether the scintillator will contain perylene at this stage, so the lowest absorption region is being taken as 400 nm or longer.

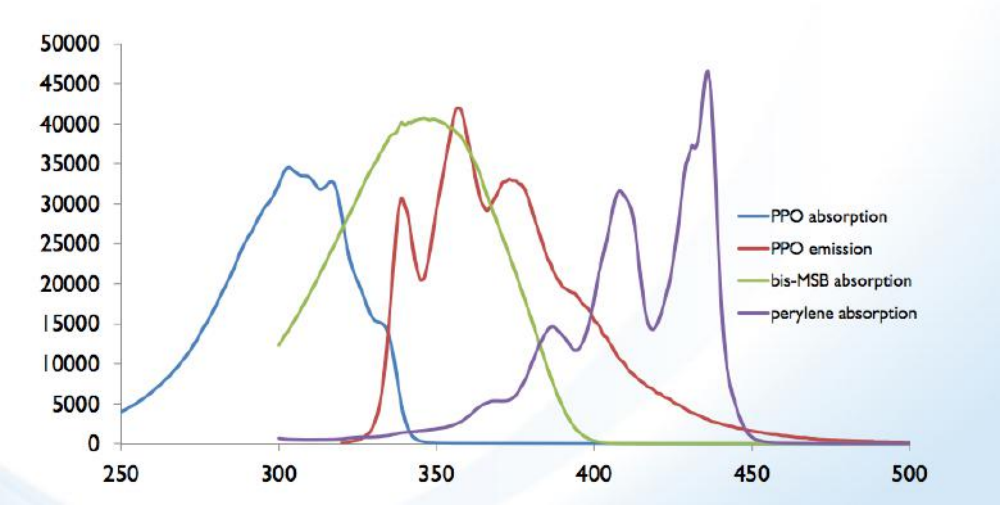

Figure 4.8: Absorption in scintillator mixture vs. wavelength (nm) [102].

The can of the laser diode has a small lens which diverges the beam into an elliptical field pattern. In a laser diode structure, optical radiation is confined in both the transverse and lateral directions by a refractive index step. The field pattern is a result of light from both the perpendicular and parallel planes. The field distribution can be approximated by a Gaussian function with two different widths along the parallel and perpendicular axes to the junction plane as seen in Figure 4.9. The radiation pattern is more divergent in the perpendicular plane. The width of the perpendicular field pattern with angle of divergence $\theta_{\perp}$ at 50% of maximum amplitude (Full-Width-Half-Maximum) is $\sim$20-24° whereas the width of the parallel field pattern is $\sim$8-12°. The perpendicular angle, $\theta_{\perp} = 24°$, was used to calibrate the optics in the next section.

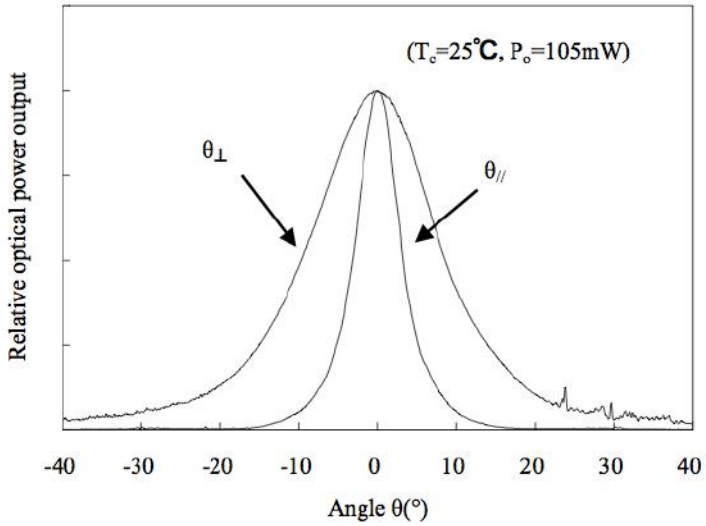

Figure 4.9: Radiation pattern from the elliptical light cross-section of the laser diode. The value of $\theta_{\perp}$ is found at FWHM.

Optical Hardware

The optical hardware used in the SNC+ is seen in Figure 4.10. As previously mentioned, the laser diode is powered by a custom PCB. The laser diode pins are inserted into a socket mounted on the PCB. A locking ring surrounding the diode couples to an adjustable iris which is set to a 1-mm wide opening. The iris which is thermally connected to the laser diode can is attached to a passive heatsink lens tube, rated for a temperature rise of 0.25 °C/W of heat dissipation. The anticipated temperature rise would therefore be ∼0.06°C for 250 mW maximum diode power if run DC and substantially less for a low-duty cycle pulsed operation as is actually foreseen.

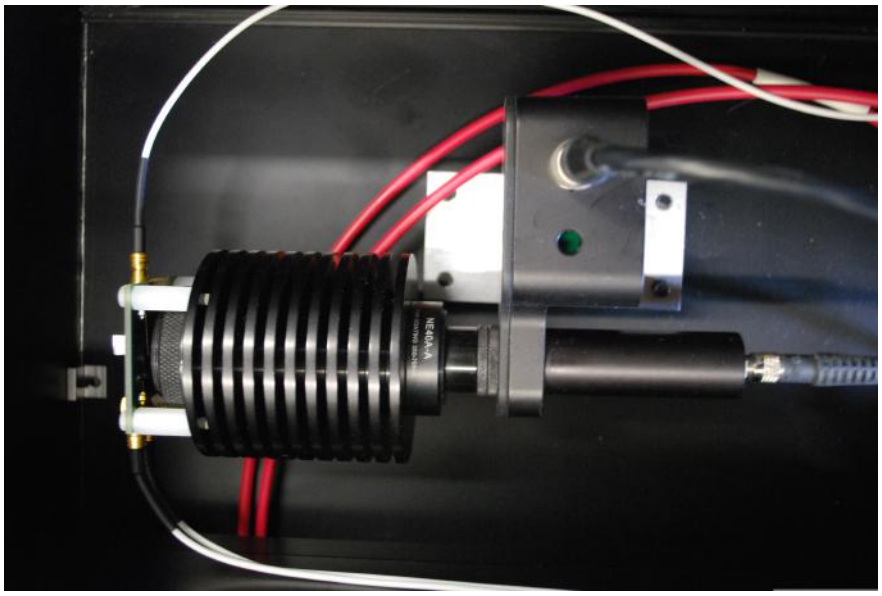

Figure 4.10: Overhead view of the source optical system.

The heatsink serves as a lens and neutral density filter (NDF) holding tube. A 1" lens and several 1" NDF filters can be inserted with locking rings within the heatsink lens tube. The end of the heatsink makes a connection with a lens tube adaptor which allows for a transition to a 1/2" tube. An electro-mechanical beam shutter connects to the 1/2" opening and is controlled by the SNC+ interlock system of the front panel PCB. The second 1/2" lens tube connects with the shutter exit hole and contains a 1/2"-diameter plano-convex lens. A lens tube SMA fiber adaptor

connects at the end to provide coupling with a 1 m fiber patch cable. This cable terminates in a small homogenizing mode mixer which couples to another 1 m fiber patch cable which then terminates at the fiber coupler/sensor device on the front panel. These two fiber patch cables coil underneath the raised chassis platform such that their minimum bending radii requirements are met. This hardware is further described in Section 4.6.

Two (1" and 1/2") plano-convex spherical lenses were used to focus the light output of the laser diode into a low-divergence beam. The 1" lens was used to make a parallel beam from the beam diverging from the laser diode, while the 1/2" lens was used to inject the parallel beam into a 1-mm fiber opening.

To determine the focal point of the first 1" lens needed, the following equation was used:

$$f_1 \simeq \frac{D_1}{2tan(\Theta_1)} \tag{4.5}$$

where f_1 is the focal point of the 1" lens which dictates the placement of the lens from the laser diode can; D_1 is the diameter of the parallel beam exiting the lens (this needed to be less than 1/2" to meet the second lens tube, thus D_1 was chosen to be 11 mm); and Θ_1 is the half-angle of the perpendicular angle based on Figure 4.9 at FWHM ($\Theta_1 = \frac{\Theta_\perp}{2} \simeq 12°$). Therefore, $f_1 \approx 12.4$ mm.

A roughly 11 mm-diameter parallel beam exits the first lens and travels through the neutral density filters, the shutter opening and into the second lens where it is converged to a 1 mm-diameter fiber core surface. The focal point for the 1/2" lens, f_2, was chosen to be 40 mm from the focal point within the fiber. The purpose of this was to decrease the entry angle of the light from the lens into the fiber's 1 mm surface diameter and ensure that this angle was less than the fiber's acceptance angle for maximum light input. To reach a beam diameter of D_2=1 mm from D_1=11 mm, the lens should be set at $d = f_2 - x$ where x is the distance from the focal point inside the fiber to the fiber edge. Based on the ratio $\frac{\Theta_1}{f_2} = \frac{D_2}{x}$, x was determined to be 3.6 mm, thus the placement of the lens was at $d = 36.4$ mm as indicated in Figure 4.10.

The step-index, 1-mm multimode fiber that accumulates the light from the 1/2" lens tube has a half-angle of acceptance of 15°, which is larger than the converging beam half-angle of entry to ensure full light acceptance.

These lens placement calculations were made prior to optical tests performed in a dark room to

characterize the output of the laser diode. With the 1" lens in place at f_1, the beam profile exiting from the heatsink was observed at various distances to ensure a parallel beam. Because the lens placement calculation was based on an estimate of only the laser diode's perpendicular divergence, excluding its parallel divergence, the full beam exiting the lens was not completely parallel. To compensate for this, the 1" lens position was slightly adjusted to obtain a parallel beam up to ∼3 m away.

When the light from the laser diode was viewed on a flat surface, it was found that two distinct half-moon patterns flanked the elliptical (shown as circular) signal region when the laser diode was powered on. These two half-moon patterns, as seen in Figure 4.11, which appear alongside the circular signal spot needed to be removed as these were present below the lasing threshold and were due to the spontaneous emission[5] produced by the laser diode. An iris was then needed to exclude this extraneous light, and it was set to a diameter of 1-mm which allowed the stimulated emission (signal) light controlled by the SNC+ DAC to pass through.

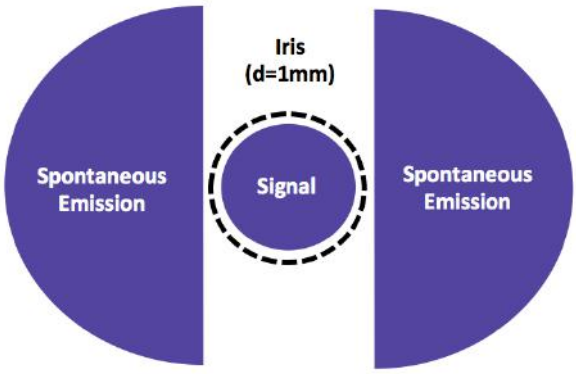

Figure 4.11: Light field pattern from the laser diode can. Two half moon spots appear surrounding the stimulated emission region prior to sending a current DAC value as a result of spontaneous emission. As higher DAC values are sent, the stimulated emission spot appears intensifies in the center. An iris at a diameter of 1mm was used to allow the center "signal" light to pass.

During commissioning of the SNC+, which is discussed in full in the next chapter, a small PMT was attached to the fiber output. Because the PMT saturated from the full output of the laser diode at maximum DAC value, several combinations of neutral density filters (NDFs) were placed in the 1" lens tube to reduce the light output. NDFs will not actually be used during SNO+

[5]Spontaneous emission of laser diodes is discussed further in Chapter 5.

calibration events and normal operation as the light will not need to be reduced during pulsing.

NDFs reduce the transmission by optical density factors (ODFs). For example, the NDF05 is a neutral density filter with an optical density of 0.5 and reduces the light intensity in the lens tube by a factor of $10^{0.5}$. The NDF05 is shown held up to light in Figure 4.12.

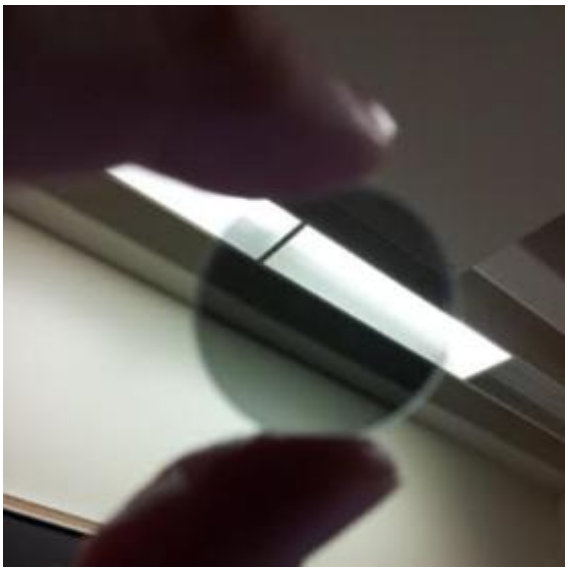

Figure 4.12: Neutral Density Filter with an optical density of 0.5 (NDF05) held up to visible light. Several neutral density filters can be combined in the lens tube to reduce the overall intensity of the diode.

4.5 User Interface and Operation

The SNC+ was designed to be easy for users to operate. A LabWindows/CVI interface was programmed for the system to communicate with the system's USB-8451 card and DAC daughterboard.

The pin assignments and their signal descriptions for the USB-8451 connector which are derived from the NI USB-8451 user manual are also shown in Appendix C. The USB-8451 board had several available registers in the form of chip selects, and 3 were chosen for the purposes of the SNC+ as listed in Table 4.3. Chip select signals are outputs used to select a desired SPI peripheral device - in this case, the FIFO registers. SPI protocol and chip select features of the USB-8451 are used to pass commands and data between the LabWindows user interface program and the FPGA.

Table 4.4 and Table 4.5 give a detailed description of the CS0 FIFO Command Register's bit allocation and command usage.

Chip Select Signals (SPI)	J1 Pin	Allocation	Details
CS0	16	Command Register - 16 bit (W)	see Table 4.4 for list of commands
CS1	20	Data Register - 32 bit (R/W)	for loading FIFO
CS2	24	Progress Feedback Register - 32 bit (R)	current event no. (FIFO pointer); max FIFO size is 256K (18 bits)

Table 4.3: Chip select allocations of the USB-8451.

Bit No.	Command	Requirements	Description
0	Read/Write	bit not set: Reading; bit set: Writing	used in conjunction with other bits
1	*RUN/PAUSE*	ignores bit 0; bit not set: PAUSE; bit set: RUN	
2	*RESET*	valid for bit 1 set to *PAUSE*	sets the pointer back to the start of the FIFO
3	*CLEAR*	valid for bit 1 set to *PAUSE*	clears both pointers
4	Load FIFO	bit 1, 2, 3 not set; valid for bit 0 set to Write	
5	Load Look Up Table	bit 1, 2, 3 not set; valid for bit 0 set to Write	can be used when bit 1 set on or off for LUT readout
6	Set Tag Bit Delay	ignores bit 1; valid for bit 0 set to Read or Write	
7	Set Tag Bit Width	ignores bit 1; valid for bit 0 set to Read or Write	
8	Set Idle DAC value	bit 1, 2, 3 not set; valid for bit 0 set to Read or Write	
9	*REPEAT*	valid for bit 2 set; bit 3 not set	allows repetition of file when end of file reached and pointer reset to start

Table 4.4: Command register (CS0)

Command Register (CS0)										
	Command Only (no data)					Command + Data		Command + Data (manual load required)		
Command, Bit No. (n)	PAUSE	RUN	RESET	CLEAR	REPEAT	LOAD FIFO	LOAD DAC LUT	SET TAG DELAY	SET TAG WIDTH	SET IDLE DAC
Read/Write, 0	ON	ON	ON	ON	ON	ON	ON	ON	ON	ON
Run/Pause, 1	OFF	ON	OFF	OFF	X	OFF	OFF	X	X	X
RESET, 2	OFF	OFF	ON	OFF	ON	OFF	OFF	OFF	OFF	OFF
CLEAR, 3	OFF	OFF	OFF	ON	OFF	OFF	OFF	OFF	OFF	OFF
Load FIFO, 4	OFF	OFF	OFF	OFF	OFF	ON	OFF	OFF	OFF	OFF
Load LUT, 5	OFF	OFF	OFf	OFF	OFF	OFF	ON	OFF	OFF	OFF
Set Tag Delay, 6	OFF	OFF	OFF	OFF	OFF	OFF	OFF	ON	OFF	OFF
Set Tag Width, 7	OFF	OFF	OFF	OFF	OFF	OFF	OFF	OFF	ON	OFF
Set Idle DAC, 8	OFF	OFF	OFF	OFF	OFF	OFF	OFF	OFF	OFF	ON
REPEAT, 9	OFF	OFF	OFF	OFF	ON	OFF	OFF	OFF	OFF	OFF
Command Value:	1	3	5	9	517 or 519	17	33	65 or 67	129 or 131	257 or 259

Table 4.5: Command register (CS0) logic. **ON** and **OFF** indicate bit status.

4.5.1 Altera Board and FPGA Programming

Commands and data are passed to the SNC+ field-programmable gate array (FPGA) from a LabWindows/CVI GUI written in the C language. Programming of the FPGA was completed by J.P. Martin. Communication is through a USB connection to a NI USB-8451 board via USB protocol. The USB sends data to the Altera registers via SPI communication. By writing commands and data to registers defined within the FPGA, the initialization, loading, and operation of the SNC+ is controlled. From the user interface, the FPGA allows the following functionality:

1. load an ASCII SN burst file (up to 256K x 32bit) to a FIFO register
2. load the DAC lookup table (fixed size 256 x 16 bits)
3. issue a *RUN* command which begins the FIFO pointer movement down a file
4. issue a *PAUSE* command which pauses the FIFO pointer
5. issue a *RESET* command which resets the FIFO pointers to the top of the same ASCII file, ready for the next run
6. issue a *CLEAR* command which clears the FIFO contents
7. set the tag bit delay (4 ns ticks, 2 μs max delay) when paused or running
8. set the Tag bit width (4 ns resolution, 2 μs max) - possible to change while running
9. set the "idle" DAC value while either paused or running

4.5.2 User Interface Software

The graphical user interface (GUI or UI) for the SN source was developed for the Windows source laptop using LabWindows/CVI in the C language. LabWindows/CVI is a graphical development environment that integrates C programming scripts. The UI controls the SN calibration runs by communication with the USB-8451 in SPI. A screenshot of the user interface is seen in Figure 4.13.

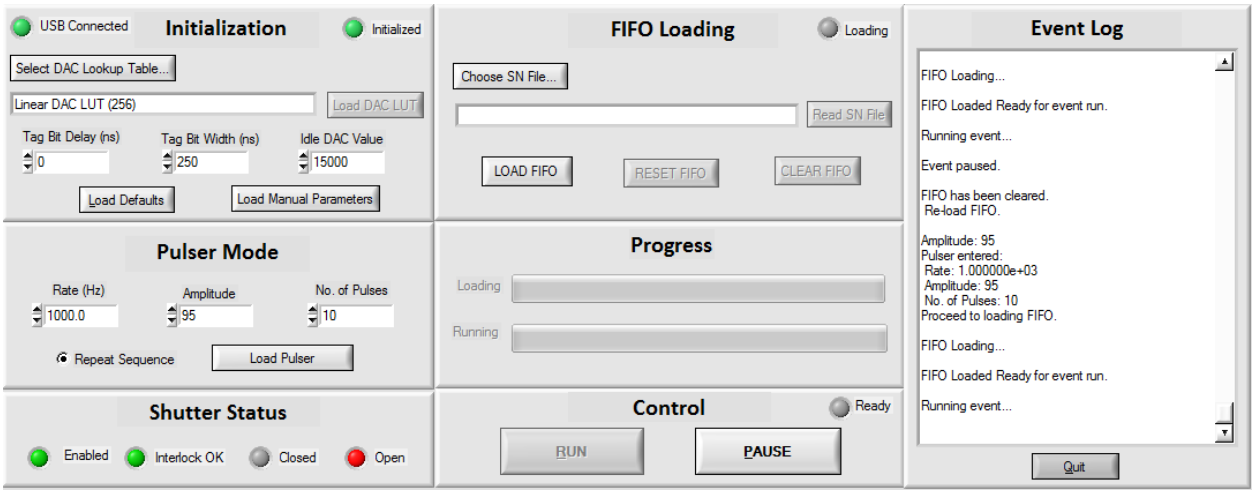

Figure 4.13: The SNC+ LabWindows/CVI graphic user interface communicates with the USB-8451 board. The GUI is primarily written in C and consists of 7 block sections: Initialization, Pulse Generator Mode, FIFO Loading, Progress Feedback, Run Control, Shutter Status, and User Messaging.

The SN source user interface (UI) has the following features and functionality:

1. Ability to read the shutter interlock status bits from the SNC+ front panel PCB upon start-up and periodically throughout program run time

   (a) *Enabled*: the keylock on the front panel has been turned to the *Shutter Open* position

   (b) *Interlock OK*: the external fiber is attached to the SMA fiber output on the front panel; the emergency button has not been depressed; the keylock has been enabled

   (c) *Closed*: the shutter is closed

   (d) *Open*: the shutter is open

2. Ability to load a DAC lookup table to translate an 8-bit number to a 16-bit word, allowing for a user-defined, non-linear intensity map

3. Pulse Generator Modality: specification of a fixed frequency, intensity and duration of a non-file-based burst

4. SN ASCII burst file selection from a directory

5. Ability to load the FIFO register with the selected file or pulse configuration

6. Ability to load the other parameters (DAC idle value; Tag bit delay; Tag bit width to SNO+ MTC) and to change these values while the SNC+ is executing a burst

7. robust FIFO contents control (*Load, Reset, Clear, Run, Pause*) for prevention of unwanted signals to the laser diode

8. Ability to set the SNC+ chassis front panel LEDs to indicate calibration event run status:

   (a) *Initialized*: the lookup table and other parameters are loaded

   (b) *Loading*: the ASCII file is currently being loaded into the FIFO

   (c) *Ready*: the ASCII file has been loaded and FIFO pointers are set for execution

   (d) *Running*: the laser diode event is being generated

9. Progress Bars: to show the progress in either loading a burst file to the FIFO register or executing a loaded burst function.

Start-up Initialization Tasks

Upon program start, the UI reads the shutter status bits and indicates whether a laser diode run can occur. The shutter status is then read cyclically by a programmable time interval.

Calibration Run Initialization

A SN calibration run must first be initialized. In the Initialization block, "LEDs" show USB connection status and source initialization status. The *Load Defaults* button allows for a linear DAC LUT to be entered along with a user-defined default tag bit pulse delay and width.

There is also the option of manually loading a LUT and initialization parameters through Load Manual Parameters. Select DAC Lookup Table will open a pop-up file-selection menu filled with various LUTs that allow both fine and coarse energy sampling.

Pulse Generator

A pulse generator in the program allows for time duration and pulse energies to be selected with an input of Pulse DAC amplitude, number of pulses, and frequency.

FIFO Loading

An ASCII file can be loaded into the FIFO (CS1 Data Register). The CS0 Command Register defines the reset and clear functions for this feature. A progress feedback register (CS2) allows the FIFO pointer to be read during loading.

Calibration Run Control

A Control panel includes indication for FIFO loading completion (LED Ready). Run and Pause buttons send commands to the FPGA as defined in the CS0 command register. Control of the digital signal is not only controlled by the UI, however. The emergency off switch is a physical cut to power and will override the UI signal. A progress bar indicates the run status of the SN event as determined by the FIFO read pointer.

Indication

An indication panel displays the shutter status from the front panel. The code will not perform a FIFO load or run if the shutter is not enabled, the key interlock is not ok (ie. set to *Open*), or the shutter is closed and will return an error message through the event log message board.

4.6 Hardware and Construction

The SNC+ is within a chassis which will be mounted in a 19" rack in the deck clean room (DCR) located above the SNO+ detector and will be operated remotely from the SNO+ control room. The anodized aluminum 3U chassis was custom designed and ordered through Front Panel Express. A photo of the front of the source is seen in Figure 4.14.

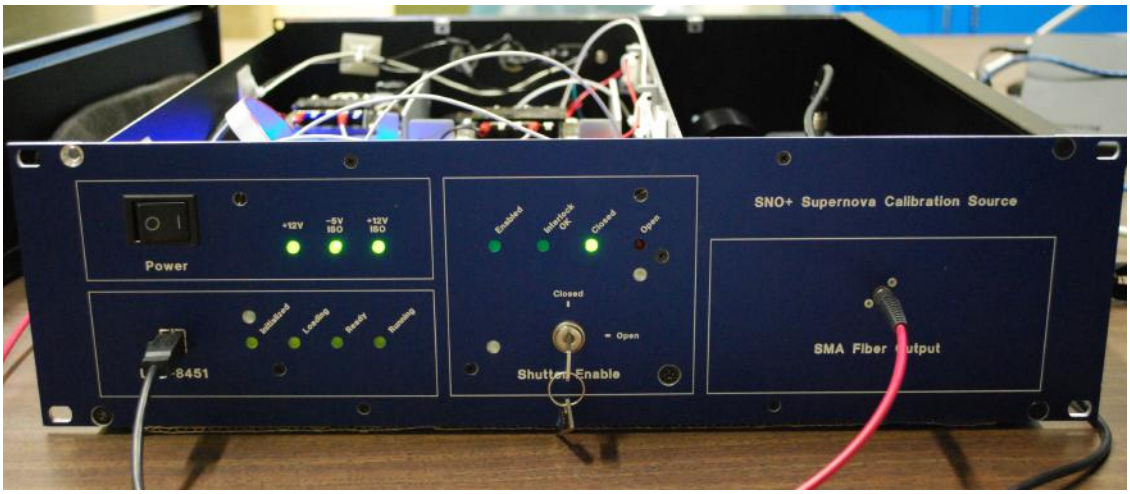

Figure 4.14: The SNC+ chassis shown without the top panel, though the source box is closed when in use.

The SNC+ is operated through a Windows laptop computer, running a LabWindows/CVI user interface (USB-2 communication). The laptop will be mounted within the same rack in the DCR and accessed from the SNO+ control room through VNC.

An overhead view of the SNC+ chassis is seen in Figure 4.14 The custom HSMC DAC daughterboard, developed by J.P. Martin, interfaces the USB board to the Altera FPGA starter board. Signal cables from the DAC daughterboard connect to the laser diode PCB on the back of a heatsink in a partitioned area. Light exiting the heatsink must pass through an electro-mechanical shutter to the second lens tube where the light is focused into a 1mm fiber. An SMA sensor fiber coupler on the front panel signals the front panel PCB whether or not the exterior fiber is attached. This serves as an interlock.

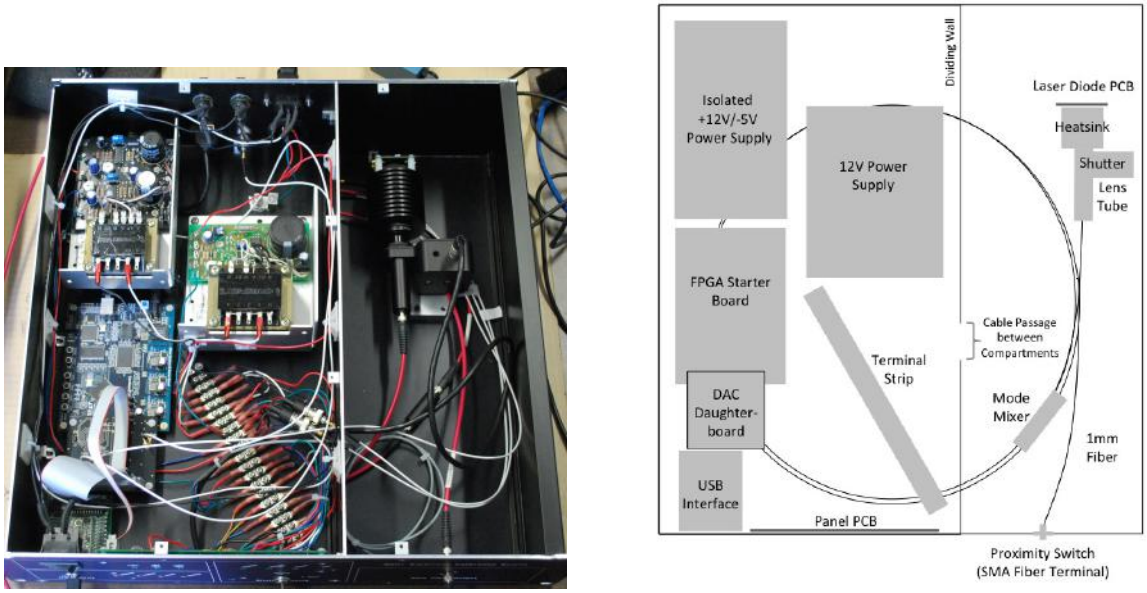

Figure 4.15: Overhead view of the source with the top panel removed. Parts are shown in schematic according to their placement in the photo.

The back panel of the source is shown in Figure 4.16. A tagging "bit" with variable pulse delay and width is sent to the SNO+ Master Trigger Card (MTC) in coincidence with each pulse. The system is powered with 120VAC which is grounded to chassis. The AC 125V (60Hz) is converted into three continuous voltages: +5V ISO, -12V ISO and +12V. An emergency-off cable connector exits the back panel providing for an "emergency-off" mushroom button which will be located in the control room. The emergency-off cable wires are connected to the +12V power supply located inside the chassis. Two fuses protect the +12V and ISO power supplies. The Altera FPGA can be re-programmed with a USB-B port conveniently located on the back panel, and a BNC monitor jack can be used to monitor the signal from the DAC daughterboard on an oscilloscope. All wired components connected to the laser diode PCB are isolated from the chassis with nylon standoffs, with the exception of the USB board front-panel port connection. Electrically isolating the laser diode PCB reduces noise effects caused by ground loops.

Figure 4.16: Back panel view of the source.

4.6.1 Front Panel Indication

The front panel of the system has been designed to control and indicate the state of various system components and is seen in Figure 4.17. Both the power supplies located in the chassis are switched on and off via a power rocker switch on the front panel. There are three LEDs ($+12V, -5VISO$, and $+12VISO$) which can be energized when the designated power supply is turned on. The FIFO loading and SN event run statuses are indicated by 4 more LEDs ($Initialized, Loading, Ready, Running$) next to the USB-8451 board port, which connects to the source laptop. The status of the shutter is indicated by 4 LEDs - *Interlock OK*, *Enabled*, *Closed*, and *Open*. *Interlock OK* turns on when an external fiber is sensed by the SMA Fiber Output adaptor/sensor. The *Enabled* LED turns on when the shutter key is in the *Open* position, as in the shutter leaves are open and light is free to pass through. When the shutter key is in the *Closed* position, the shutter leaves are closed and the *Closed* LED is energized.

Figure 4.17: Indication and control front panel of the SNC+ chassis.

Sitting on nylon standoffs on the back of the front panel is the custom indication and interlock

printed circuit board which houses the LEDs which protrude through holes in the front panel. A photo of one side of the front panel PCB is seen in Figure 4.18; the circuit schematic for this board is located in Appendix C.

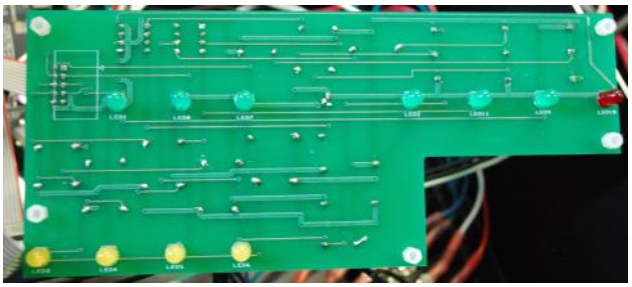

Figure 4.18: The front panel interlock and indication PCB located behind the front panel of the SNC+.

4.7 Personnel and Detector Safety Features

The SNC+ is a relatively closed system that meets the safety requirements of a Class IIIB laser system as outlined in the American Laser Standards Reference Book (ANSI Z136.1, 2007). The shutter interlock system is designed for the safety of both the SNO+ detector and source operator. The shutter is enabled by a physical key switch, and a sensor prohibits the shutter from opening if the fiber is not attached to the fiber connection of the chassis. The main +12V power supply is connected to a normally-closed switch that acts as an emergency off button in the control room. When the switch is opened, the shutter closes, the Altera board powers down, and the FPGA is unable to send a signal to the laser diode PCB. This ensures that the SNC+ cannot remain on with DC current in the SNO+ detector once this button is pressed. The status LEDs located on the front panel give the user indication of the shutter and event statuses.

Chapter 5

SNC+ Commissioning

5.1 Objectives

Benchtop testing of the supernova calibration system with a small PMT was completed following the optical alignment of the SNC+.

The first commissioning objective was to demonstrate proof of principle. The system was tested with parameters that would be used in normal operation to determine whether any major changes would need to be made to the hardware or user interface program.

Several neutral density filters (NDFs) had to be used with the PMT to avoid saturation. *Ex-situ* spectrophotometry measurements were taken to determine the optical densities of the neutral density filters used during commissioning. In normal calibration operations with SNO+, NDFs will not be used, thus the measured optical density factors were removed from the light measurements to correct for attenuation.

During the optical alignment of the system, it was noticed that the laser diode was emitting light at all DAC values, even an idle DAC value of 0. This was due to spontaneous emission occurring at low current, before the onset of stimulated emission. This light output was measured within the SNO+ trigger window to determine whether the SNC+ could be operated without the introduction of too much light into the SNO+ detector.

Another objective was to determine the dynamic range of the SNC+ by sweeping through the idle DAC settings. Data was taken in a series of sweeps for idle DAC values from 0 to values that caused PMT saturation. Different neutral density filters were used in each sweep to vary the PMT

saturation point.

Since different neutral density filters were used to take the idle DAC data, it was of interest to remove their individual optical density factors to find the intensity vs. forward current curve of the diode. This attenuation correction scaled the data to correspond with an optical density factor of 0, as would be the case during normal operation of the SNC+.

To test normal, pulsed operation, the SNC+ was pulsed through the full pulse DAC value range (0-255) sitting at various idle DAC levels that were closer to the threshold for stimulated emission of the laser diode derived from the idle DAC levels scan done previously.

It was of interest to characterize the pulse by determining the maximum light output of a pulse to check light pulse reproducibility and whether a pulse 2.5 ns long was sufficient for our purposes.

5.2 Experimental Setup

The experimental setup for the SNC+ commissioning is depicted in Figure 5.1. Laser diode pulses were generated by the SNC+ and delivered via a 1mm optical fiber, to a Hamamatsu H10721-110 photomultiplier tube. This PMT has a super bialkali photocathode with high sensitivity in the UV-visible range (∼230-700 nm) and a peak sensitivity wavelength of 400 nm. At this wavelength, the radiant sensitivity of the PMT is 110 mA/W on average (at 25°C). The gain of the PMT was controlled by a potentiometer box fabricated according to Hamamatsu's design (box and circuit shown in Appendix C). The PMT was powered with a +5V power supply. The gain of the PMT was adjusted by the turn of a potentiometer and a control readback voltage, related to the PMT gain, was monitored by a voltmeter.

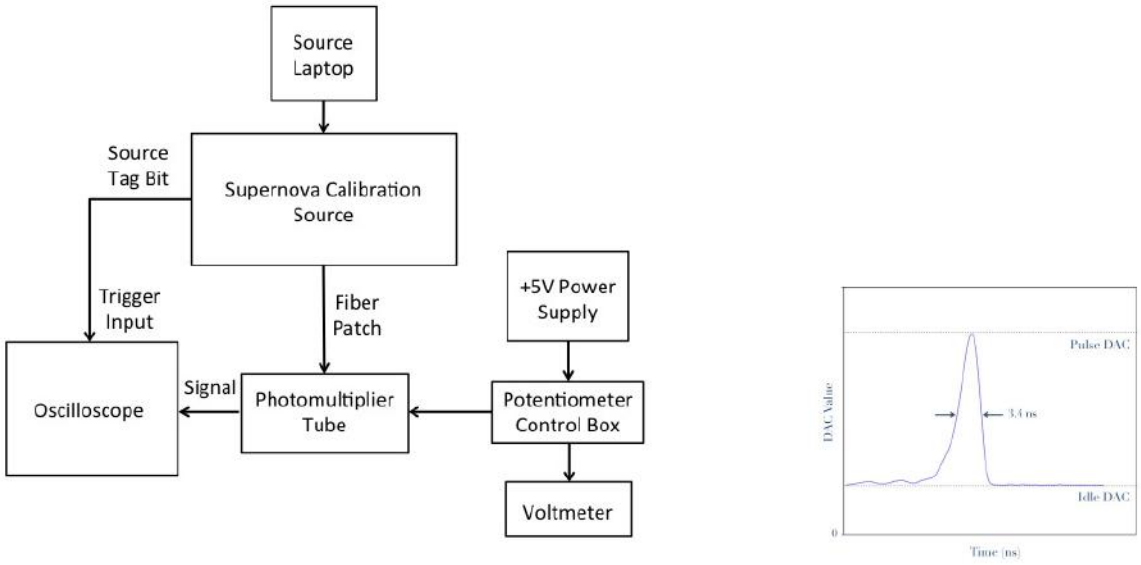

Figure 5.1: **Left**: Diagram of the experimental setup. **Right**: Representation of inverted PMT oscilloscope trace from pulse DAC value = 255.

The signal output of the PMT was connected to a LeCroy WaveRunner 104MXi 1GHz oscilloscope which was used to sample the PMT waveform. The oscilloscope was triggered by the SNC+ tag bit signal. Several neutral density filters, ranging in optical densities from 1.0 - 3.0, were used to reduce the light from the laser diode. The placement of these is seen in Figure 4.11.

5.2.1 PMT Quantum Efficiency and Gain

Part of setting up the experiment involved determining the quantum efficiency (QE) and gain of the PMT based on its specifications. The gain and PMT QE were used in calculations discussed later in the chapter.

The true gain of the Hamamatsu H10721-110 used with the SNC+ was not determined. Instead, the gain from previous studies completed at the University of Sussex and SNOLAB for the TELLIE[1] optical calibration system, using the same PMT model [103], was used. The true SNC+ PMT gain is expected to be similar.

TELLIE used a parameterization of the PMT gain, G, based on the readback voltage, V_{app}:

[1]TELLIE is an external calibration system for SNO+ which uses optical fibers to inject light produced by LEDs into the detector.

$$G = a * e^{b*V_{app}} - c \tag{5.1}$$

where $a, b, c = 2.432,\ 12.86,\ 237.5$ are the measured parameters from the TELLIE PMT calibration [103]. These same parameters were used for the SNC+ PMT along with a readback voltage of +1.000 V for a gain of $G = 9.473e5$.

The quantum efficiency[2] (QE), η, of the PMT was estimated at the laser diode's mean wavelength of 406 nm using the specified cathode radiant sensitivity[3] (S_k) of 110 mA/W at 400 nm. Dividing S_k, expressed in C/J, by the elementary charge, e, one obtains the number of photoelectrons per Joule of incident photons:

$$\frac{S_k}{e} = \frac{110 \times 10^{-3} C/J}{1.6 \times 10^{-19} C/e^-} = 6.875 \times 10^{17} e^-/J \tag{5.2}$$

Taking the inverse of the equation for a single photon energy, E_γ, one obtains the photons per Joule for $\lambda = 406$ nm:

$$\frac{1}{E_\gamma} = \frac{\lambda}{hc} = 2.014 \times 10^{18} \gamma/J \tag{5.3}$$

The ratio of these values is the quantum efficiency of the Hamamatsu H10721-110 PMT which is used in later calculations found in this chapter:

$$\eta = \frac{e^-/J}{\gamma/J} = 34\% \tag{5.4}$$

[2]The quantum efficiency is the number of photoelectrons emitted from the photocathode divided by the number of incident photons.

[3]Radiant sensitivity is the photoelectric current generated by the photocathode divided by the incident radiant flux at a given wavelength, expressed in units of amperes per Watts.

5.3 NDF Absorbance Measurements

The dominant wavelength of the SNC+ laser diode is 406 nm, which is in a region of rapid change of optical density for the neutral density filters. We were interested in calibrating the NDFs using *ex-situ* spectrophotometry measurements to find the true optical density (absorbance) at 406 nm.

Absorbance (optical density, OD)[4] measurements were taken of the NDFs used in the experiment by P. Rost [104] with a spectrophotometer. Figure 5.2 shows the measured absorbance/optical density curves for the NDFs from 380-420 nm. Averages of several values were taken around 406 nm and compared to the manufacturer's nominal OD as seen in Table 5.1. It is clear that at 406 nm, the optical densities are higher than their nominal values, particularly for higher ND values. These measured values (OD_{spec}) were used later in determining the light output of the SNC+ as a function of DAC input values.

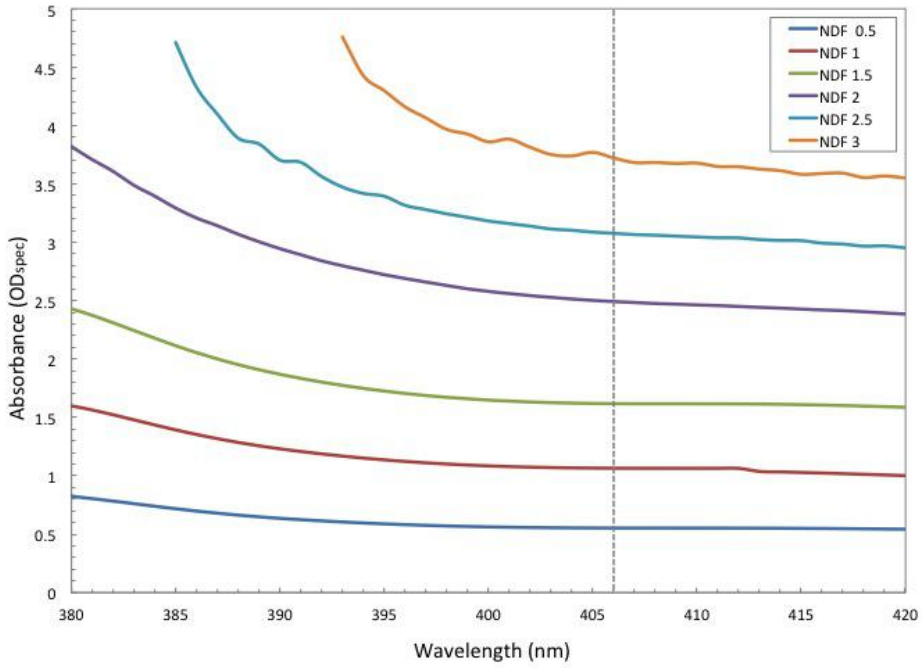

Figure 5.2: The absorbance of the neutral density filters as measured in [104] using a spectrophotometer.

[4]The absorbance of the NDFs used in the experiment, which is synonomous with optical density (OD), is related to the laser diode light transmission T by the following equation: Absorbance = OD = $\log_{10}\left(\frac{1}{T}\right)$.

OD_{man}	OD_{spec}
0.5	0.5533
1.0	1.0673
1.5	1.6203
2.0	2.4976
2.5	3.0509
3.0	3.5649

Table 5.1: The measured optical density values found with a spectrometer (OD_{spec}) compared to the manufacturer's nominal optical density values of the filters (OD_{man}).

5.4 Light Output for a DAC Input of Zero

The smallest current possible through the laser diode is when the system sits at a DAC level of 0. A small amount of light is emitted from the diode when sitting at this DAC level, since spontaneous emission occurs. This diode emission had to be first characterized to determine later whether this light was a tolerable background in SNO+ when the laser diode is operating at the current corresponding to the idle DAC value (in between pulses).

This light output while sitting at a DAC value of 0 was characterized by recording 10,000 oscilloscope traces with a duration of 200 ns. The SNC+ was programmed to send "empty pulses" at 1000 Hz to the PMT. These pulses had a pulse DAC value = 0 and an idle DAC value = 0. Essentially, the smallest possible DC output of the laser diode was being measured by the PMT. The nominal NDF 2 filter was used which reduced the laser diode light amplitude by a factor of $10^{2.4976} = 314.49$ (Table 5.1). The NDF's optical density reduction factor was later removed from the light signal to give the true value of the light from the laser diode[5].

The oscilloscope was set to a fixed vertical gain of 500 mV/div and a timebase of 20 ns/div. Trace files were saved containing time and voltage data. A sampling rate of 5 GS/s and a sampling time period of t = 200 ns gave a total number of individual voltage points (V_i) measured per trace of $N = 5$ GS/s $\times$ 200 ns = 1000 pt/trace.

[5]In hindsight, this measurement could have been made without an NDF present.

The mean of voltage points taken from one trace was found using:

$$V_j = \sum_{i=1}^{N} \frac{V_i}{N} \tag{5.5}$$

where $N = 1000$. The mean voltage for multiple traces, $\bar{V}$, was found using:

$$\bar{V} = \sum_{j=1}^{T} \frac{V_j}{T} \tag{5.6}$$

where T is the total number of traces.

The area under each trace was determined by integrating the trace voltage levels (V_i) in a chosen time interval (t_1, t_2):

$$A_j = \int_{t_1}^{t_2} V_i(t)dt \tag{5.7}$$

where $dt = 0.2$ ns for a full time period of $t = 200$ ns. The mean area under all these traces $\bar{A}$ in a sampling time t is:

$$\bar{A} = \frac{\sum_{j=1}^{T} A_j}{T} \tag{5.8}$$

The mean area of the traces, $\bar{A}$, was used to calculate the photon count for a period of 200 ns from the laser diode pulse, N_γ, based on the following equation:

$$N_\gamma = \frac{|\bar{A}|(10^{OD_{spec}})}{eZG\eta} \tag{5.9}$$

where $|\bar{A}|$ is the absolute value of the mean area of the traces, $Z = 50\ \Omega$ is the input impedence input of the oscilloscope, OD_{spec} is the measured optical density factor from the neutral density filter used (further described in Section 5.6), e is the elementary electric charge, η is the PMT

quantum efficiency calculated using Equation 5.4 (34%), and G is the gain of the PMT (947,300).

The individual voltage points, V_i, for 10,100 oscilloscope traces (1.013e7 entries), are plotted in the histogram seen in Figure 5.3. The mean trace voltage of the spontaneous emission was calculated from T = 10,100 traces of the oscilloscope in t=200 ns periods using Equation 5.6. The mean trace voltage was found to be $\bar{V}$ = (-5.278±0.004)e-4 V.

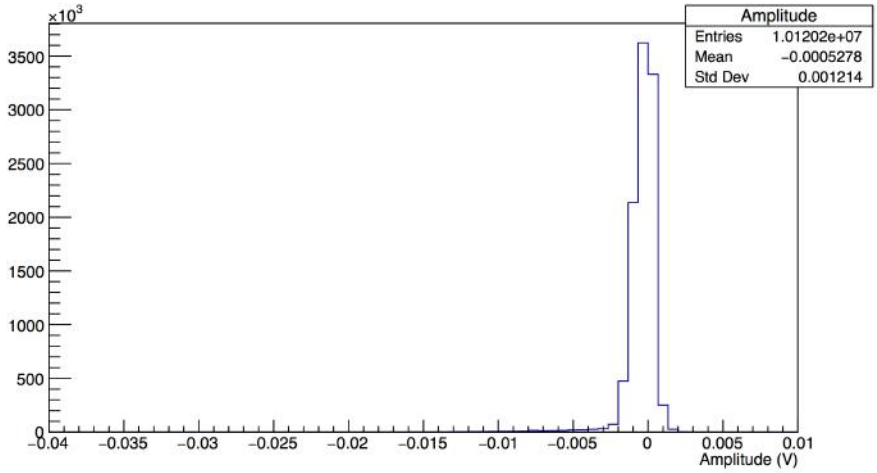

Figure 5.3: Histogram of the voltage points, V_i, for 10,100 traces at 1000 samples per trace for a DAC input of 0. The mean trace voltage is $\bar{V}$ = (-5.278±0.004)e-4 V.

The histogram of the individual trace areas per 200 ns is shown in Figure 5.4(a) for T=10,100 traces. The centroid depicts the mean area (trace height or amplitude) which is calculated using Equation 5.8 to be $\bar{A}$=(-0.1052±0.0003) Vns integrated over 200 ns.

Equation 5.9 was then used to calculate the average photon count expected from this signal: N_γ = (1.294±0.004)e4 photons/200 ns. The multiplicative optical density factor of $10^{2.4976}$ was included to account for the NDF 2 filter's light reduction and give the photon count produced when no filter is present. The photon count distribution is shown in Figure 5.4(b), which is derived from the area distribution in Figure 5.4(a).

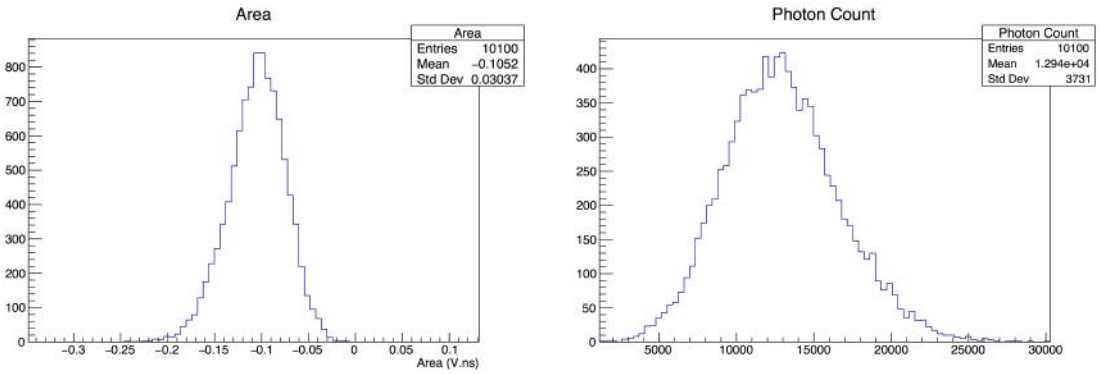

Figure 5.4: (a) **Area**: The areas under the oscilloscope traces for a DAC input of 0 for over 10,000 traces integrated over 200 ns. **Photon Count**: The photon counts found from the mean areas of 10,100 traces integrated over 200 ns using Equation 5.9. This is the light present in 200 ns for a DAC input of 0.

To determine whether this photon output in 200 ns is a tolerable light background in SNO+ in between laser diode pulses, we consider the anticipated SNO+ trigger threshold. The SNO+ energy threshold is likely to be $\geqslant$150 keV in a 100 ns window to be above the background due to ^{14}C β-decay[6] For a light yield of 400 p.e. per MeV, 150 keV is equivalent to 60 p.e. The SNC+ light output at a DAC value of 0 should be well below this; for example, 25% of 60 p.e., $\sim$15 p.e., could be reasonable. Considering 99.39% external transmission loss (see Table 4.1) from the SNC+ to the SNO+ PMTs, this allows for $\sim$1,491 p.e. in 100 ns. This calculation is seen in Equation 5.10:

$$\Big(150keV\Big)\Big(\frac{1MeV}{1000keV}\Big)\Big(\frac{400p.e.}{1MeV}\Big)\Big(0.25\Big)\Big(99.39\Big) = 1491p.e./100ns \tag{5.10}$$

From Figure 5.4(b), in 100ns, the SNC+ produces $N_\gamma = 6470\pm20$ photons when sitting at a DAC value of 0, which is higher than the SNO+ photoelectron trigger threshold by over $4\times$ $(\frac{6{,}470p.e.}{1491p.e.})$. This will have to be addressed in future modifications of the system to reject the light from the diode before it undergoes stimulated emission.

[6] ^{14}C is a β emitter that is constantly reproduced through cosmogenic neutron interactions. Because the decays occur frequently, it is considered a constant background or noise for SNO+.

5.5 DAC Levels Scan

Considering that a DAC level of 0 was beyond the tolerance of SNO+, sitting at higher levels between pulsing was not feasible. It was originally intended that the DAC input value be kept at a non-zero level just below stimulated emission, in between laser pulses, to reduce the voltage slew time of the circuit and allow for maximum light production during pulsing, but this "idle" DAC input value had to be tolerable in SNO+ as a constant (DC) photon background. A measurement of the photon output as a function of DAC input value had been made (prior to discovering that a DAC value of 0 was beyond SNO+ tolerance) to determine this stimulated emission threshold as a DAC input value.

Several sweeps through a range of DAC values were made with different combinations of ND filters, by using the idle DAC setting of the SNC+. Traces were recorded for 500 ns time windows with the oscilloscope triggered by the SNC+ tag bit to determine the light produced by the diode when not sending a pulse signal into the detector. These idle DAC sweeps were taken with each ND filter combination (OD: 1.0 - 3.0) in steps of 0.5.

As mentioned in Chapter 4, each DAC input value corresponds to a current value through the diode. The 16-bit DAC input value can range from 0 to max of 65,280 which corresponds to maximum applied current. Keeping the laser diode at high current levels over an idle DAC value of 30,000 for long periods of time can cause damage to the device. Thus, sweeps were kept between the idle DAC values of 0-30,000. The mean area under the idle DAC traces over 500 ns was found using Equations 1.5-1.8 with N = 5 GS/s $\times$ 500 ns = 2500 pt/trace and a time period of 500 ns.

Figure 5.5 shows the absolute value of the mean areas for the traces as a function of the DAC input value, starting at 0. The mean trace areas are integrated over 500 ns. Neutral density filters of varying optical density were used.

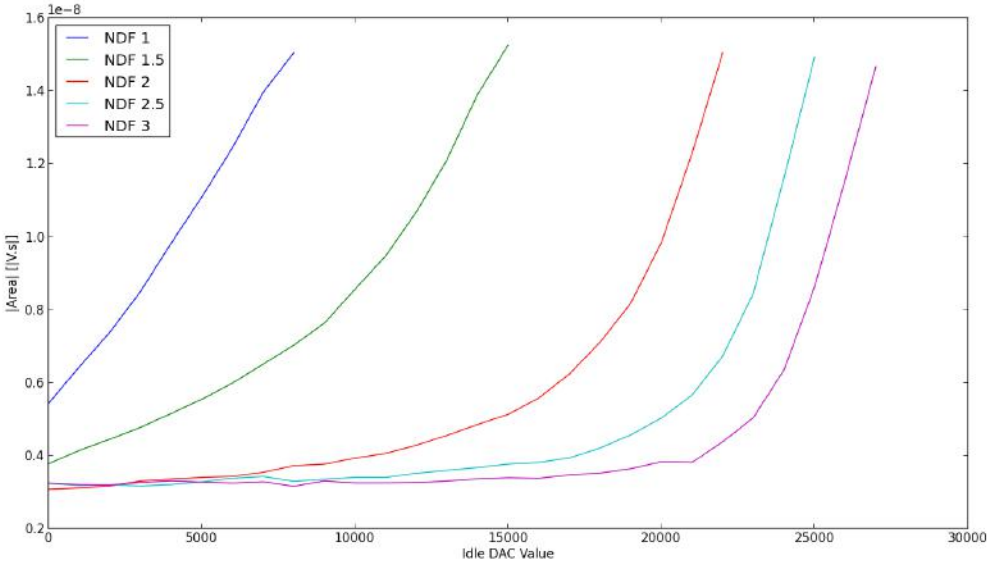

Figure 5.5: The mean trace areas (absolute value) integrated over 500 ns vs. the idle DAC value. Sweeps through all idle DAC input values were taken with several neutral density filters of varying optical density (NDFs 1, 1.5, 2, 2.5, 3). Each area point (not shown) is an average from several thousand traces. The PMT saturation occurred around 1.5×10^{-8} Vs and was omitted from the plot.

The PMT eventually saturates with too much light at some level extending beyond the endpoints of the curves; these saturated portions have been cut from the plot. The magnitude of the mean trace areas increases with DAC input value, which is expected.

Ideally, no light should be present before the stimulated emission threshold, but the non-negligible area prior to stimulated emission (differing for each curve) is attributed to spontaneous emission of the diode. Moving to higher NDF curves of 2.5 and 3, we begin to see the true nature of the laser diodes power/luminosity output vs. the current or DAC value applied.

To correct for varying attenuation of the NDFs and find a rough threshold current/idle DAC level of stimulated emission, curves were combined by removing the optical density factors from the area points.

5.6 Attenuation Correction of the Data

When the area values are corrected for the measured optical densities, the idle DAC sweeps in Figure 5.5 should fall on each other. This unified curve corresponds to an optical density of OD=0,

ie. the absence of NDFs, as would be the case during normal operation of the SNC+.

As is evident in Figure 5.5, the idle DAC sweep data contain DC offsets that need to be removed before the signal attenuation, due to the presence of ND filters. The origin of these offsets in the data was never fully understood, but it is clear that they must be removed. The measured optical densities were used to calculate the scaling correction factor. The offsets were found by either taking the average of a number of the low idle DAC value areas, in the case of the high optical density sweeps, or by finding the offset value that produced the best overlap of the curves for the low optical density sweeps.

The scaled curves are shown in Figure 5.6. The scaled areas, A_{scaled}, are determined using:

$$A_{scaled} = (A_{raw} - A_{offset}) \times 10^{OD_{spec}} \tag{5.11}$$

where A_{raw} is the original area, A_{offset} is the offset value, OD_{spec} is the measured optical density.

The offset values used in Equation B.1 are given in Table 5.1 along with the nominal and measured OD values at 406 nm.

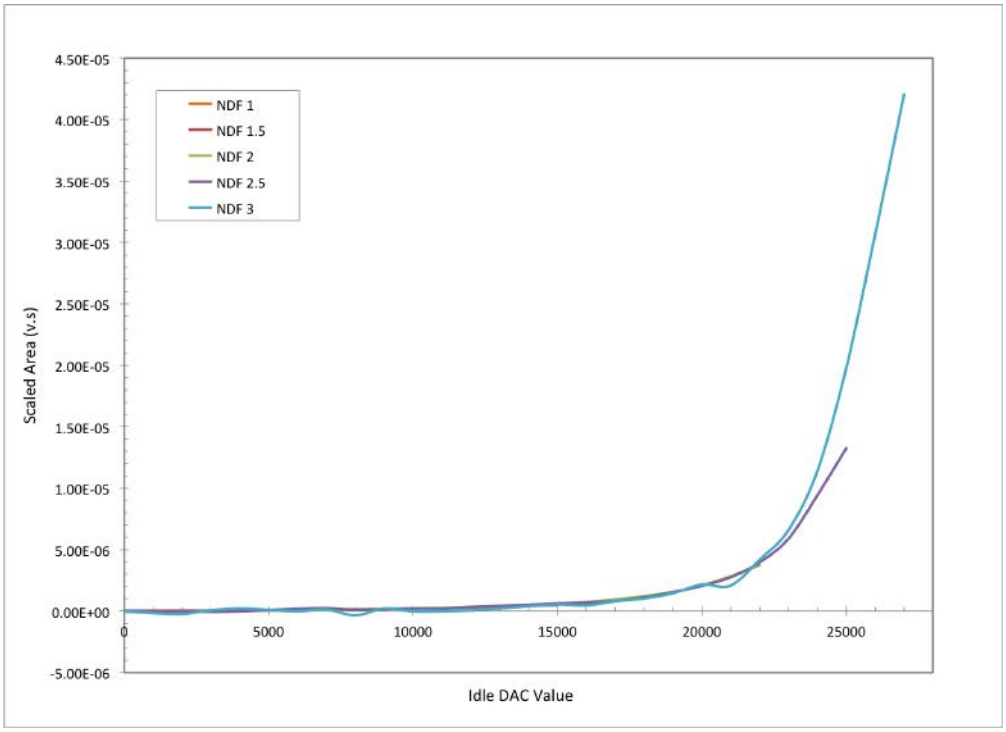

Figure 5.6: Scaled area values for all idle DAC curves with ND filter optical densities and offsets removed. The discrepancy at idle DAC = 21,000 between the NDF 2.5 and 3.0 curves is due to a bad data point. The discrepancy between the same curves for idle DAC values > 22,000 may be due to PMT saturation in the NDF 2.5 curve.

OD_{man}	OD_{spec}	A_{offset}
1.0	1.0673	5e-9
1.5	1.6203	3.7e-9
2.0	2.4976	3.25e-9
2.5	3.0509	3.22e-9
3.0	3.5649	3.25e-9

Table 5.2: Parameters used to correct for the attenuation introduced by the use of ND filters. OD_{man} is the manufacturer's nominal optical density of the ND filter combination at 406 nm. OD_{spec} is the measured optical density at 406 nm. A_{offset} is the offset that was removed before correcting the idle DAC sweep curves.

Corrected in this way, Figure 5.6 resembles and now may be directly compared to the laser diode optical output versus forward current characteristic (Figure 4.6). The DAC input value at which stimulated emission of the laser diode occurs may be found by extrapolation of the 3rd last

and last points measured in the scaled NDF 3 idle sweep. These two points were (x_{k-1} = 25,000, A_{k-1} = 1.98e-5) and (x_k=27,000, A_k = 4.2e-5), where x represents the idle DAC value and A represents the mean area at x. These points were used in a linear extrapolation down to threshold idle DAC. The extrapolation equation used to find the mean scaled area of the traces at various idle DAC values ($A_{scaled}(x^*)$) was:

$$A_{scaled}(x*) = A_{k-1} + (\frac{A_k - A_{k-1}}{x_k - x_{k-1}})(x * -x_{k-1}) \tag{5.12}$$

where $x*$ is the idle DAC value at which the area is being found.

Extrapolating to the point at which $A_{scaled} = 0$ produces the idle DAC threshold value. The intercept of the linear extrapolation was x^*_{th} = 23,216. This DAC value represents the point where stimulated emission in the laser diode begins. Furthermore, extrapolating to a maximum idle DAC level of x^*_{max} = 65,280 produces a scaled trace area estimate of $\mathrm{A}_{scaled}(x^*)$ = 4.7e-4 Vs.

Recalling Figure 4.6, the required forward current corresponding to maximum possible pulse power output of the diode (P = 250 mW) was $\mathrm{I}_{F,max}$ = 188.416 mA $\simeq$ 188 mA. The forward current corresponding to threshold was I_{th} $\simeq$36 mA. If the experimental threshold idle DAC value (x^*_{th} = 23,216) now corresponds to a current threshold of I_{th} $\simeq$36 mA, then the current being reached at maximum idle DAC value (x^*_{max} = 65,280) is only $I_{max,true} = \frac{36mA \times 65{,}280}{23{,}216}$ = 101.226 mA $\simeq$ 101 mA $<$ 188 mA.

Therefore, to reach the desired maximum current, the gain (current/DAC value) needs to be increased by $\sim$87%. This would be accomplished by a hardware change to the LD driving PCB, possibly by addition of a second op-amp. Other adjustments to the system may be required to extend the power output of the laser diode and these are discussed in Chapter 6: Conclusions.

5.7 Testing of Normal, Pulsed Operation

5.7.1 Pulsing from Threshold Idle DAC Levels

An idle DAC level of 20,000 was tested for its tolerability in SNO+ as a background light when the laser diode is not pulsing. This value was chosen since it sits below below threshold idle DAC value of x^*_{th} = 23,216, and would be a level the DAC would sit at between pulses for normal operation

(had a DAC level of 0 not been already intolerable as a background light source in SNO+).

The 20,000 idle DAC traces were characterized before pulsing from this level. From the 20,000 or 20k idle DAC level, several thousand traces were averaged to find the mean voltage within t=500 ns as seen in Figure 5.7 ("*Amplitude*", ie. Trace Height), which was $|\bar{V}|$ = (1.9710±0.0006)e-2 V.

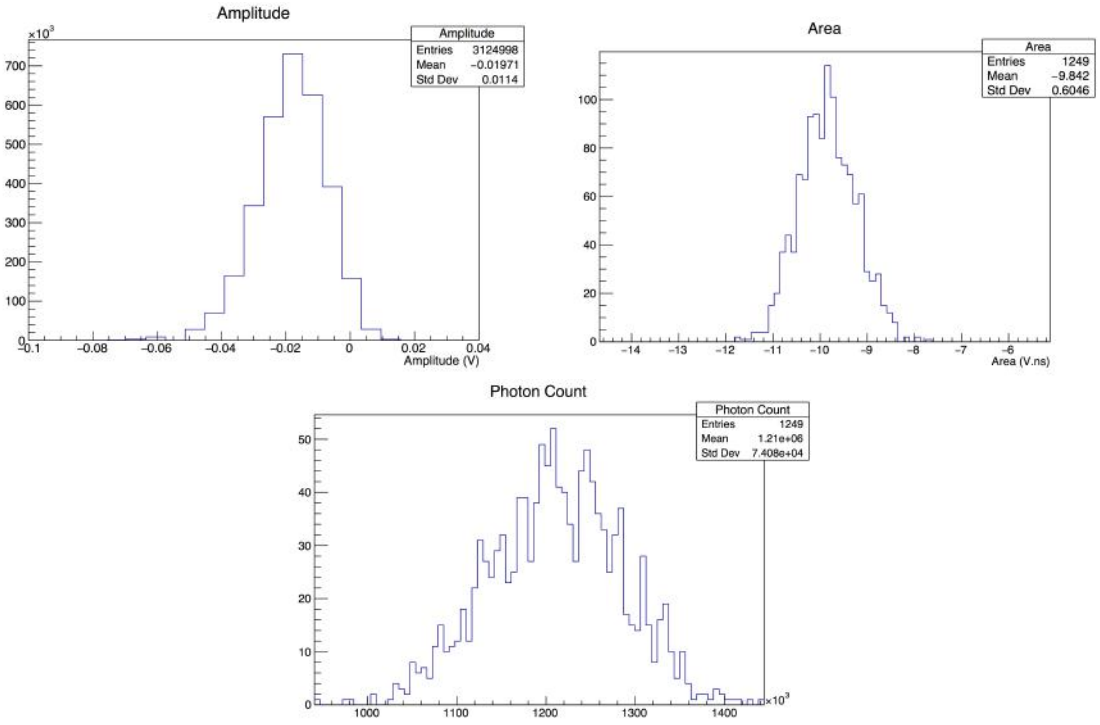

Figure 5.7: Histograms for the 20,000 idle DAC level taken with NDF 2. (a) **Amplitude**: The voltage distribution for several thousand traces using NDF 2 sitting at an idle DAC level of 20,000. The absolute value of the mean voltage at this level is $|\bar{V}|$ = (1.9710±0.0006)e-2 V. (b) **Area**: The distribution of the areas that can be calculated from (a) in a period of 500 ns are shown. The absolute value of the mean area (scaled, ie. with the NDF 2 optical density factor removed) is $|\bar{A}_{scaled}|$ = (9.84±0.02) Vns. (c) **Photon Count**: The photon count is calculating using the trace areas and Equation 5.9 . The mean photon value, $\bar{N}_\gamma$ = (1.210±0.002)e6 γ, is an estimation of the light present in a time period of 500 ns from the laser diode when set to an idle DAC of 20,000 between pulses.

The area and photon distributions are also seen in Figure 5.7. The area of the idle DAC level averages to $|\bar{A}_{scaled}|$ = (9.84±0.02) Vns. To estimate the photon production at that level, the area mean was used with Equation 5.9 to find N_γ = (1.210±0.002)e6 γ.

As previously mentioned, the tolerance of SNO+ is 150 keV in 100 ns which corresponds to 1,491 p.e. from the SNC+ before external transmission losses. The 20,000 idle DAC level photon output was measured within a timespan of 500 ns, so the resulting value can be reduced by a factor

of 5 to obtain $N_\gamma = (2.420 \pm 0.004)$e5 γ which is well above the allowable 1,491 p.e./100 ns in SNO+.

The system is currently not capable of sitting at a level below this maximum at any idle DAC value between 0-65,280 due to the spontaneous emission of the system below lasing which starts at an area of ∼0.3e-8 Vs.

5.7.2 Pulse Characterization

The laser diode was pulsed as it would be during normal operation: from a non-zero idle DAC level sitting under stimulated emission threshold. 20,000 was chosen for the idle DAC level since this sits below idle DAC threshold/stimulated emission ($x^*_{th} = 23{,}216$). Maximum DAC amplitude pulses were used to determine the current light output and reproducibility of the pulse. The pulse DAC value is used to describe the pulse power and can range between 0-255. It corresponds to the idle DAC level through the relationship: *Idle DAC Value* = 256 × *(Pulse DAC Value)*. The light produced by the diode at a pulse DAC value of 255 in a 2.5 ns period should be equivalent to the light produced at an idle DAC level of max 65,280 in a 2.5 ns period.

The average waveform of a pulse is seen in Figure 5.8 for an idle DAC level of 20,000 with NDF 2. This pulse is an average of several thousand pulse waveforms pulsed at a frequency of 1000 Hz[7]. The pulse has a FWHM of roughly 3.4 ns.

[7]To determine whether or not the frequency of the pulse affected the waveform, tests were performed and described in Appendix B. The oscilloscope appeared to perform better at lower frequencies, but anything over 10,000 Hz lost data. It was efficient to perform tests at 1000 Hz, ensuring full data acquisition with no losses.

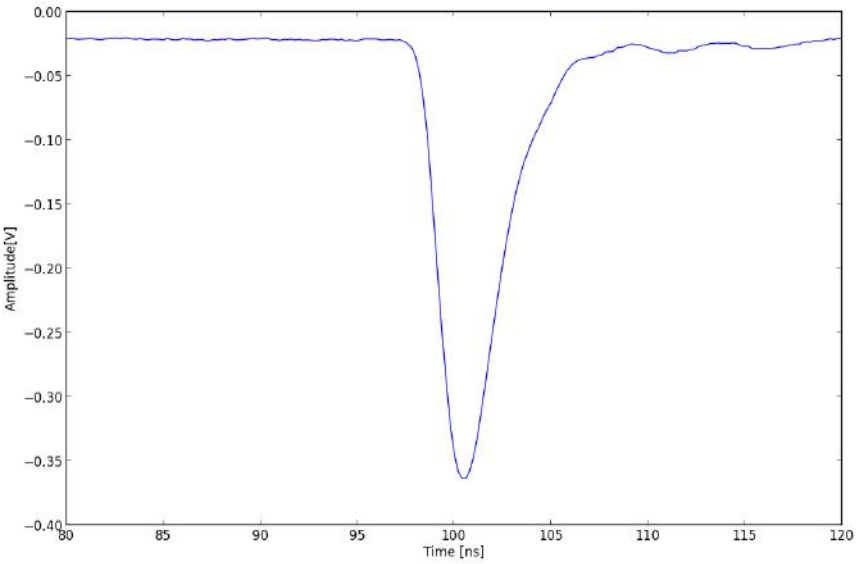

Figure 5.8: Mean waveform for pulse of maximum DAC value = 255; zoomed into cut region 95-110 ns (15 ns period). Data taken with NDF 2 sitting at an idle DAC = 20,000. Pulse FWHM is roughly 3.4 ns.

A cut region was applied between 95-110 ns where the pulse was triggered. A background subtraction from the cut region was used to determine the area under the pulse. The background voltage level per trace was estimated by averaging the first 100 data points of the waveform before the pulse at 95 ns using:

$$\bar{V}_{j,bkgd} = \sum_{i=1}^{N} \frac{V_i}{N} \tag{5.13}$$

where $N = 100$ and j = trace number. This background mean includes the spontaneous emission at the voltage level of the idle DAC value = 20,000.

To find the background-subtracted ("cut") pulse area in 95-110 ns for one trace, $\bar{V}_{j,bkgd}$ was subtracted from each voltage point, $V_{i,pulse}$, of the pulse:

$$\begin{aligned} A_{pulse,cut} &= \int_{t=95ns}^{110ns} \left[V_{i,pulse}(t) - \bar{V}_{j,bkgd}\right] dt \\ &= \int_{t=95ns}^{110ns} V_{i,pulse}(t) dt - \bar{V}_{j,bkgd}(15ns) \end{aligned} \tag{5.14}$$

The mean area for several thousand traces was then found using:

$$\bar{A}_{pulse,cut} = \frac{\sum_{j=1}^{T} A_{pulse,cut}}{T} \tag{5.15}$$

where j is the trace number from 1 to T.

Figure 5.9 shows the amplitude/voltage level histogram created from a maximum amplitude pulse DAC value = 255 originating from an idle DAC level = 20,000. The "Amplitude" histogram displays the trace voltages of the pulse points without the background subtraction of the idle DAC level. The optical reduction factor of the NDF 2 has been removed. The absolute value of the mean of the pulse voltage within the 15 ns region is $|\bar{V}|$= (114.6±0.4)V before background subtraction.

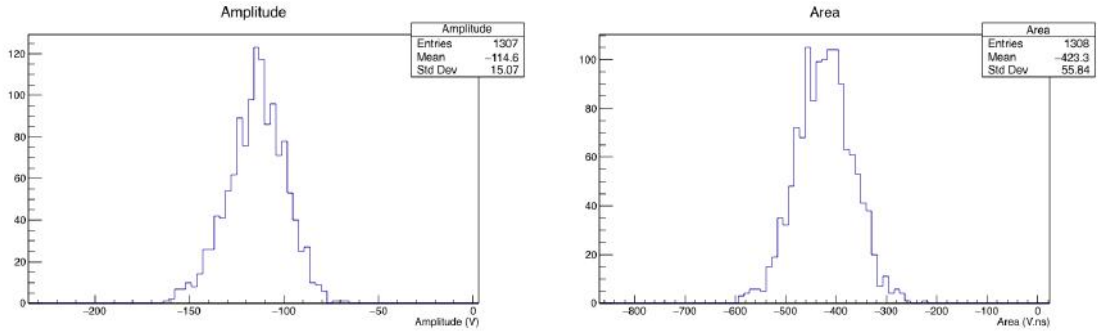

Figure 5.9: Histograms for a laser diode pulse of maximum amplitude (pulse DAC value = 255) for an idle DAC level of 20,000 below threshold. Pulse was background subtracted around 95-110 ns (15 ns). Over 1000 waveforms were taken with NDF 2 at this DAC amplitude. (a) **Amplitude**: The maximum pulse height/voltage distribution. The mean voltage value is $|\bar{V}|$= (114.6±0.4) V. (b) **Area**: Area under the pulse between 95-110 ns with a background subtraction of the underlying idle DAC level at 20,000 averaged from the first 100 points of the waveform in the idle background. The absolute value of the mean area (with attenuation correction) is $\bar{A}_{scaled}$ = (423±2) Vns.

The area histogram in Figure 5.9(b) shows the distribution of trace areas which were calculated from Equation 5.14. The absolute value of the mean area (with attenuation correction) is $\bar{A}_{scaled}$ = (423±2) Vns. Using Equation 5.10, a photon count was calculated from the mean area to be N_γ = (1.2±0.2)× 10^5. This light production is much lower than what is expected from a maximum pulse of 255 for this level which leads to the conclusion that the pulse is not reaching its maximum expected height. It was found in Chapter 4 that the maximum DAC value of 255 is not normalized to the maximum laser diode output power of ∼250 mW and instead corresponds to a power output of P = 1.64(101.62) - 59 = 107.66 mW which is ∼43% of the desired 250 mW. The cause for

this power loss is the inability of the pulse to reach maximum within the short timescale of 2.5 ns. Several other factors could influence the overall reduction in light output measured from the diode, such as inefficient pulse output, including inadequacy of a single op-amp, clock misalignment, misalignment of the optical system, etc., but these would also affect the idle DAC levels (which perform adequately) along with the pulse DAC light levels, and so are not the reason for the pulse alone not reaching maximum power.

Sweeps through the pulse DAC values (0-255) were taken to characterize the pulse shape and light output. Three idle DAC levels were used with NDF 2: 15,000, 17,500, and 20,000, which are all levels below the stimulated emission threshold. The pulses were background subtracted between 95-110 ns using the average of the first 100 points from the idle DAC traces (outside the pulse region) with Equations 5.13 and 5.14. The mean subtracted pulse areas (with attenuation correction) are plotted in Figure 5.10 (Top). The pulse areas shown are the absolute values and decrease with idle DAC value. Figure 5.10 (Bottom) shows the zoomed region of DAC value 0-110 where the curves cross the 0-axis of the area. The point at which the curves cross 0 indicates the point at which the pulse begins to appear with a non-zero area above the idle DAC level.

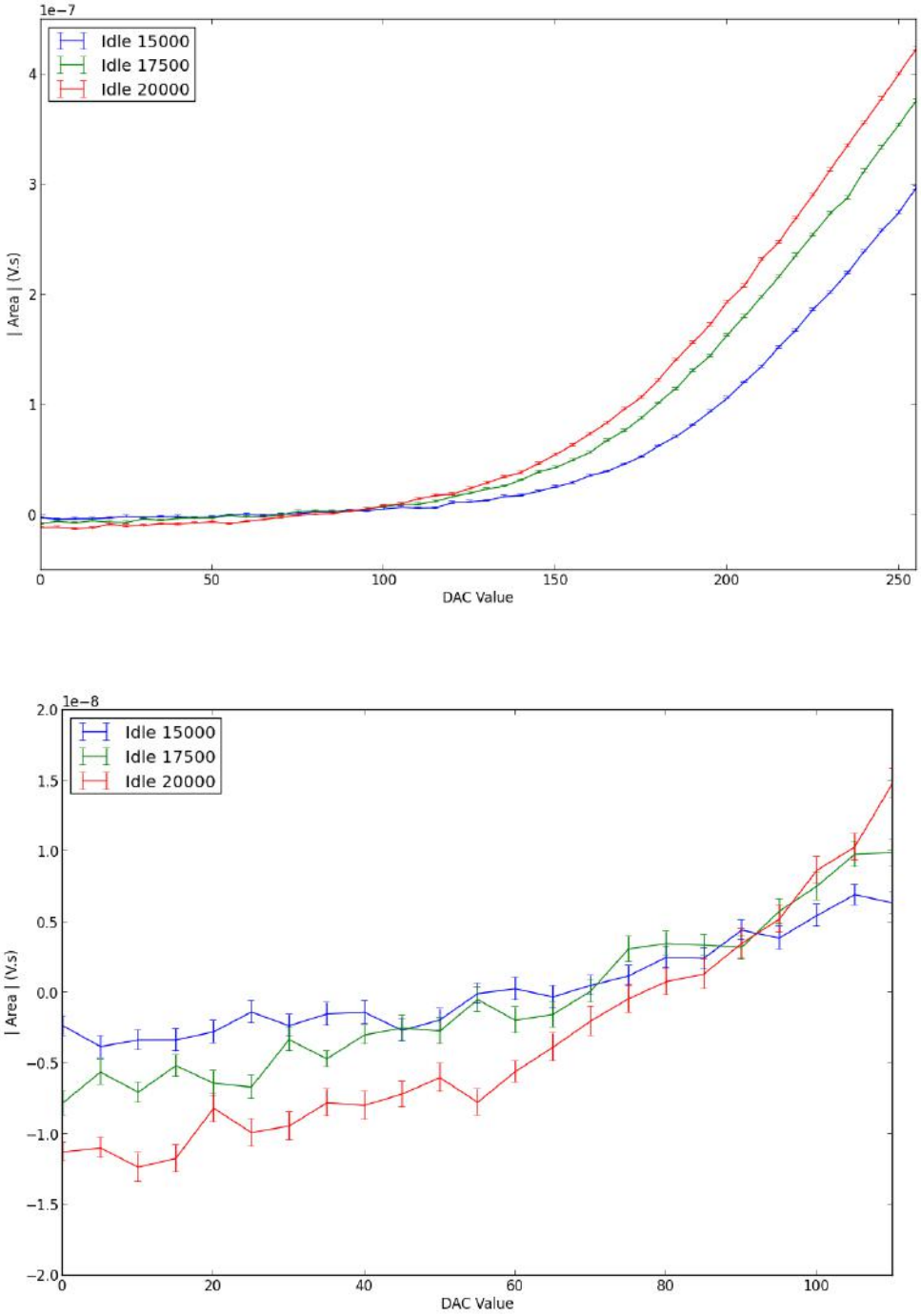

Figure 5.10: **Top**: Mean area of the pulse taken between 95-110 ns with a backgroun subtracted for 3 idle dac levels (15k, 17.5k, and 20k) sweeping through 0-255 DAC amplitudes. **Bottom**: Closer view of the pulse areas pulsing from a 0-110 Idle DAC value showing the crossing of all curves at the Area = 0 axis.

5.7.3 Pulse Reproducibility

It is important to check that the pulse is reproducible during running to ensure the device is working properly and all data is being transferred with the appropriate clock timing of the FPGA. The reproducibility of the pulses was determined by finding the full-width-half-max (FWHM) of the pulse area histograms for each trace in 95-110 ns (with the background idle DAC levels cut) and dividing by their mean area. The FWHM was determined using the following equation:

$$FWHM = 2\sqrt{2\ln 2}\sigma \tag{5.16}$$

Shown in Figure 5.11 are the FWHM/Mean Area of the pulses from DAC values 120-255 for the three idle dac levels of 15k, 17.5k, and 20k. These curves give an estimation of the pulse height reproducibility from three different idle DAC values sitting under threshold. The curves decrease with increasing area and level off towards 0, demonstrating that the pulse area becomes more reproducible at higher DAC values.

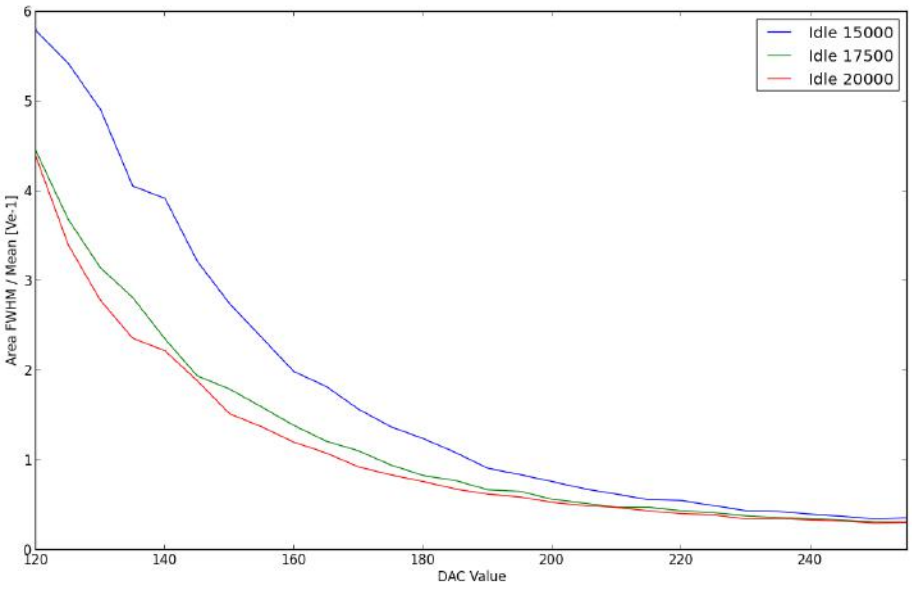

Figure 5.11: FWHM of the individual trace pulse areas over the mean pulse areas taken between 95-110 ns with a background cut for three idle DAC levels, sweeping through DAC values = 120-255.

5.7.4 Pulse Efficiency

The area of the pulse produced at pulse DAC value of 255 in 2.5 ns was found to be a small percentage of the area of a square pulse of DAC value 65,280 in 2.5 ns. Figure 5.12 shows the discrepancy between the experimental area of the pulse, A_{pulse} vs. the "ideal" area, A_{ideal}, of the square pulse in 2.5 ns.

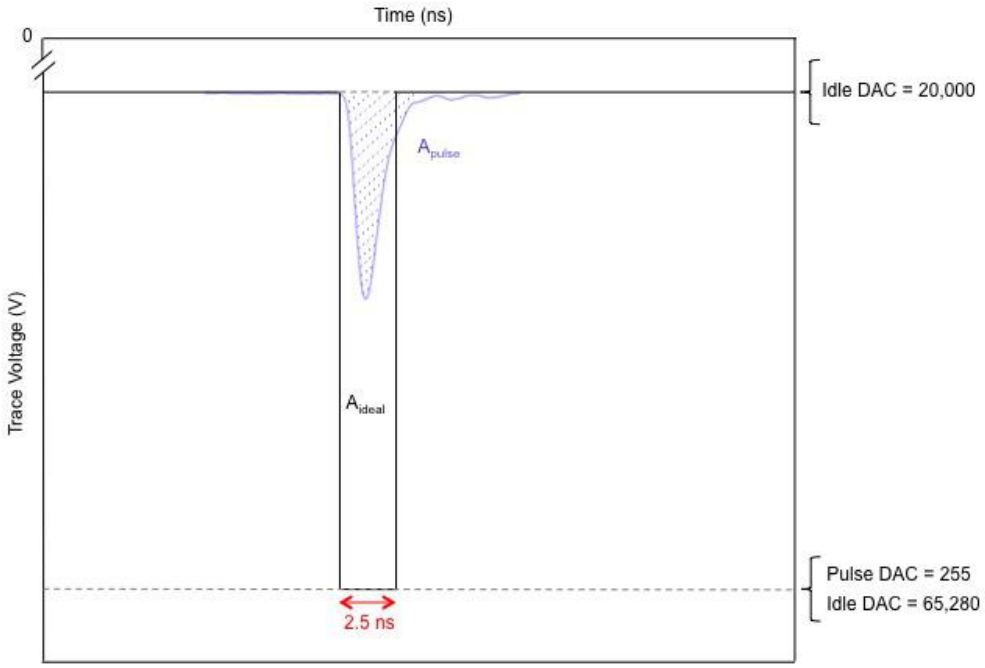

Figure 5.12: The pulse efficiency for a 2.5 ns pulse of maximum DAC value (255) from an idle DAC level of 20,000. The area under the pulse within a 2.5 ns period is labeled A_{pulse}. This is compared to the area of a square pulse reaching maximum voltage for a DAC value of 65,280 in 2.5 ns: A_{ideal} which was found using Equation 5.17.

To obtain the area of the square pulse of maximum DAC value 65,280 (equivalent to pulse DAC value 255), Equation 5.12 was first used to find the area of the idle DAC level at 65,280 in a 500 ns period, $A_{scaled,65280}$ = 4.669e-4 Vs.

Subtracting the value of the area in 500 ns at an idle DAC level of 20,000 from this, $\bar{A}_{20,000}$ = (9.84±0.02)e-9 Vs, obtained from Figure 5.7(b) and multiplying by $\frac{2.5ns}{500ns}$, we obtain the area of the square pulse of with idle DAC background subtraction in 2.5 ns, A_{ideal}:

$$A_{ideal} = (A_{65280} - A_{20,000})(\frac{2.5ns}{500ns}) = 2.334 \times 10^{-6} Vs \tag{5.17}$$

This is compared to the area of the experimental pulse obtained from Figure 5.9(b), $\bar{A}_{scaled} = A_{pulse} = (423 \pm 2)$ Vns. This is a background-subtracted value which roughly gives the area under the pulse in 2.5 ns. The pulse efficiency of the maximum 255 DAC level pulse from 20,000 in comparison to the ideal square pulse in a period of 2.5 ns is then found to be roughly 18% of the expected value:

$$Efficiency = \left(\frac{A_{pulse}}{A_{ideal}}\right) \times 100\% = \left(\frac{4.23 \times 10^{-7} Vs}{2.334 \times 10^{-6} Vs}\right) \times 100\% \simeq 18\% \tag{5.18}$$

This means that the power output of the diode will need to be increased to reach efficiencies closer to 100%.

Chapter 6

Conclusions

6.1 Proofs of Principle

The commissioning of the SNC+ provided a successful proof of principle as it did perform well in its basic capacity as a programmable, optical pulser with a working user interface. The SNC+ can produce the minimum pulse-to-pulse timing separation to produce realistic event pile-up in the SNO+ 500 ns trigger window. The UI is able to load any file wherein the pulse timing and energies can be directly modeled after expected supernova energy distributions for a more realistic calibration. Several files were loaded containing random energy and timing values during preliminary testing, and the SNC+ was able to execute these. Several other tests were performed on the frequency dependence of the pulse, and the results (Appendix B) show no significant dependence up to 1 MHz. The safety interlock system of the SNC+ also performs correctly and should ensure the safety of the SNO+ detector and calibration personnel.

The SNC+ currently does not produce a sufficient amount of light in a 2.5 ns pulse to simulate a real supernova neutrino physics event, and does not have a dynamic range of 0-60 MeV to accommodate the energy range of supernova neutrino emission. Thus, it cannot currently simulate supernovae as close as 0.5 kpc. Solutions to this issue are discussed in Section 6.2.

6.2 SNO+ Tolerance of Spontaneous Emission

It was determined that the laser diode does produce light by spontaneous emission prior to stimulated emission even at a DAC value of 0. This light emission at a DAC value of 0 was analyzed as a possible allowable light background in the SNO+ detector. It was determined that within SNO+'s 500 ns trigger window, this would not be an acceptable background light source between pulses, and this needs to be addressed. The laser is not currently able to sit an any idle DAC value greater than or equal to 0 below stimulated emission threshold. The SNO+ trigger NHit will have to be changed temporarily during calibration such that the photon tolerability is higher to accommodate the spontaneous emission.

6.3 Pulse Efficiency

It was found during testing that the pulse is not reaching its maximum power output in a 2.5 ns pulse when sitting at an idle DAC level just below lasing threshold. The amplitude of the pulse should start from the current level of the idle DAC before pulsing - ie. the amplitude does not drop back to 0 prior to pulsing. This means that the pulse DAC amplitude maximum of 255 (not cutting out idle DAC level background) should produce a pulse up to the light level of the maximum idle DAC at 65,280. This is however not the case as found in Chapter 5.7.4, and the pulse area is 18% of the expected area for a pulse of maximum height.

The most likely case for the laser diode not reaching a sufficient power output is that the current through the diode is not reaching peak current corresponding to a maximum DAC value of 255 in 2.5 ns. This inefficiency is likely produced by a limitation of the maximum voltage slew rate of the single op-amp, which can't reach peak current in the time scale of 2.5 ns. One option for improving the peak current output would be a modification of the laser diode board with a second op-amp. This could increase the rise time of the pulse, but will improve the overall photon output.

Another solution to the light reduction issue is possibly using a longer pulse to allow for the laser diode to reach full power. Increasing the pulse width to 10 ns would allow for the idle DAC value to be left low or at 0 since there would be less need for a fast slew upwards to maximum. Simulations are currently being done on a 10 ns pulse width in SNO+ to determine the profile of light entering the PMTs (P. Rost). SNO+ has a <10 ns pulse after scattering and re-emission (by

the PPO wavelength shifter) in scintillator, thus pulse widths up to 10 ns may still be tolerable. PPO has a multi-component emission time, but ∼90% of the light is emitted with an exponential time constant of ∼2 ns.

6.4 Future Design Modifications

If the pulse cannot be extended to 10 ns, design modifications to the laser diode PCB will be required to improve the power output of the diode. As mentioned, a second op-amp will have to be installed on the PCB to improve the overall light output. This could lengthen the rise time of the pulse, however. Thus, the first priority must be to determine if the pulse time can be extended to 10 ns before making any changes to the hardware.

Additionally, further programming of the user interface would improve user-friendliness and make calibration event running more realistic to a supernova event. These improvements could include:

- pulse rate vs time live preview pop-up panels
- choice of distance of supernova (intensity inversely proportional)
- SN ASCII event file creation via RAT or other forms of MC simulation that feature model- and/or distance-dependent timing and energy arrays; timing and energy event files could be based on Poisson expected energy distribution functions
- Probability density and cumulative probability density histograms generation with plots being available to the user immediately following run
- possible integration into SNO+ current user system (ORCA) via Python language hand-holding

Appendix A

SNO+ Acrylic Vessel Cleanliness Studies

A.1 SNO+ Internal Background Measurements

The SNO+ experiment requires radioactive contamination control to obtain desired energy resolution and minimal background activity. The minimization of background events requires a high intrinsic purity of materials and the reduction of radioactivity on the surfaces of the detector components. Since the detector is located in an active mine where the rock and ore dust contains typically 60 mg/g Fe (approx. 1.1 g/g U and 6.4 g/g Th), while the inner components of the detector require at or below 10^{-12} g/g U and Th, dust levels have to be kept very low.

The acrylic vessel was extensively cleaned and rinsed with ultra-pure water to remove the build-up of mine dust and other deposits that accumulated on the surface during the running of SNO and the transition period between SNO and SNO+. The entire inner surface was cleaned to remove the materials that contain radioactive isotopes. To determine the level of contamination on the surface of the SNO+ acrylic vessel (AV), particularly from mine dust and its inherent radioactive elements, tapelifts were taken from the surface of the AV. X-Ray Fluorescence (XRF) is used to detect elements on the tapelifts.

Dust is removed from a surface by placing a section of thin adhesive tape (low in Fe) on the surface, pulling it off and placing it in an XRF spectrometer. X-ray fluorescence spectrometry

(XRF) was used for sensitive and precise measurements. In this method, one detects elements in the range of atomic number Z = 20 to 45 by the characteristic X-rays emitted following fluorescence of the sample with an x-ray tube. A spectrometer was built during SNO's lifetime for this purpose and located underground for convenient use. The XRF method involves elemental and chemical analysis of x-ray generated spectra of molecules present on samples lifted from the surface in question. It is described in detail in Section A.2 of this Appendix. The amount of mine dust deposited was inferred by measuring the amount of iron, which is present in the local mine dust at the level of 7%. When a single piece of tape is used to perform five lifts from adjacent areas on a surface, the sensitivity can be extended down to about 0.015 g/cm^2. This method was used to monitor the surface cleanliness of the acrylic vessel.

SNO+ cleanliness testing was modeled after SNO's [105], [106]. The contamination of the SNO+ experiment is defined by the target cleanliness levels achieved by the Borexino experiment [79],[107]. Target levels are measured with respect to mine dust concentration and the LAB (Linear Alkyl Benzene) mass. Radioactivity levels of isotopes of interest are estimated via these values. The internal backgrounds at the level of those measured in Borexino are assumed to be on the order of 10^{-17} g/g of ^{238}U and ^{232}Th [79]. The decay chains for these radioactive isotopes are seen in Figure A.1. Among the different daughters, ^{214}Bi, ^{210}Bi, ^{212}BiPo and ^{208}Tl are identified as the main backgrounds for the double beta and solar studies. In addition, Radon-222 is also a special concern due to the fact that it decays to Lead-210 ($T_{1/2}$=22.2 years), which decays to ^{210}Bi, similar in shape to the CNO neutrinos spectrum. Any additional source of ^{222}Rn (such as from external contamination, calibration sources, etc.), will increase the ^{210}Pb background and consequently the ^{210}Bi background.

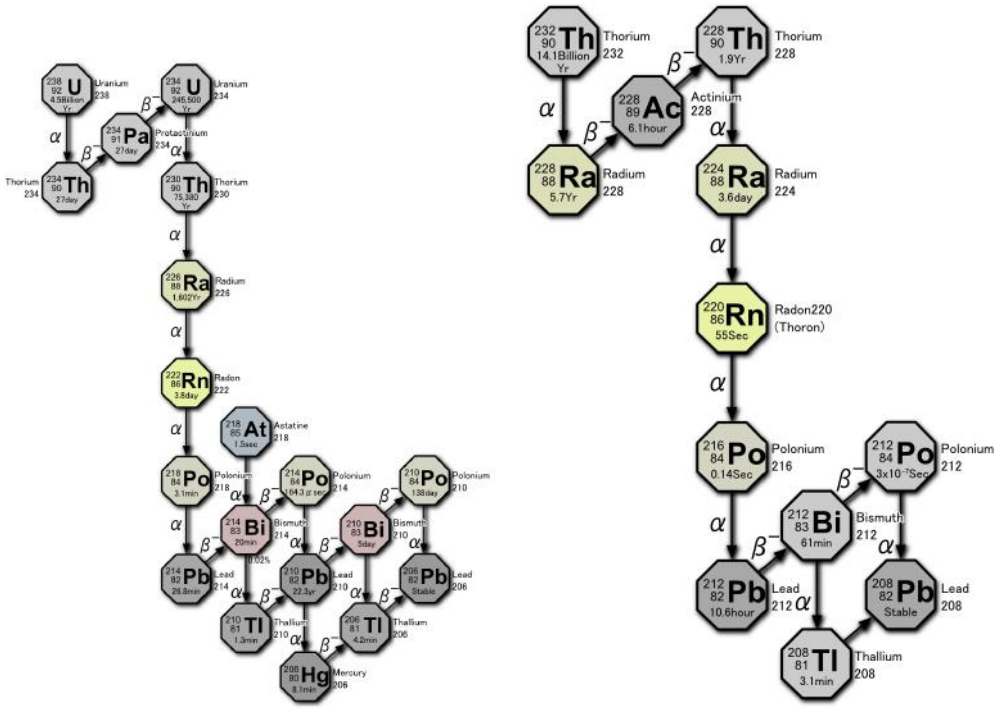

Figure A.1: *Left*: ^{238}U decay chain showing decay to ^{222}Rn gas. *Right*: ^{232}Th decay chain showing decay to ^{220}Rn gas.

To achieve the same background levels as the Borexino liquid scintillator, the target level of the mine dust concentration was set to be less than 2 ng dust/cm^2 [107]. Considering the inner surface area of the AV acrylic sphere (4.52 x 10^6 cm^2), there can be no more than ∼9 mg of dust within the detector volume. This contamination level is much higher than the standards of the original SNO experiment, thus SNO+ should achieve these cleanliness standards.

The results from the cleaning of the inner AV surface (neck, upper and lower hemispheres) are presented in this document in terms of mine dust concentrations and isotope activity levels of interest.

A.2 XRF Data Acquisition

The XRF system resides at the SNOLAB underground Ladder Lab C. It uses a molybdenum anode x-ray generator and an Amptek Silicon Drift Detector which recently replaced a SiLi detector (details can be found at SNOLAB-STR-2012-001). The tapelift samples are inserted individually into the XRF system and exposed to x-rays at a constant geometry. The x-ray count is found within

an energy resolution of approximately 0-20 keV. The detector absorbs the x-rays scattered from the tapelift and passes the information to the spectrum analyzer in Amptek, which then translates the data by graphing the number of x-rays vs. energy channel.

The XRF tapelifts are hand-crafted by applying adhesive tape to an aluminum ring. The adhesive side of the tapelift is then applied at 5 locations on a test surface, constituting one tapelift (TL) sample. An iron standard containing 6300 ng $^2Fe/cm^2$ calibrates the system and a blank tapelift is created for every tapelift batch (labeled "TL-xxx") to ensure iron and other backgrounds are low and to quantify the effect of the background in the regions of interest. The iron standard tape is measured for a live time of 600 s (10 minutes), whereas the blank and samples are measured for 3600 s (1 hour) to increase the sensitivity of the measurement. The blank for a tapelift sample is usually another piece of tape from the same roll prepared during the same time as the other samples. On rare occasions a tape from one batch is used in place of an existent or non-existent blank for another batch. To obtain the most reliable measurements, it is best to make a tapelift, measure it as the blank before taking the sample, and measure it after taking a lift. This is usually impractical due to time constraints, but should be attempted for small batches. It is reasonable to assume that the background from tape rings prepared in a batch will be the same provided the same tape is used for each, so it is sufficient to use one blank tapelift for a number of samples prepared on the same day. There is some variation in the background per blank [108], however, thus blanks should normally be used with the batch they are created with.

A.3 Analysis Techniques

Several known K_α peaks of several elements are analyzed within the spectra: Argon, Potassium, Calcium, Chromium, Iron, Nickel, Copper, Zinc, and Molybdenum. The centre energies of these regions of interest are seen in Table A.1 [107].

Element	Ar	K	Ca	Cr	Fe_α	Ni	Cu	Zn	Mo
Central Energy (keV)	2.96	3.31	3.69	5.41	6.40	7.48	7.77	8.26	17.45

Table A.1: Spectral peak central energies of several regions of interest. The ROI extends $\pm$ 3σ.

A.3.1 Region of Interest Counting

Region of interest counting (ROI) was the analysis method used to identify the iron concentration on the tape lift samples from the K_α peak in this study. The ROI technique is based on the known peaks of the elements listed in Table A.1. The peaks in the regions of interest are integrated in a given energy window in the sample spectra to obtain the net iron counts in the sample, N_{Sample}, and in the blank spectra to obtain N_{Blank}. The net x-ray iron count is the difference between N_{Sample} and N_{Blank}. The iron standard concentration (6300 ng ^{2}Fe/cm^2), the known mine dust mass per unit area (MPA) measured through the percentage of mine dust that is iron (7%), the number of times the tapelift is lifted off of a surface (5), and the counts from the iron standard (N_{FeStd}) in the same region are used in Equation A.1 to find the mine dust concentration, (ρ), in ng/cm^2. The corresponding error for this calculation is seen in Equation A.2 [108].

$$\rho = \frac{6300(N_{Sample} - N_{Blank})}{(5)(0.07)(N_{FeStd})} \Big[\frac{ng}{cm^2}\Big] \tag{A.1}$$

$$\delta\rho = \Big(\frac{6300}{(5)(0.07)(N_{FeStd})}\Big)\sqrt{\delta N^2_{Sample} + \delta N^2_{Blank} + \delta N^2_{FeStd}\Big(N_{Sample} - N_{Blank}\Big)} \tag{A.2}$$

A.3.2 Peak-Wing Fitting

A second method of analysis, peak-wing fitting, is presented for reference to the analysis techniques available, but was not used for the purposes of this study. The technique uses two Gaussians to fit the K_α and K_β peaks of the iron spectra at centre energies 6.40 and 7.06 keV, respectively. The wing regions around each peak were selected on the left and right sides to determine background. These regions were chosen for generally stable background on the left and right sides of the peaks: [6.05, 6.20] and [6.70, 6.85] keV. To determine the net counts ($N_{NetPeak}$) under the peak, it uses a local background estimation subtraction from the wings of the Gaussians. The integrated counts on the left and right (N_{Left}),(N_{Right}) are taken from the left and right wing regions of the Gaussian fit and divided by the number of channels (δx) in each region. From this, the area of the peak is determined in both the blank and sample tapes using:

$$N_{NetPeak} = N_{GrossPeak} - \left[\frac{N_{Left} \cdot \delta x_{Peak}}{2 \cdot \delta x_{Left}}\right] - \left[\frac{N_{Right} \cdot \delta x_{Peak}}{2 \cdot \delta x_{Right}}\right] \tag{A.3}$$

The error formula for this method is based on a binomial with a very low probability, as most x-rays pass through the tape without interacting, scatter, or fluoresce in directions not entering the spectrometer. Due to this, the variance of the counts in any region is equal to the number of counts, and the statistical error of the net counts is then:

$$\delta N_{NetPeak} = \sqrt{N_{GrossPeak} - N_{Left}\left[\frac{\delta x_{Peak}}{2 \cdot \delta x_{Left}}\right]^2 + N_{Right}\left[\frac{\delta x_{Peak}}{2 \cdot \delta x_{Right}}\right]^2} \tag{A.4}$$

The method is essentially taking an average of the left and right backgrounds around the peaks and subtracting this from the gross estimate of counts under the peak. From the net peak counts, Equation A.1 can then be used to determine the iron concentration, but substituting the blank subtraction from the sample with $N_{NetPeak}$.

The difference between ROI and peak-wing is the derivation of the net counts: ROI uses the region of the Ka iron peak alone, whereas peak-wing uses both the Ka and Kβ.

The peak-wing method, though finding greater area under two iron peaks, is often not accurate when subtracting unusually high backgrounds from the wing regions when the sample and blank are on the same order of dust concentration. It is also inefficient at estimating background when several other high peaks surround the iron K_α and K_β peaks in a sample, thus, it was not utilized in this study. Only the region of interest raw iron counts were used to calculate the mine dust concentration on the sample using Equation A.1.

The fits from the peak-wing method are outlined in Figure A.2 in the typical iron standard ^{2}Fe spectra (red). The fits work well when the concentration of iron is significantly higher than background, but poorly when dealing with small concentrations of dust near the sensitivity limits of the XRF system. The regions of interest fits are also visible in blue on this plot for the elements mentioned in Table A.1. Note that the region of interest fit (blue) also applies to the K_α and K_β peaks.

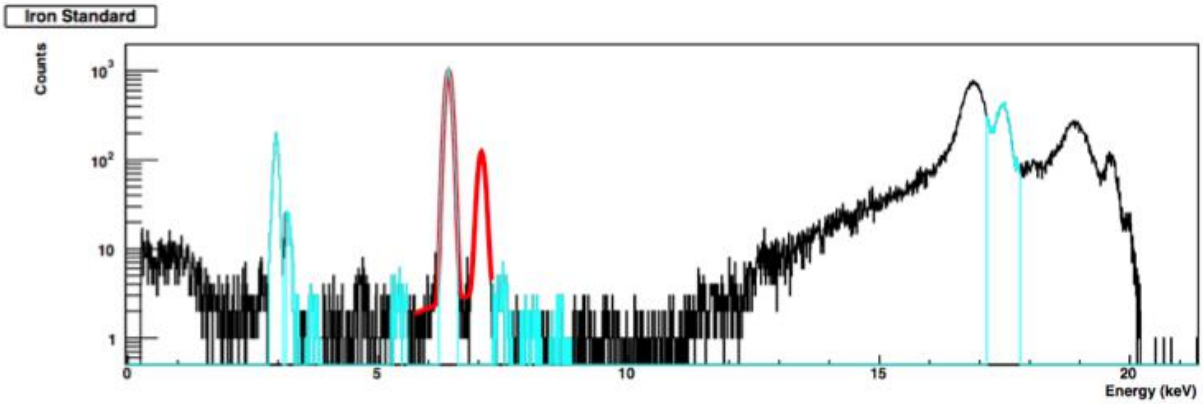

Figure A.2: Typical iron standard ^{2}Fe calibration spectra showing ROI (blue) and double Gaussian (red) peak fits for the two methods of analysis. The Fe peaks are prominent at just above 5.5 keV, with K_α on the left and K_β on the right. The Ar peaks are visible above 3 keV and the Mo peaks are clearly visible between 16-20 keV.

A.4 Results

A.4.1 Iron Concentration of AV Samples

The mine dust concentrations (ρ) in ng/cm^2 obtained for the inner surface of the AV upper and lower hemispheres were determined from the iron peaks of each tapelift. These were calculated from tapelifts lifted on the surface before cleaning (baseline) and after cleaning. Several blank tapes were also analyzed to assess the consistency of the blank subtraction method and the stability of the concentrations of iron inherent in the tape (See Figures A.3 and A.4).

Iron concentration is defined as:

$$\overline{\rho} = \frac{6300 \cdot N_{peak}}{N_{FeStd}}. \tag{A.5}$$

The distribution of the blank samples is relatively consistent with the mean, yet 6 outliers exist. The cause of these outliers is unknown, although it can be attributed to possible contamination by user handling or misplacement in the x-ray beamline. When these values are considered in the mean, the iron concentration is 29.25 ng/cm^2. By removing the outliers, the remaining values correspond with a previous study completed by C. Bruulsema [108] (Figure A.4). A more accurate mean is calculated using both sets of values to be 25.15 ng/cm^2. The distribution of the AV samples is plotted among the blanks in Figure A.5. The AV iron concentrations are values from each tapelift

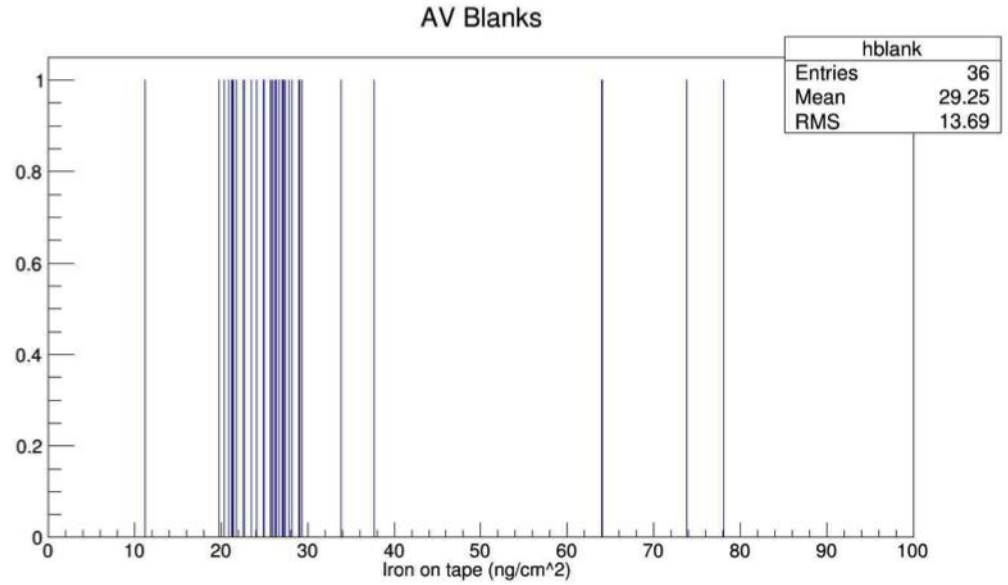

Figure A.3: Distribution of iron concentrations of the blank samples which were used against the AV sample tapelifts. Consistency is seen around the mean of 29.25 ng/cm^2.

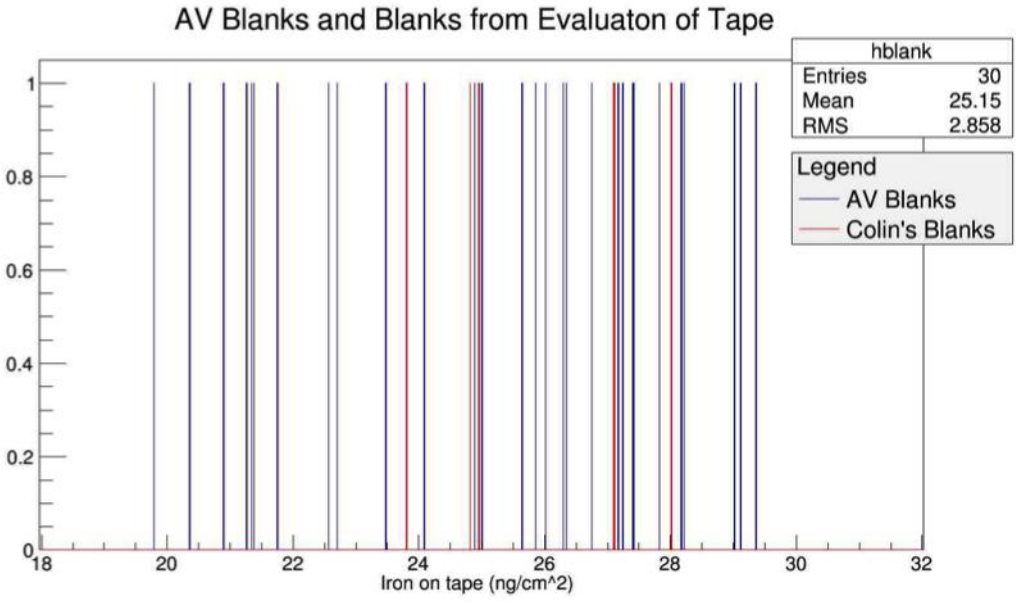

Figure A.4: Distribution of all blank samples used in the tapelift analysis overlaid with a previous blanks test [108]. AV blanks show consistency with the concentrations of iron found on the previous blanks. The mean of all these samples is 25.15 ng/cm^2.

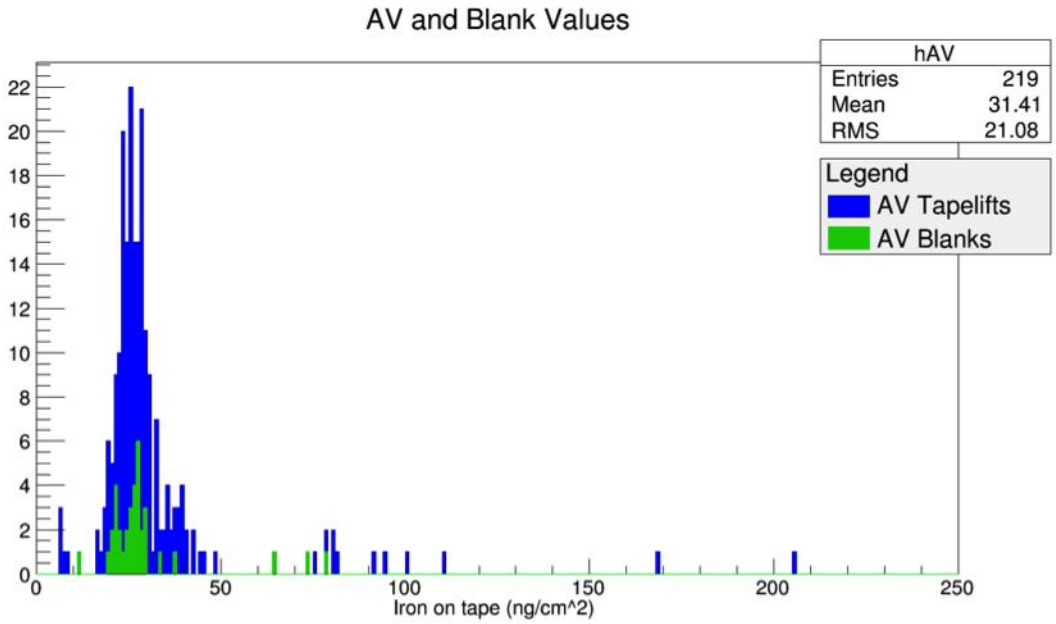

Figure A.5: Plot displays both the distribution of all the blank samples (excluding C. Bruulsema ("Colin's") previous blanks) and the distribution of all the AV tapelift samples. As can be seen, some outliers exist; however, most values fall around the blanks mean. This indicates that the AV values have very low concentrations of iron that are consistent with blank levels. The mean of the tapelift samples (including the outliers over 150 ng/cm^2) is 31.41 ng/cm^2.

sample taken after cleaning the inner surface area of the acrylic vessel as seen in Figure A.5. Most values fall amongst the mean of the blanks. Two outliers can be seen above 100 ng/cm^2. These are possibly attributed to user contamination. Including these values in the mean of the AV samples taken after cleaning allows for a larger average of 31.41 ng/cm^2. This is used to overestimate the iron concentration when subtracting the blank mean of 25.15 ng/cm^2.

Staring from the Iron on tape (ρ) Equation A.6 is used to calculate the mean mine dust concentration ($\bar{\kappa}_{Dust}$) on the inner AV surface. The value was found to be approximately 17.89 ng/cm^2.

$$\bar{\kappa}_{Dust} = \frac{(\bar{\rho}_{Sample} - \bar{\rho}_{Blank})}{(5)(0.07)} \left[\frac{ng}{cm^2}\right] \tag{A.6}$$

A.4.2 Effective Radioactivity of Inner AV Surface

The mean of the mine dust concentration $\bar{\kappa}_{Dust} = 17.89$ ng/cm^2 was converted to activity (decays per year) for each isotope of interest (Table A.3). Calculations were based on the conversion factors in Table A.2 determined by previous studies [109] along with several known constants. Calculations

considered 778 tonnes (x 10^6 g) of the solvent linear alkyl benzene (LAB) directly in contact with the inner surface of the AV which has an area of 4.52 x 10^6 cm^2 given the AV radius of roughly 6m. The total mass of mine dust on the inner AV surface is then 0.0809 g.

Parent Isotope	Specific Activity (mBq/g dirt)	Average Rock Concentration (ppm = μg element/g dirt)
^{238}U	13.58 ± 1.59	1.11 ± 0.13 [75]
^{232}Th	22.76 ± 2.13	5.56 ± 0.52 [75]
^{40}K	310 ± 40	10000 ± 1300*

Table A.2: Conversion factors used in conversion of iron concentration to radioactivity. Values are considered "worst case scenario" estimates based on gamma-ray emission detection of rock samples in Creighton Mine. *^{40}K value based on the concentration of natK [109].

Parent Isotope	Total Isotope on AV (ng element)	Concentration in LAB (g element/g LAB)
^{238}U	89.76	1.14
^{232}Th	449.60	5.73
^{40}K	808628	10301

Table A.3: Concentration of isotopes in approximately 800t of LAB.

Table A.4 displays the activity values leading to the estimated amount of Radon atoms present per day due to the external dust on the inner AV surface. The expected Rn contribution from the ^{238}U chain is 95 atoms/day. The cover gas target level is <600 Rn atoms/day which is after considering a 50x factor reduction in Rn atoms through the neck [107]. Considering the background levels of the acrylic volume (M=30t) wherein ^{214}Bi contributes ∼1.18 × 10^7 events/year (32,329 Rn atoms/day), the estimated daily Rn atom amount from the external AV dust is relatively insignificant. These results imply that the SNO+ AV is clean by the standards described in the Section A.1 and has tolerable levels of mine dust for its physics searches.

Parent Isotope	Total Activity on AV (mBq)	Annual Activity (decays/year)	Radon atoms/day	Isotope (decays/year)
^{238}U	1.1	34653	95	34653 (^{214}Bi)
^{232}Th	1.8	58078	159	20908 (0.36 ^{208}Tl)
^{40}K	25	791052	N/A	N/A

Table A.4: Activity values of each isotope considering inner surface area of AV. Radon contributions only applicable to branching of ^{238}U and ^{223}Th chains. Isotope activity is obtained using the branching values shown in brackets

Appendix B

SNC+ PMT Testing: Extended Data

B.1 NDF Attenuation Offset Fitting

In addition to the attenuation correction in Chapter 5, a chi-square minimization test with 2 degrees of freedom was performed on the idle DAC sweep data to determine the offsets when correcting for NDF attenuation. The idle DAC areas in a period of 500 ns were scaled with 2 parameters allowed to adjust: the area offset between curves and the optical density factor of the NDF used, and the following equation was used:

$$A_{scaled} = (A - A_{offset})10^{OD} \tag{B.1}$$

where A is the original area data, A_{offset} is the adjustable area offset parameter, OD is the adjustable optical density parameter and A_{scaled} is the resulting area value. The χ^2 was minimized using:

$$\chi^2 = \Sigma\frac{(A_{scaled} - A)^2}{A} \tag{B.2}$$

Results of the fit are listed in Table B.1 and compared to nominal and spectrophotometry values.

OD_{Nom}	OD_{Spec}	A_{Offset}
1.0	1.0673	5e-9
1.5	1.6203	3.7e-9
2.0	2.4976	3.25e-9
2.5	3.0509	3.22e-9
3.0	3.5649	3.25e-9

Table B.1: Results of fitting the idle DAC level areas to the measured optical density values measured with a spectrometer (OD_{Spec}); the averages are taken for 405-406 nm. OD_{Nom} are the nominal optical densities of the filters and A_{Offset} are the offsets encountered in the area when the curves are corrected for attenuation through the NDFs.

The fitted OD values from the chi-square minimization are shown in Figure B.1 as a function of the nominal NDF values and shows tolerable offset.

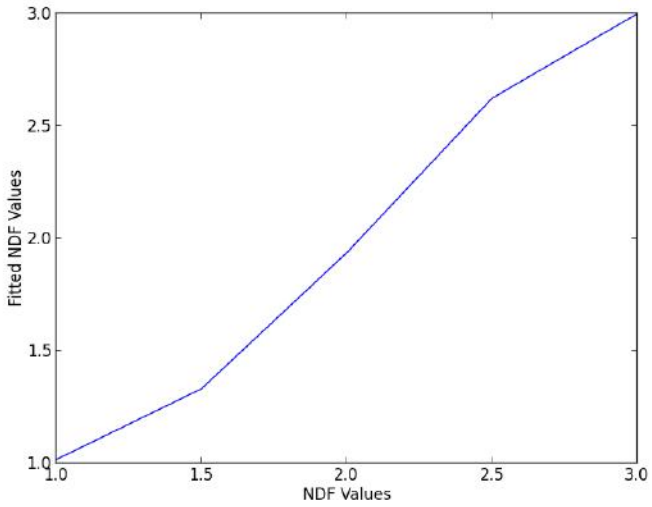

Figure B.1: The fitted NDF/OD values from the chi-square minimization were plotted against the theoretical OD values listed in the specifications. Offsets are tolerable.

B.2 Pulses at Idle DAC Level of 17500

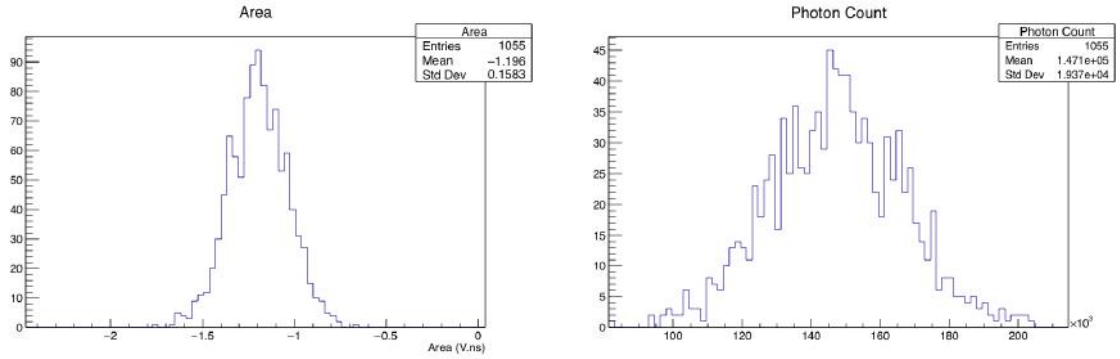

Figure B.2: Histograms for a pulse DAC value of 255 at an idle DAC of 17,500.

B.3 Pulses at Idle DAC Level of 20000

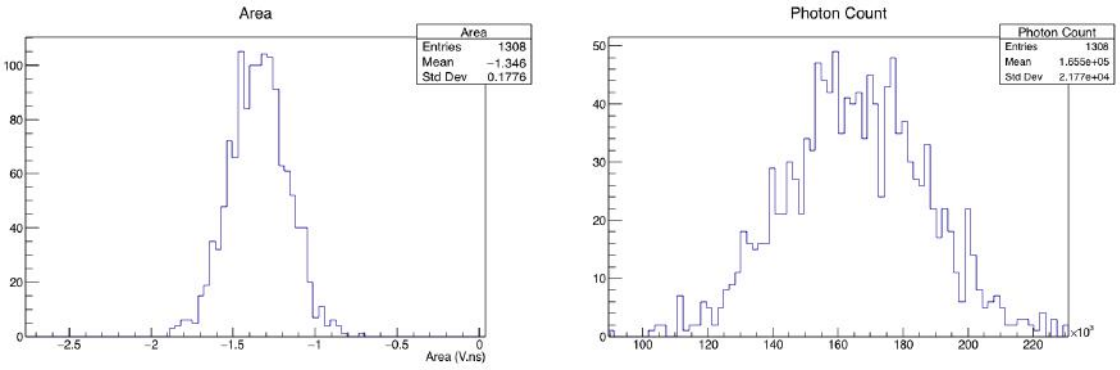

Figure B.3: Histograms for a pulse DAC value of 255 at an idle DAC of 20,000.

B.4 Frequency Dependence Test

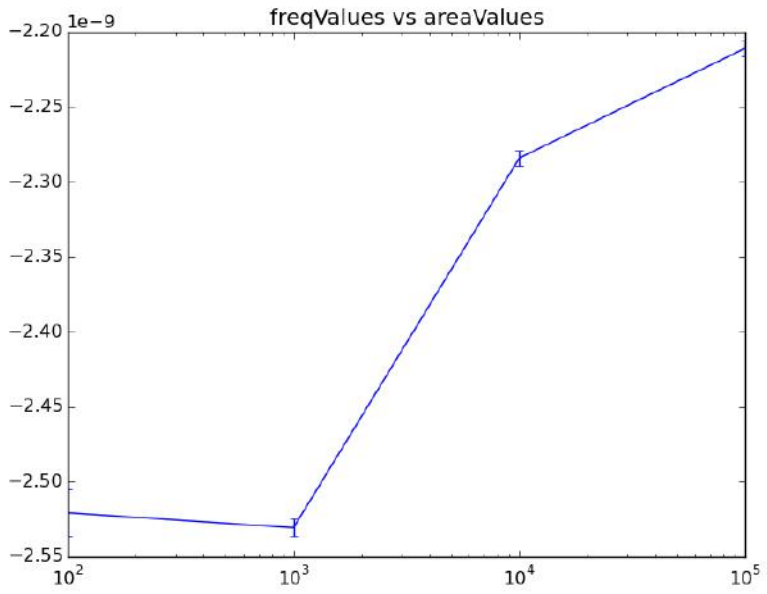

Figure B.4: Preliminary frequency-dependence tests performed prior to taking commissioning data. Oscilloscope data was taken with maximum pulse DAC amplitude of 255 at an idle DAC level of 12,500 with the NDF2 filter in place, with pulse frequencies of 100, 1000, 10,000, and 100,000 Hz. The scope began to fail after 10,000 Hz. The figure shows the area values (in Vs) as a function of frequency (Hz). The pulse area values (taken in a 15 ns period with idle DAC level subtraction) negligibly increase with higher frequencies ($\sim$13% tolerance). The results of this test suggested that all scope commissioning data be taken at 1000 Hz to ensure no data loss.

B.5 Spontaneous Emission Trace Voltage

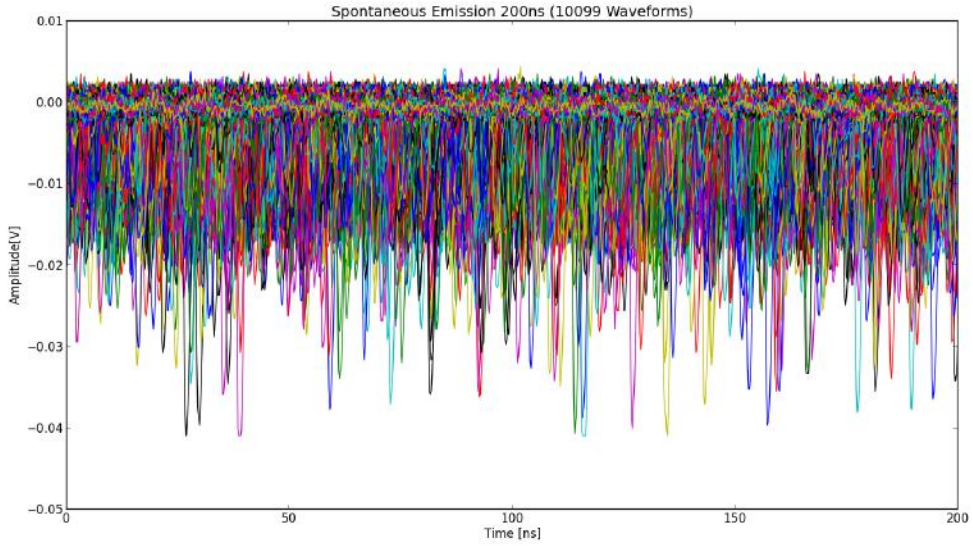

Figure B.5: The overlaid plot of over 10,000 scope traces taken for an idle DAC value of 0 and a pulse DAC value of 0. The amplitude or voltage levels of the light produced by the laser diode's spontaneous emission are shown within a period of 200 ns. Data was taken with the PMT used in commissioning and the NDF2 filter. Peak maxima do not exceed -0.042V.

Appendix C

SNC+ Technical Documentation

C.1 Front Panel PCB 10-Pin Header Functionality

J1 Pin	J1 Sig	J2 Pin	Function
17	P0.0	9	Shutter *Enabled* (TTL level from FP PCB)
19	P0.1	8	Shutter *Interlock OK* (TTL level from FP PCB)
21	P0.2	7	Shutter *Closed* (TTL level from FP PCB)
23	P0.3	6	Shutter *Open* (TTL level from FP PCB)
25	P0.4	5	LED3 (*Initialized*) (TTL level from USB-8451)
27	P0.5	4	LED4 (*Loading*) (TTL level from USB-8451)
29	P0.6	3	LED5 (*Ready*) (TTL level from USB-8451)
30	GND	1, 10	+12V GND
31	P0.7	2	LED6 (*Running*) (TTL level from USB-8451)

Table C.1: Connection mapping between J1 and J2 of the DAC daughterboard. Refer to NI USB-8451 User Manual.

C.2 NI USB-8451 Board Pinout

Signal	Pin	Connector	Pin	Signal
NC	1		2	GND
NC	3		4	SCLK
SDA	5		6	GND
SCL	7	Pin 1 Pin 2	8	MISO
NC	9		10	GND
CS5	11		12	MOSI
CS6	13		14	GND
CS7	15		16	CS0
P0.0	17		18	GND
P0.1	19		20	CS1
P0.2	21		22	GND
P0.3	23	Pin 33 Pin 34	24	CS2
P0.4	25		26	GND
P0.5	27		28	CS3
P0.6	29		30	GND
P0.7	31		32	CS4
+5V	33		34	+5V

Signal Name	Direction	Description
SPI CS <0..7>	Output	**Chip Select Signals**—Outputs used to select the desired SPI peripheral device.
SPI MOSI (SDO)	Output	**Master Output Slave Input**—SPI communication signal to slave device.
SPI MISO (SDI)	Input	**Master Input Slave Output**—SPI communication signal from slave device.
SPI CLK (SCLK)	Output	**SPI Clock**—SPI output clock signal to slave devices capable of clock rates up to 12 MHz.
I^2C SDA	Input or Output	**I^2C Serial Data**—Data signal for I^2C communication.
I^2C SCL	Output	**I^2C Clock**—I^2C clock signal to slave devices capable of clock rates up to 250 kHz.
P0.<0..7>	Input or Output	**Digital I/O Signals**—You can individually configure each signal as an input or output. You can configure the port for open-drain or push-pull output.*
+5 V	Output	**+5 V**—The voltage source provided by the USB host. The voltage is nominally 5 V, but varies from system to system.
GND	—	**Ground**—The reference for the digital signals and the +5 VDC supply.
NC	—	**No Connect**—Do not connect any signals to this terminal.

* If you configure the DIO port for open-drain output, you must supply pull-up resistors to V_{cc} (3.3 or 5 V). The resistor value must not be lower than 1 kΩ.

Figure C.1: The USB-8451 IDC connector (J1) pin assignments and their signal descriptions derived from the NI USB-8451 user manual. Any 34-pin female IDC (ribbon) cable can be used to connect to the IDC connector.

C.3 Laser Diode PCB Circuit Schematic

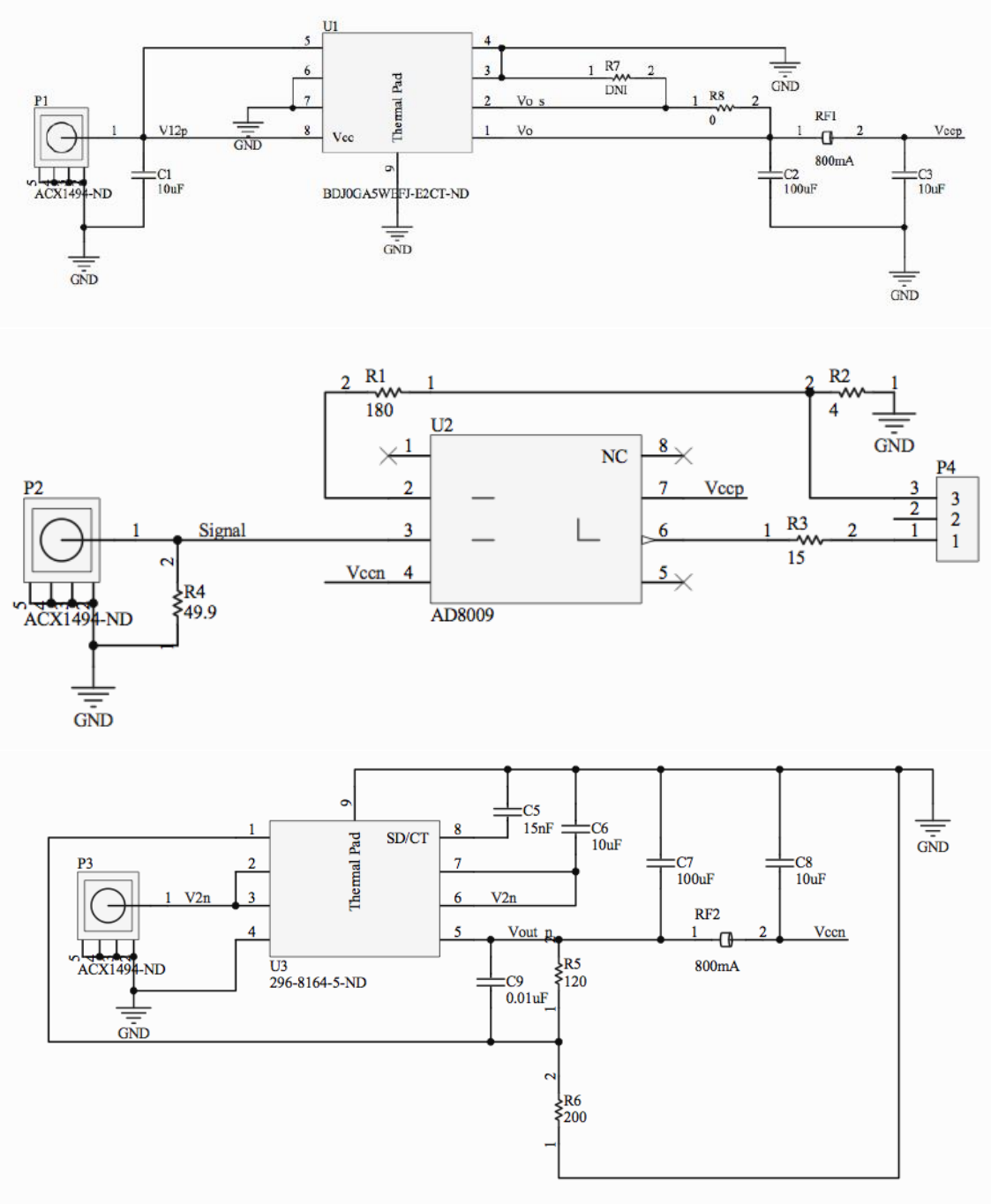

Figure C.2: Laser diode driving PCB schematic developed by J.P. Martin.

C.4 Potentiometer Box and Circuit

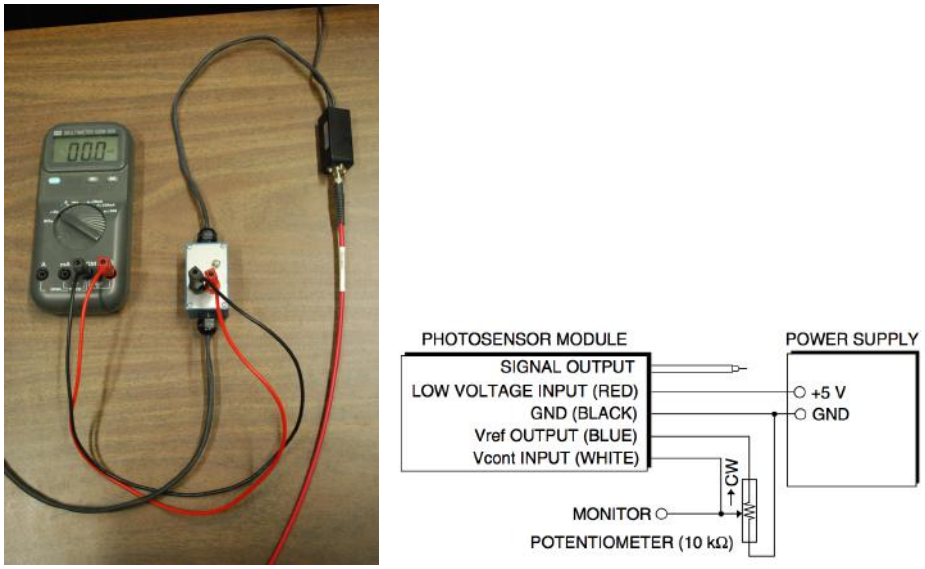

Figure C.3: In the left figure, the PMT (right) is powered by a +5V input voltage from an external power supply. A potentiometer trimmer pot box (center) was developed based on the circuit shown (right image) and adjusts the PMT sensitivity between +0.5-1.1 V, in essence controlling the gain of the PMT. This control voltage is then monitored by an external voltmeter (left).

C.5 DAC Daughterboard Block Diagram

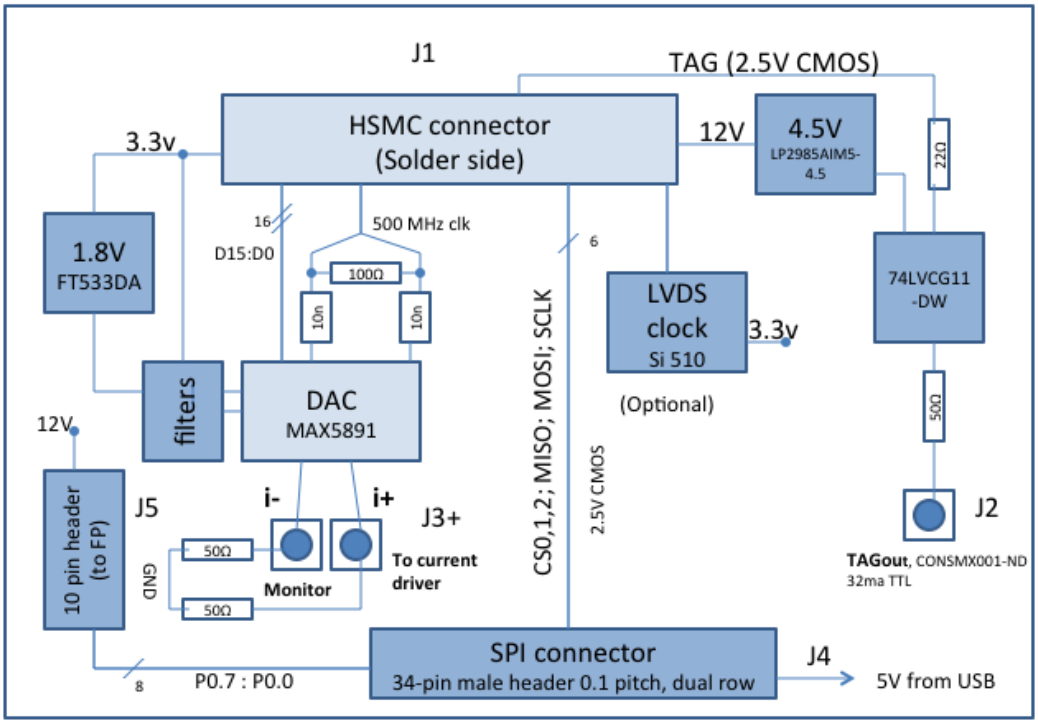

Figure C.4: DAC daughterboard block diagram. **J1**: Samtec ASP-122952-01 HSMC Connection to Altera Board (placed on underside); **J2**: BNC jack for tagged bit; **J3**: MCX connectors for "P2" laser diode signal; **J4**: 34-pin USB-8451 connection (IDC, male, 0.1" pitch); **J5**: 10-pin header to front panel PCB. The Current DAC daughterboard PCB schematic is on the next page. Design by J.P. Martin at the University of Montreal.

C.6 Front Panel Interlock and Indication PCB Circuit Schematic

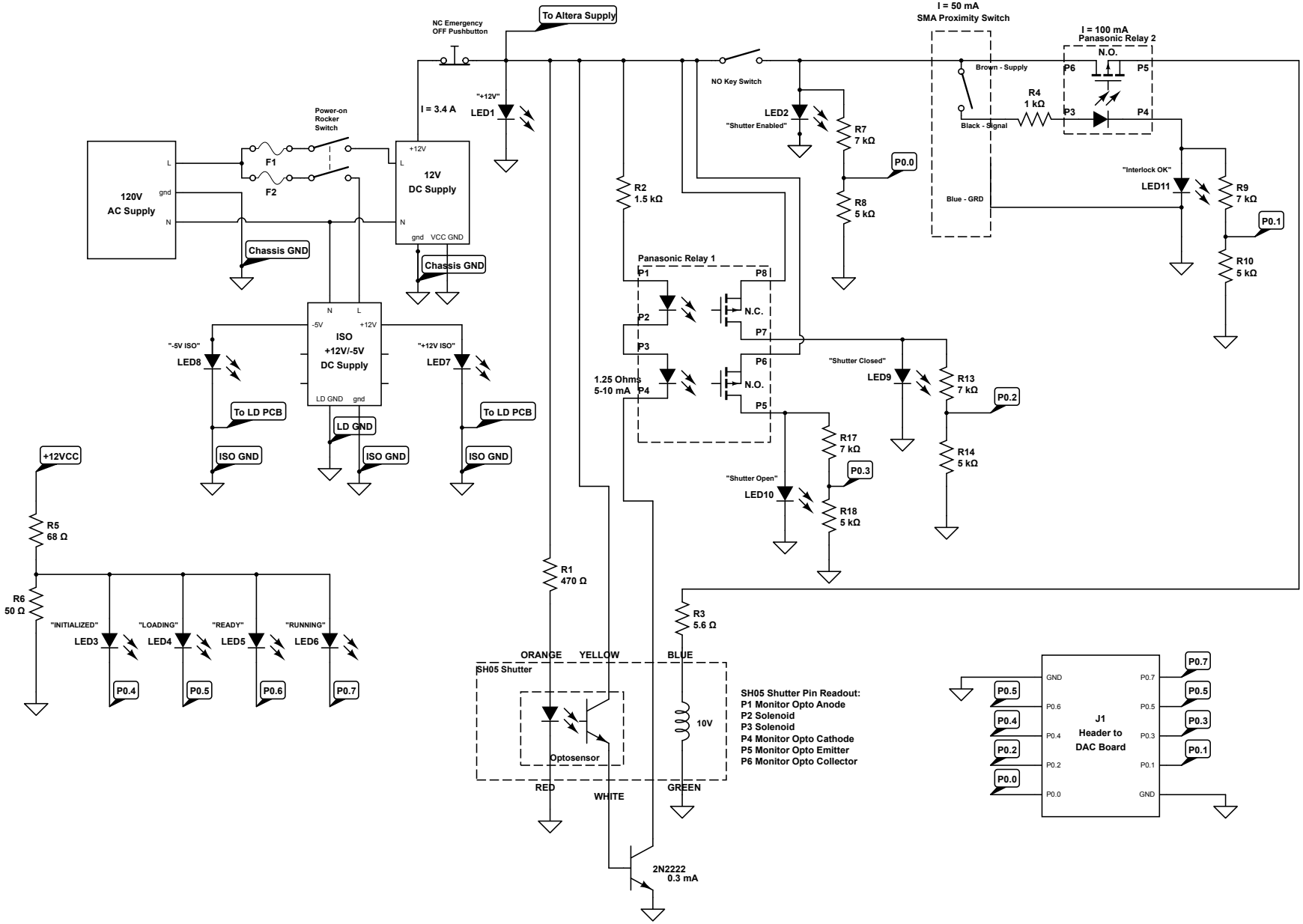
To Altera Supply
NC Emergency OFF Pushbutton
I = 50 mA
SMA Proximity Switch
I = 100 mA
Panasonic Relay 2
N.O.
P6
P5
P3
P4
Brown - Supply
Black - Signal
Blue - GRD
NO Key Switch
I = 3.4 A
"+12V"
LED1
LED2
"Shutter Enabled"
R4
1 kΩ
R7
7 kΩ
P0.0
R8
5 kΩ
R2
1.5 kΩ
Power-on Rocker Switch
F1
F2
120V
AC Supply
L
gnd
N
12V
DC Supply
+12V
gnd
VCC GND
Chassis GND
Chassis GND
"Interlock OK"
LED11
R9
7 kΩ
P0.1
R10
5 kΩ
Panasonic Relay 1
P1
P2
P3
P4
P8
P7
P6
P5
N.C.
N.O.
1.25 Ohms
5-10 mA
N
L
-5V
+12V
ISO
+12V/-5V
DC Supply
LD GND
gnd
"-5V ISO"
LED8
"+12V ISO"
LED7
To LD PCB
To LD PCB
LD GND
ISO GND
ISO GND
ISO GND
"Shutter Closed"
LED9
R13
7 kΩ
P0.2
R14
5 kΩ
R17
7 kΩ
P0.3
"Shutter Open"
LED10
R18
5 kΩ
+12VCC
R5
68 Ω
R6
50 Ω
"INITIALIZED"
LED3
"LOADING"
LED4
"READY"
LED5
"RUNNING"
LED6
P0.4
P0.5
P0.6
P0.7
R1
470 Ω
R3
5.6 Ω
ORANGE
YELLOW
BLUE
SH05 Shutter
Optosensor
10V
RED
WHITE
GREEN
2N2222
0.3 mA
SH05 Shutter Pin Readout:
P1 Monitor Opto Anode
P2 Solenoid
P3 Solenoid
P4 Monitor Opto Cathode
P5 Monitor Opto Emitter
P6 Monitor Opto Collector
J1
Header to
DAC Board
GND
P0.6
P0.4
P0.2
P0.0
P0.7
P0.5
P0.3
P0.1
GND

Bibliography

[1] O. Hahn and O. von Baeyer. *Phys. Z.*, 11(448), 1910.

[2] C. D. Ellis and W. A. Wooster. *Proc. R. Soc. London.*, Ser. A 117(109), 1927.

[3] W. Pauli. Offener Brief an die Gruppe der Radioaktiven bei der Gauvereine Tagung zu Tüb. 1930.

[4] C. L. Cowan Jr., F. Reines, F. B. Harrison, H. W. Kruse, and A. D. McGuire. Detection of the free neutrino: A confirmation. *Science*, 124(3212):103–104, July 1956.

[5] G. Danby, J-M. Gaillard, K. Goulianos, L. M. Lederman, N. Mistry, M. Schwartz, and J. Steinberger. Observation of high-energy neutrino reactions and the existence of two kinds of neutrinos. *Phys. Rev. Lett.*, 9:36–44, June 1962.

[6] M. N. Z. Maki, M. Nakagawa, and S. Sakata. Remarks on the unified model of elementary particles. *Prog. Theo. Physics*, 28(5):870–880, 1962.

[7] M. Goldhaber, L. Grodzins, and A. W. Sunyar. Helicity of neutrinos. *Phys. Rev.*, 109(3):1015–1017, 1958.

[8] B. Pontecorvo. Neutrino experiments and the question of leptonic-charge conservation. *Sov. Phys. JETP*, 26:984–988, 1968.

[9] R. Davis, D. S. Harmer, and K. C. Hoffman. Search for neutrinos from the sun. *Phys. Rev. Lett.*, 20:1205–1209, 1968.

[10] M. L. Perl, G. S. Abrams, and A. M. Boyarski *et al.* Evidence for anomalous lepton production in e^+ - e^- annihilation. *Phys. Rev. Lett.*, 35(22):1489–1492, 1975.

[11] DONUT Collaboration (K. Kodama *et al.*). Observation of tau neutrino interactions. *Phys. Lett.*, B504:218–224, 2001.

[12] LEP Collaboration. Precision electroweak measurements on the z resonance. *Physics Reports*, 427(5-6):257–454, 2006.

[13] R. Kotthaus and Johann H. Kuhn, editors. *Proceedings of the 24th International Conference on High-Energy Physics*, August 1988.

[14] Kamiokande-II Collaboration (K. S. Hirata *et al.*). Experimental study of the atmospheric neutrino flux. *Physics Letters*, B205(416), 1988.

[15] Super-Kamiokande Collaboration (Y. Fukuda *et al.*). Measurement of a small atmospheric ν_μ/ν_e ratio. *Physics Letters*, B433, 1998.

[16] Super-Kamiokande Collaboration (Y. Fukuda *et al.*). Study of the atmospheric neutrino flux in the multi-gev energy range. *Physics Letters*, B436:33–41, 1998.

[17] The SNO Collaboration (Q. R. Ahmad *et al.*). Measurement of the rate of $\nu_e + \mathrm{d} \rightarrow \mathrm{p} + \mathrm{p} + \mathrm{e}^-$ interactions produced by $^8\mathrm{B}$ solar neutrinos at the Sudbury Neutrino Observatory. *Phys. Rev. Lett.*, 87, 2001.

[18] Nobelprize.org (Nobel Media AB 2014). The Nobel Prize in Physics 2015. `http://www.nobelprize.org/nobel_prizes/physics/laureates/2015/`. Accessed: 2015-02-09.

[19] ATLAS Collaboration. Observation of a new particle in the search for the standard model higgs boson with the ATLAS detector at the LHC. *Physics Letters B*, 716(1), 2012.

[20] M. Turatto. Classification of Supernovae. *ArXiv Eprints*, (arXiv:astro-ph/0301107), 2003.

[21] Borexino Collaboration (G. Bellini *et al.*). Neutrinos from the primary proton-proton fusion process in the Sun. *Nature*, 512(7515), 2014.

[22] Borexino Collaboration (G. Bellini *et al.*). Measurement of geo-neutrinos from 1353 days of Borexino. *Phys. Lett. B*, 722(295), 2013.

[23] F. Vissani and G. Pagliaroli. The diffuse supernova neutrino background: Expectations and uncertainties derived from SN1987A. *Astronomy and Astrophysics*, 528(L1), 2011.

[24] F. Vissani. Comparative analysis of SN1987A antineutrino fluence. *J. Phys. G: Nucl. Part. Phys.*, 42(013001), 2015.

[25] OPERA Collaboration. Discovery of tau neutrino appearance in the CNGS neutrino beam with the OPERA experiment. *Phys. Rev. Lett.*, 115(121802), 2015.

[26] IceCube Collaboration (M. G. Aartsen *et al.*). Observation of high-energy astrophysical neutrinos in three years of IceCube data. *JPhys. Rev. Lett.*, 113(101101), 2014.

[27] F. Vissani. Neutrino Sources and Properties. *ArXiv Eprints*, (arXiv:1412.8386v2), 2015.

[28] Determining the oscillation parameters by solar neutrinos and kamLAND. *Physics Letters B*, 562(1–2):28 – 35, 2003.

[29] G.A. Tammann, W. Löffler, and A. Schröder. The galactic supernova rate. *Astrophysical Journal Supplement Series*, 92:487–493, 1994.

[30] T. Kajita. Atmospheric neutrino results from Super-Kamiokande and Kamiokande - Evidence for ν_μ oscillations. *Nucl. Phys. Proc. Suppl.*, 77(123-132), 1999.

[31] IceCube Collaboration (M. G. Aartsen *et al.*). First observation of PeV-energy neutrinos with IceCube. *Phys. Rev. Lett.*, 111(021103), 2013.

[32] N. Jelley, A. B. McDonald, and R. G. H. Robertson. The Sudbury Neutrino Observatory. *Annu. Rev. Nucl. Part. Sci.*, 59(431-65), 2009.

[33] S. M. Bilenky, J. Hosek, and S. T. Petcov. On oscillations of neutrinos with Dirac and Majorana masses. *Phys. Lett.*, B94:495, 1980.

[34] A. Yu. Smirnov. The MSW Effect and Solar Neutrinos. *Phys. Scripta*, T121:57–64, 2005.

[35] Mainz Collaboration (Ch. Weinheimer *et al.*). Improved limit on the electron-antineutrino rest mass from tritium β-decay. *Physics Letters*, B300(210), 1993.

[36] K. Nakamura and P. D. Group. Review of Particle Physics. *Journal of Physics G: Nuclear and Particle Physics*, 37(7A):075021, 2010.

[37] KATRIN Collaboration (J. Wolf *et al.*). The KATRIN Neutrino Mass Experiment. *Nucl. Instrum. Meth.*, A623:442–444, 2010.

[38] L. Bodine, D. S. Parno, and R. Robertson *et al.* Assessment of molecular effects on neutrino mass measurements from tritium beta decay. *ArXiv Eprints*, (arXiv:1502.03497), 2015.

[39] K.A. Olive *et al.* (Particle Data Group). *Chin. Phys.*, C38(090001), 2014.

[40] E. Majorana. Symmetrical Theory of Electrons and Positrons. *Nuovo Cim.*, 14:171, 1937.

[41] R. Saakyan. Two-neutrino double-beta decay. *Annu. Rev. Nucl. Part. Sci.*, 63(503-529), 2013.

[42] EXO Collaboration. Observation of two-neutrino double-beta decay in ^{136}xe with the EXO-200 detector. *Phys. Rev. Lett.*, 107:212501, 2011.

[43] Planck Collaboration. Planck 2013 results. I. Overview of products and scientific results. *Astronomy & Astrophysics*, 2014.

[44] M. Redshaw *et al.* Masses of ^{130}Te and ^{130}Xe and Double-β-Decay Q-value of ^{130}Te. *Physical Review Letters*, 102(21), 2009.

[45] F. T. Avignone III, S. R. Elliott, and J. Engel. Double beta decay, Majorana neutrinos, and neutrino mass. *Review of Modern Physics*, 80(481-516), 2008.

[46] K. Scholberg. Supernova neutrino detection. *Annu. Rev. Nucl. Part. Sci.*, arXiv:1205.6003, 2012.

[47] W. Baade and F. Zwicky. On super-novae. *PNAS*, 20(5):254–259, 1934.

[48] H.A. Bethe. Supernova mechanisms. *Rev. Mod. Phys.*, 62(801), 1990.

[49] K. Hirata et al. Observation of a neutrino burst from the supernova SN1987A. *Phys. Rev. Lett.*, 58(1490), 1987.

[50] R.M. Bionta *et al.* Observation of a neutrino burst in coincidence with supernova 1987A in the Large Magellanic Cloud. *Phys. Rev. Lett.*, 58(1494), 1987.

[51] H.-Th. Janka *et al.* Theory of core-collapse supernovae. *Physics Reports*, 442:38–74, 2007.

[52] J. N. Bahcall and S. L. Glashow. Upper limit on the mass of the electron neutrino. *Nature*, 326(6112), 1987.

[53] R. Minkowski. Spectra of Supernovae. *Publications of the Astronomical Society of the Pacific*, 53(314):224, 1941.

[54] A. Maury *et al.* Supernova 2000er in Pgc 9132. *IAU Circ.*, 7528(2), 2000.

[55] A. Heger, C.L. Fryer, S.E. Woosley, N. Langer, and D.H. Hartmann. How massive single stars end their life. *The Astrophysical Journal*, 591:288–300, 2003.

[56] G.E. Brown and H.A. Bethe. The equation of state of dense matter: supernovae, neutron stars and black holes. *Nucl. Phys. A*, 574:217–230, 1994.

[57] F. Calura and F. Matteucci. Cosmic supernova rates and the Hubble Sequence. *The Astrophysical Journal*, 652:889–901, 2006.

[58] S.D. Van Dyk. Association of supernovae with recent star formation regions in late type galaxies. *The Astronomical Journal*, 103(6), 1992.

[59] S. M. Adams, C. S. Kochanek, and J. F. Beacom *et al.* Observing the next galactic supernova. *Astrophys. J.*, 778:164, 2013.

[60] A. Burrows. Supernova explosions in the universe. *Nature*, 403:727–733, 2000.

[61] S.E. Woosley and T. Janka. The physics of core-collapse supernovae. *Nature Physics*, 1(147), 2005.

[62] R. Buras, M. Rampp, H.-Th. Janka, and K. Kifonidis. Two-dimensional hydrodynamic core-collapse supernova simulations with spectral neutrino transport. *Astron. Astrophysics*, 447(1049-1092), 2006.

[63] H.-Th. Janka. Explosion mechanisms of core-collapse supernovae. *Ann. Rev. Nucl. Part. Sci.*, 62:407–451, 2012.

[64] A. Mezzacappa, S.W. Bruenn, and E.J. Lentz *et al.* Recent progress on ascertaining the core collapse supernova explosion mechanism. *ArXiv E-prints*, (1501.01688), 2015.

[65] K. M. Lee (Astronomy Education at the University of Nebraska-Lincoln Web Site). Hertzsprung-Russel simulation. `http://astro.unl.edu`. Accessed: 2015-08-04.

[66] S. Chandrasekhar. On stars, their evolution and their stability. Technical report, University of Chicago, Chicago, Illinois USA, 1983. Nobel Prize Lecture.

[67] A. Burrows, J. Hayes, and B.A. Fryxell. On the nature of core-collapse supernova explosions. *Astrophysical Journal*, 450:830, 1995.

[68] J. R. Wilson. Supernovae and post-collapse behavior. *Numerical Astrophysics*, page 422, 1985.

[69] H. A. Bethe and J. R. Wilson. Revival of a stalled supernova shock by neutrino heating. *The Astrophysical Journal*, 295:14–23, 1985.

[70] A. Burrows, E. Livne, L. Dessart, C.D. Ott, and J. Murphy. Features of the acoustic mechanism of core-collapse supernova explosions. *Astrophysical Journal*, 655:416–433, 2006.

[71] A. Burrows, L. Dessart, E. Livne, C.D. Ott, and J. Murphy. Simulations of magnetically-driven supernova and hypernova explosions in the context of rapid rotation. *The Astrophysical Journal*, 664(416):434, 2007.

[72] E. M. Burbidge, G. R. Burbidge, W. A. Fowler, and F. Hoyle. Synthesis of the elements in stars. *Rev. Mod. Phys.*, 29(4):547–650, 1957.

[73] SNO Collaboration (J. Boger *et al.*). The Sudbury Neutrino Observatory. *Nuclear Instrumentation and Methods in Physics Research*, A449:172–207, 2000.

[74] Depth of major underground laboratories. `http://www.deepscience.org/contents/underground_universe.shtml`. Accessed: 2015-07-08.

[75] S. Andringa, E. Arushanova, and S. Asahi *et al.* Current status and future prospects of the SNO+ experiment. *Advances in High Energy Physics*, 2016:6194250, 2015.

[76] L. Segui. Background reduction in the SNO+ experiment. *AIP Conference Proceedings*, 1672, 2015.

[77] R. Ford for the SNO+ Collaboration. A scintillator purification plant and fluid handling system for SNO+. *ArXiV E-prints*, (arXiv:1506.08746), 2015.

[78] J. Klein for the SNO+ Collaboration. The SNO+ Experiment. `http://fsnutown.phy.ornl.gov/fsnufiles/positionpapers/snoplus_position_post.pdf`. Accessed 2015-06-23.

[79] C. Arpesella *et al.* Direct measurement of the ^{7}Be solar neutrino flux with 192 days of Borexino data. *Physical Review Letters*, 101:091302, 2008.

[80] Borexino Collaboration (G. Alimonti *et al.*). The liquid handling systems for the Borexino solar neutrino detector. *Nuclear Instruments and Methods in Physics Research*, A609(1):58–78, 2009.

[81] E. Arushanova. *Pileup background rejection in SNO+ Experiment*, IoP Meeting 2015 - Manchester. April 2015.

[82] E. Arushanova and A. R. Back. Probing neutrinoless double beta decay with SNO+. *ArXiv E-prints*, (arXiv:1505.00247 [physics.ins-det]), 2015.

[83] V. Lozza for the SNO+ Collaboration. Neutrinoless double beta decay search with SNO+. *EPJ Web of Conferences*, 65(01003), 2014.

[84] J. Kotila and F. Iachello. Phase-space factors for double-β decay. *Phys. Rev. C*, 45:034316, 2012.

[85] J. Barea, J. Kotila, and F. Iachello. Nuclear matrix elements for double-beta decay. *Phys. Rev. C*, 87(014315), 2013.

[86] A. Burrows *et al.* The future of supernova neutrino detection. *Phys. Rev. D*, 45:10, 1992.

[87] G. Pagliaroli, F. Vissani, M.L. Costantini, and A. Ianni. Improved analysis of SN1987A antineutrino events. *Astroparticle Physics*, 31(3):163–176, 2009.

[88] M. T. Keil, G. G. Raffelt, and H.-T. Janka. Monte carlo study of supernova neutrino spectra formation. *The Astrophysics Journal*, 590(2):971–991, 2003.

[89] J. F. Beacom, W. M. Farr, and P. Vogel. Detection of supernova neutrinos by neutrino-proton elastic scattering. *Phys. Rev.*, D66(033001), 2002.

[90] B. von Krosigk, M. Chen, and S. Hans *et al.* Measurement of α-particle quenching in LAB based scintillator in independent small-scale experiments. *ArXiv E-prints*, (arXiv:1510.00458 [physics.ins-det]), 2015.

[91] T. Lund and J. P. Kneller. Combining collective, MSW, and turbulence effects in supernova neutrino flavor evolution. *Phys. Rev. D*, 88(2):023008, 2013.

[92] B. von Krosigk, L. Neumann, R. Nolte, S. Röttger, and K. Zuber. Measurement of the proton light response of various LAB based scintillators and its implication for supernova neutrino detection via neutrino-proton scattering. *The European Physical Journal C*, 73(2390), 2013.

[93] B. von Krosigk. *Measurement of proton and α–particle quenching in LAB based scintillators and determination of spectral sensitivities to supernova neutrinos in the SNO+ detector*. PhD thesis, Technical University Dresden, 2015.

[94] R. Ford. *Calibration of SNO for the Detection of ^8B Neutrinos*. PhD thesis, Queen's University, 1998.

[95] B.A. Moffat, R.J. Ford, F.A. Duncan, K. Graham, A.L. Hallin, C.A.W. Hearns, J. Maneira, and P. Skensved. Optical calibration hardware for the sudbury neutrino observatory. *Nucl. Instrum. Meth.*, (A554):255–265, 2005.

[96] J. R. Sinclair. Laserball hardware status. *SNO+ Internal Document*, docDB:1748v2, March 2013.

[97] M. Stringer. MC simulation of the effect of the new laserball neck on the PMT angular response. *Internal SNO+ document*, (docDB:2889-v4), 2015.

[98] K. Vynck. *A Supernovae Calibration Source for the Sudbury Neutrino Observatory*, B.Sc. thesis, Laurentian University, 2004.

[99] M. Yen. SNO+ 0.3%-te doped scintillator. *SNO+ Internal Document*, docDB:2079v1, August 2013.

[100] M. Chen. LAB Scintillator. *SNO+ Internal Document*, docDB:11v1, May 2007.

[101] SHARP. Sharp GH04P21A2GE high-power, blue violet laser diode. *ET*, 070803, July 2007.

[102] M. Yen. SNO+ Te-LS development. *SNO+ Internal Document*, docDB:3053v1, March 2015.

[103] J. Maneira, M. Mottram, S. Peeters, J. Sinclair, and J. Waterfield. Characterisation procedure for TELLIE LED drivers. *SNO+ Internal Document*, docDB:3841v1, Nov 27, 2013.

[104] P. Rost. Neutral density filter measurements. *Correspondence Document*, 2015-12-30.

[105] E.D. Hallman and R.G. Stokstad. Establishing a cleanliness program and specifications for the sudbury neutrino observatory. *SNO Internal Report*, SNO-STR-91-009(Accessed at ¡http://www.sno.phy.queensu.ca/sno/str/SNO-STR-91-009.pdf¿), September, 1991.

[106] E. Kong. Contamination control study on mine dust. *SNO Internal Report*, SNO-STR-92-49(Accessed at ¡http://www.sno.phy.queensu.ca/sno/str/SNO-STR-92-049.pdf¿), June, 1992.

[107] D. Chauhan, O. Chkvorets, and C. Jillings *et al.* Cleanliness monitoring using XRF technique and interpretation of tape lift numbers to radioactivity levels for the SNO+ Experiment. *SNO+ Internal Document*, (docDB:1529-v10), 2012.

[108] C. Bruulsema. XRF Accuracy Analysis. *SNO+ Internal Document*, (docDB:x), 2012.

[109] I. Lawson. Analysis of rock samples from the new laboratory. *SNO+ Internal Document*, (docDB:x), 2005.